



저작자표시-비영리-변경금지 2.0 대한민국

이용자는 아래의 조건을 따르는 경우에 한하여 자유롭게

- 이 저작물을 복제, 배포, 전송, 전시, 공연 및 방송할 수 있습니다.

다음과 같은 조건을 따라야 합니다:



저작자표시. 귀하는 원저작자를 표시하여야 합니다.



비영리. 귀하는 이 저작물을 영리 목적으로 이용할 수 없습니다.



변경금지. 귀하는 이 저작물을 개작, 변형 또는 가공할 수 없습니다.

- 귀하는, 이 저작물의 재이용이나 배포의 경우, 이 저작물에 적용된 이용허락조건을 명확하게 나타내어야 합니다.
- 저작권자로부터 별도의 허가를 받으면 이러한 조건들은 적용되지 않습니다.

저작권법에 따른 이용자의 권리는 위의 내용에 의하여 영향을 받지 않습니다.

이것은 [이용허락규약\(Legal Code\)](#)을 이해하기 쉽게 요약한 것입니다.

[Disclaimer](#)

Doctor of Philosophy

**New Phase Boundary Originating from
Coexistence of Ferroelectrics and Relaxor in
Lead-free Piezoelectric KNN-based Composites**

**The Graduate School
of the University of Ulsan
Department of Materials Science
and Engineering
TRANG AN DUONG**

**New Phase Boundary Originating from
Coexistence of Ferroelectrics and Relaxor in
Lead-free Piezoelectric KNN-based Composites**

Supervisor: Prof. JAE-SHIN LEE


**A Dissertation Submitted to
the Graduate School of the University of Ulsan
In Partial Satisfaction of the Requirements
for the Degree of
Doctor of Philosophy
by
TRANG AN DUONG**

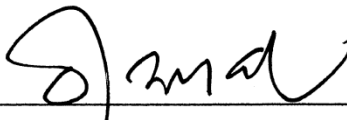
**Department of Materials Science and Engineering
University of Ulsan, Korea**

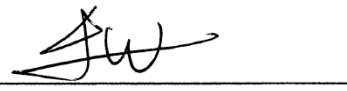
May 2021

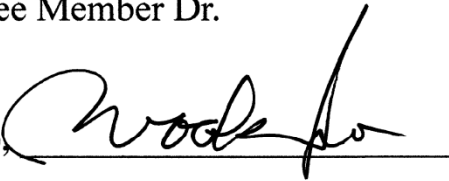
New Phase Boundary Originating from
Coexistence of Ferroelectrics and Relaxor in
Lead-free Piezoelectric KNN-based Composites

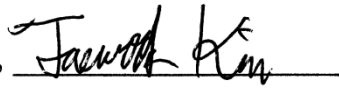
This certifies that the dissertation
of Trang An Duong is approved.

Dae-il Kim, 
Committee Chair Dr.

Jae-Shin Lee, 
Committee Member Dr.

Ji-won Jung, 
Committee Member Dr.

Wook Jo, 
Committee Member Dr.

Tae-wook Kim, 
Committee Member Dr.

School of Materials Science and Engineering
University of Ulsan
Korea, May 2021

Acknowledgements

I have received many helps and supports from a lot of people during my graduate study. First and foremost, I express my special gratefulness to my supervisor, Prof. Jae-Shin Lee, for his full support, affectionate guidance, patience and efficient supervision during the past six years. I am thankful to committee members Prof. Tae-il Kim, Prof. Ji-won Jung, Prof. Wook Jo and Dr. Tae-wook Kim for their time and valuable suggestions, which helped in improving the quality of present work.

I would like to extremely thank to my advisor, Dr. Hyoung-Su Han, for his speedy advices and affectionate discussions. His instructions about writing papers and doing experiments brought a great help to me in this research work. I highly appreciate and thank to all the members in the Smart Materials Lab (SM Lab) for their friendliness, devotedly helps and collaborations during my stay.

There are some other people from other laboratories, who provided me the constant help, good company and sharing laboratory equipments. I would like to give a special thanks to Prof. Ill-Won Kim and his group (UOU, Korea) for their training and technical supports, especially, Dr. Chang-Won Ahn for his collaboration in writing papers and discussions of any aspect of $S(E)$, $P(E)$, and $D(T)$ characterization. I would also like to express my gratitude to Prof. Wook Jo and his group (UNIST, Korea), especially, Mr. Woo-Seok Kang for his valuation, collaboration, and technical supports in $S(E)$, $P(E)$, temperature-dependent permittivity analyses. I would like to thank to Dr. Hyun-Young Lee for her help in PFM analyses.

Finally, I am very grateful for the big love and encouragement from my whole family and friends during my PhD period.

Abstract

Lead-based piezoelectric materials have been used in various commercial high-tech applications such as sensors, actuators and ultrasonic transducers. According to European environmental legislation, lead with high toxicity brings harmful effects on the environment and human. Recently, in order to replace lead-based piezoelectric materials, lead-free ones were strongly developed. Several kinds of lead-free piezoceramics have been extensively investigated, such as BaTiO₃-based, (Bi_{1/2}Na_{1/2})TiO₃-based and (K_{0.5}Na_{0.5})NbO₃-based (KNN) materials. Among them, KNN and its compounds have been considered as one of promising candidates because of their excellent dielectric and piezoelectric properties. The unique advantages of KNN ceramics such as a high Curie temperature ($T_C \approx 420^\circ\text{C}$) and a high piezoelectricity, represents a promising candidate for replacement of lead-based materials. From that, many studies focused on addition, substitution, modification chemical elements to improve the properties for KNN-based materials defined the concept of polymorphic phase transition (PPT) at room temperature, and morphotropic phase boundary (MPB). The PPT compositions in KNN-based materials have improved the piezoelectric properties; however, remain the temperature sensitive problem since the phase boundary corresponding to R-O or O-T possesses the PPT characteristic depending on not only the compositions but also the temperatures. To prevent this problem, many studies paid their attentions on MPB. The MPB is the nearly vertical phase boundary separating rhombohedral (R), tetragonal (T), and/or monoclinic (M) ferroelectric phases and nearly temperature independent. There are many studies for MPB, mentioned about the improvement in piezoelectric properties and the temperature stability of d_{33} . However, the explanation for these behaviors still remains a challenge. Recently, some studies suggested ferroelectric-relaxor phase boundary with the crystal structure transit from non cubic phase (orthorhombic or tetragonal) to pseudocubic (PC) phase. Though the enhancement of piezoelectric constant and/or electromechanical strain

can be observed, the temperature stability of piezoelectric properties was not considered.

In order to separate and maintain the phase in materials, the composite method was mentioned in this work, by mixing the calcined powders of two phase components. For tetragonal phase stabilization, SrTiO₃ is a promising candidate which can improve not only the sinterability but also piezoelectric properties of KNN ceramics. Tetragonal phase was stabilized and maintained good properties for the modification content of 0.06 mol. Such high amount of SrTiO₃ causes the higher sintering temperature and significantly reduces T_C . Then Li⁺ was doped into KNN-4ST to solve problems. On the other hand, we found the stabilized PC phase with relaxor features in BaZrO₃-modified KNN ceramics.

Finally, the ferroelectric/relaxor piezocomposites were compounded by T-phase KNN-4ST-4Li and PC-phase KNN-8BZ in different T-phase fraction f . The phase boundary was found at the composites of 70 mol% of T phase and 30 mol% of PC phase with the enhanced piezoelectric constant d_{33} and coupling factor k_p values of 210 pC/N and 34%, respectively. Besides, the enhanced strain properties at $f = 0.7$ composites are related with the coexistence of ferroelectric domain, tetragonal micro domains and polar nanoregions, which originates from the relatively contribution of the ferroelectric and relaxor components in composites. Moreover, the low variation ($\leq 10\%$) of d_{33} in the temperature range of 25°C –225°C performs good temperature stability of the piezoelectric constant, corresponding with phase transition in temperature dependent XRD patterns.

Table of contents

Acknowledgements	ii
Abstract	iii
Table of contents	v
List of Figures	viii
List of Tables	xiii
Chapter 1: Introduction	1
1.1. Back ground	1
1.2. Aim and scope of research	2
1.3. Outline of the thesis	3
Chapter 2: Theory and literature review	5
2.1. Basics of ferroelectrics	5
2.1.1. Crystal symmetry	5
2.1.2. Dielectrics.....	6
2.1.3. Piezoelectrics.....	7
2.1.4. Ferroelectrics	9
2.1.5. Perovskite structure	12
2.2. Status of piezoelectric materials	13
2.2.1. Lead-based piezoelectric materials.....	13
2.2.2. Lead-free piezoelectric materials.....	19
2.2.3. Phase boundaries in KNN-based materials	26
2.2.4. Relaxor ferroelectricity in KNN-based materials.....	28
Chapter 3: Experimental procedure and characterization	31
3.1. Materials synthesis	31
3.1.1. Powders processing.....	31
3.1.2. Ceramics processing.....	33

3.1.3. Composites processing	34
3.2. Characterization	34
3.2.1. Density measurement	34
3.2.2. X-ray diffraction analysis	35
3.2.3. Surface morphology and microstructure analysis	37
3.2.4. Piezoresponse force microscopy analysis, PFM	37
3.2.5. Dielectric and piezoelectric properties analysis	38
Chapter 4: New phase boundary in lead-free piezoelectric KNN-based composites originating from coexistence of ferroelectrics and relaxor	41
4.1. Investigation of high temperature phase transition behaviors and piezoelectric properties for BaZrO₃-modified lead-free KNN-BLT ceramics	41
4.1.1. Motivation and scope	41
4.1.2. Results and discussions	44
4.1.3. Conclusion.....	53
4.2. Effects of SrTiO₃ modification on piezoelectric and strain properties of lead-free K_{0.5}Na_{0.5}NbO₃-based ceramics	54
4.2.1. Motivation and scope	54
4.2.2. Results and discussions	56
4.2.3. Conclusion.....	63
4.3. Li⁺-doping effects on tetragonal phase stabilization of lead-free KNN-ST piezoceramics	65
4.3.1. Motivation and scope	65
4.3.2. Results and discussions	67
4.3.3. Conclusion.....	71
4.4. Ferroelectric-to-relaxor crossover in KNN-based lead-free piezoceramics.....	72

4.4.1. Motivation and scope	72
4.4.2. Results and discussions	74
4.4.3. Conclusion.....	87
4.5. New phase boundary in lead-free piezoelectric KNN-based composites.....	88
4.5.1. Motivation and scope	88
4.5.2. Results and discussions	91
4.5.3. Conclusion.....	102
Chapter 5: Summary.....	104
References.....	107
Publications	116

List of Figures

Figure 2.1. Relationship between dielectrics, piezoelectrics, pyroelectrics and ferroelectrics.	6
Figure 2.2. Polarization of dielectrics by an applied electric field.	7
Figure 2.3. Sketch images for two piezoelectric effects [16].	8
Figure 2.4. Electric and elastic boundary conditions in ferroelectric materials [17].	10
Figure 2.5. Polarization and strain versus electric field loops of ferroelectric crystal [21].	11
Figure 2.6. (a) Perovskite structure of unit cell and (b) ferroelectric BaTiO ₃ [22].	12
Figure 2.7. Electromechanical properties of PbZrO–PbTiO solid-solution ceramics on composition.	14
Figure 2.8. Phase diagram of the PbZrO ₃ – PbTiO ₃ solid solution system. [24]	15
Figure 2.9. Temperature dependent dielectric constant and dissipation factor of PMN and PMN–10PT compositions. [30]	17
Figure 2.10. Basic setup for evaluating electrooptic shutter/modulator characteristics [31].	18
Figure 2.11. Temperature dependent dielectric constant and phase diagram of PLZT [32].	19
Figure 2.12. Polymorphic phase transitions in barium titanate single crystals [33].	21
Figure 2.13. Possible crystal models of BNT [36].	23
Figure 2.14. Electric field–induced unipolar strain curves for BNST ceramics [7].	24
Figure 2.15. Phase diagram of the KNN solid solution [39].	25
Figure 2.16. Intrinsic traits of (a) the polymorphic phase boundary and (b) the morphotropic phase boundary [63].	28
Figure 2.17. Characteristics of relaxor ferroelectrics as compared to normal ferroelectrics [67]. .	29

Figure 3.1. The sketch of (a) calcination and (b) sintering process.....	33
Figure 3.2. (a) Multi Purpose X-Ray Diffractometer and (b) JEOL Field Emission Scanning Electron Microscope.	36
Figure 3.3. AixPES (aixACCT) setup for measuring P-E and S-E hysteresis loop.....	39
Figure 4.1. Polished and thermally etched surface images of KNN-BLT-100xBZ ceramics, (a) $x = 0.04$, (b) $x = 0.05$, (c) $x = 0.06$, (d) $x = 0.07$, and (e) $x = 0.08$	45
Figure 4.2. X-ray diffraction patterns of KNN-BLT-100xBZ ceramics in the 2θ ranges of (a) $20^\circ-70^\circ$, (b) $44.5^\circ-46.2^\circ$ and (c) deconvoluted peaks.....	46
Figure 4.3. Polarization (top) and bipolar strain curves (bottom) of KNN-BLT-100xBZ ceramics as a function of BZ content.	47
Figure 4.4. Changes of (a) P_{\max} , P_r , E_c values and (b) S_{\max} , S_{neg} values of KNN-BLT-100xBZ ceramics as a function of BZ content.	48
Figure 4.5. (a) Temperature-dependent dielectric constant and (b) dielectric loss of KNN-BLT-100xBZ ceramics, (c) temperature-dependent dielectric constant for KNN-BLT-6BZ ceramics at different frequencies, and (d) changes of phase transition temperatures as a function of BZ content.....	49
Figure 4.6. Changes of (a) d_{33} and k_p for KNN-BLT-100xBZ ceramics as a function of BZ content, temperature-dependent dielectric constant and d_{33} for (b) KNN-BLT-5BZ, (c) KNN-BLT-6BZ, and (d) KNN-BLT-8BZ ceramics.	50
Figure 4.7. Temperature-dependence of X-ray diffraction patterns in the 2θ ranges of $44.5^\circ-46.2^\circ$ for (a) KNN-BLT-5BZ, (b) KNN-BLT-6BZ, and (c) KNN-BLT-8BZ ceramics as a function of temperature and the deconvoluted results for (d) KNN-BLT-5BZ ceramics, (e) KNN-BLT-6BZ, and (f) KNN-BLT-8BZ ceramics at representative temperatures.	52
Figure 4.8. Polished and thermally etched surface images of lead-free KNN-100xST ceramics (a) $x = 0$, (b) $x = 0.01$, (c) $x = 0.03$, (d) $x = 0.04$, (e) $x = 0.10$. (f) Average grain size and relative density for KNN-100xST ceramics as a function of ST content.	57

Figure 4.9. X-ray diffraction patterns of KNN–100xST ceramics as a function of ST content in the 2θ ranges of (a) 20° – 70° and (b) 44.4° – 46.4° . (c) Lattice parameters and tetragonality.	58
Figure 4.10. Temperature–dependent dielectric properties of KNN–100xST ceramics, (a) temperature–dependent dielectric constant (ϵ_r), (b) dielectric loss of KNN–100xST ceramics, (c) ϵ_r for KNN–3ST ceramics at different frequencies, and (d) the extracted phase transition temperatures as a function of ST content.	59
Figure 4.11. (a) Bipolar strain and polarization curves, (b) S_{pol} , S_{rem} values, (c) P_{max} , P_r and E_c values of KNN–100xST ceramics.	61
Figure 4.12. The (a) unipolar strain curves (b) normalized strain d_{33}^* , difference $S_{pol} - S_{rem}$ and $P_m^2 - P_r^2$ of KNN–100xST ceramics.	62
Figure 4.13. Phase diagram of KNN–100xST ceramics.	63
Figure 4.14. Polished and thermally etched surface images of lead–free KNN–4ST–100yL ceramics (a) $y = 0$, (b) $y = 0.01$, (c) $y = 0.02$, (d) $y = 0.03$, (e) $y = 0.04$, and (f) $y = 0.06$	67
Figure 4.15. X-ray diffraction patterns of KNN–4ST–100yL ceramics as a function of Li content in the 2θ ranges of (a) 20° – 70° , (b) 44.4° – 46.4° , and (c) lattice parameter.	68
Figure 4.16. (a) Temperature–dependent dielectric dielectric constant ϵ_r of KNN–4ST–100yL ceramics, and (b) the extracted phase transition temperatures as a function of Li^+ content.	69
Figure 4.17. (a) Polarization and bipolar strain curves, (b), P_{max} , P_r , E_c values (c) S_{max} , S_{neg} values of KNN–4ST–100yL ceramics.	70
Figure 4.18. Piezoelectric constant d_{33} , electromechanical coupling factor $k_{p,r}$ and phase transition temperature of KNN–4ST–100yL ceramics.	71
Figure 4.19. The polished and thermally etched surface images of KNN–based ceramics, (a) pure KNN (b) KNN–1Z, (c) KNN–5Z, and KNN–100yBZ ceramics for (d) $y = 0.03$, (e) $y = 0.06$, (f) $y = 0.08$, (g) $y = 0.10$	75
Figure 4.20. X-ray diffraction patterns of (a) pure KNN, (b) KNN–100xZ, (c) KNN–100yBZ	

ceramics in the 2θ ranges of 20° – 70° , (d) 29.6° – 33.2° and (e) 43° – 46.6°	77
Figure 4.21. Temperature–dependent dielectric constant (ϵ_r) for (a) all compositions at 100 kHz and (b) pure KNN, (c) KNN–1Z, (d) KNN–6BZ, (e) KNN–8BZ, and (f) KNN–10BZ ceramics.	78
Figure 4.22. Electric–field–induced strain and polarization curves for (a) KNN, KNN–100xZ ceramics as red blocks, (b) $x = 0.01$, (c) $x = 0.05$, and KNN–100yBZ ceramics as blue blocks; similarly for (d) $y = 0.03$, (e) $y = 0.06$, (f) $y = 0.08$, (g) $y = 0.10$, (h) $y = 0.15$.	80
Figure 4.23. The (a) dielectric, ferroelectric, and (b) strain properties of KNN, (top) KNN–100xZ and (bottom) KNN–100yBZ ceramics.	81
Figure 4.24. Changes in the piezoelectric constant (d_{33}) and electromechanical coupling factor (k_p) for pure KNN, KNN–100xZ, and KNN–100yBZ ceramics.	82
Figure 4.25. Evaluation of diffused phase transition for KNN–100yBZ ceramics using (a) the reciprocal of the dielectric constant ($1/\epsilon'$) as a function of the temperature and (inset) T_{CW} ; (b) the $\log(1/\epsilon' - 1/\epsilon'_m)$ vs. $\log(T - T_m)$ plot at 1 kHz and (inset) the fitted γ values for KNN–100yBZ ceramics.	84
Figure 4.26. Schematic diagram for the three different states of (a) pure KNN, (b) KNN–8BZ, and (c) KNN–15BZ ceramics.	86
Figure 4.27. The polished and thermally etched surface images of KNN–based composites, with different T–phase fraction: (a) $f = 0$, (b) $f = 0.1$, (c) $f = 0.3$, (d) $f = 0.5$, (e) $f = 0.06$, (f) $f = 0.7$, (g) $f = 0.8$, (h) $f = 0.9$, and (i) $f = 1$.	92
Figure 4.28. X–ray diffraction patterns of KNN–based composites in the 2θ ranges of (a) 20° – 70° , (b) 44.5°	93
Figure 4.29. (a) Temperature–dependent dielectric constant (ϵ_r) for all KNN–based composites at 100 kHz. (b) Phase transition temperatures.....	94
Figure 4.30. (a) Electric–field–induced strain and polarization curves for KNN–based composites and (b, c) extracted values.....	95

Figure 4.31. Piezoelectric constant (d_{33}), mechanical quality factor (Q_m), and electromechanical coupling factor (k_p) for KNN-based composites.....	96
Figure 4.32. High temperature X-ray diffraction patterns of KNN-based composites in the 2 θ range of 44.4°–46.4°	98
Figure 4.33. Temperature-dependent dielectric constant and d_{33} behavior for KNN-based composites with different T-phase fraction: (a) $f=0$, (b) $f=0.3$, (c) $f=0.7$ and (d) $f=1$	99
Figure 4.34. PFM mappings of KNN-based composites on 2.0 $\mu\text{m} \times 3.0 \mu\text{m}$ area. (a1) and (a2) $f=0$, (b1) and (b2) $f=0.7$, (c1) and (c2) $f=1$ composites.	100
Figure 4.35. Schematic diagram for the three different states of (a) $f=0$, (b) $f=0.7$, and (c) $f=1$ composites.....	102

List of Tables

Table 1. 32 three-dimensional crystallographic point groups in crystals	6
Table 2. Polymorphic phase boundary in KNN-based materials.....	27
Table 3. Effect of 1 mol% additives on the phase transition temperatures of KNN ceramics	28
Table 4. Conditions for calcination and sintering.....	32
Table 5. Crystal structure and electrical properties of lead-free KNN-100xST ceramics	58

Chapter 1: Introduction

1.1. Back ground

Lead-based piezoelectric materials have been used in various applications for sensors and actuators, based on their mutual conversion between mechanical energy and electrical energy [1-3]. However, it seems that the high toxicity of lead (Pb) in wastes of those devices causes serious problems to environment and human body. Some laws and regulations were legislated to prohibit the use of lead, including European Union passed the Restriction of Hazardous Substances (RoHS) law in 2003, Household Electronic Products Recycling Law in Japan, and Electronic Information Product Pollution Control Management Regulation in China in 2006 [4]. Hence, lead-free materials have been intensively investigated to replace lead-based piezoelectric material. Several groups of lead-free piezoceramics have been extensively investigated, such as BaTiO_3 [5,6], $(\text{Bi}_{1/2}\text{Na}_{1/2})\text{TiO}_3$ [7,8], and $(\text{K}_{0.5}\text{Na}_{0.5})\text{NbO}_3$ (KNN) [9-11]. Among them, potassium sodium niobate $\text{K}_{0.5}\text{Na}_{0.5}\text{NbO}_3$ (KNN) has drawn much attention due to their relatively high Curie temperature, excellent dielectric and piezoelectric properties. Several promising achievements was recently reported in KNN-based ceramics with constructing new phase boundaries such as polymorphic phase transition (PPT) [12] and morphotropic phase boundary (MPB) [13]. While PPT leads to the temperature sensitive problem since the characteristic depends on both composition and temperature, the nearly vertical phase boundary MPB depending on temperature can solve that problem. Liu *et al.* (2018) introduced a way of forming MPB by shifting diffused phase transitions closer to create a partially overlapped phase transition over a broad temperature range [14]. In this work, we suggest another approximation to form an MPB by mixing two end members with different crystal symmetries at room temperature. In the formation of rhombohedral (R)-tetragonal (T) MPB, most of studies believed that the R phase in KNN ceramics can

be stabilized by $AZrO_3$ ($A = Ba, Ca, Sr \dots$) modification. However, some studies recently suggested the stabilization of relaxor based on the orthorhombic (O)–pseudocubic (PC) phase transition in $AZrO_3$ –modified KNN. Therefore, there are still arguments on the definition of the stabilized phase in KNN ceramics by modifying Zr–based compounds. In this thesis, the stabilized phase in $BaZrO_3$ –modified KNN is defined as PC phase relating with the ferroelectric–to–relaxor transition. By using a T phase and a PC phase components to produce the composites, we obtain the new T–PC phase boundary with the enhanced piezoelectric properties and temperature stability in KNN–based composites. Moreover, the improvement of strain behaviors in the composites can be originated from a new phase boundary with ferroelectric–relaxor coexistence.

1.2. Aim and scope of research

Research aim:

The principle aim of this thesis work is improving the piezoelectric properties, and their temperature insensibility in lead–free KNN–based piezoelectric materials using the composite method, based on the phase coexistence. In order to serve that main goal, the following issues will be resolved:

- Stabilize the tetragonal phase in KNN ceramics.
- Define the pseudocubic phase and relaxor stabilization in $BaZrO_3$ –modified KNN.
- Produce the composites using two components, one in ferroelectric tetragonal phase and one in relaxor pseudocubic phase, then investigate the enhanced piezoelectric properties and temperature stability near MPB region, based on the high temperature crystal structure XRD.
- Propose a model of ferroelectric–relaxor coexistence, and explain the improvement of strain behaviors in the composites.

Research scope:

The solid solution $0.92(\text{Na}_{0.5}\text{K}_{0.5})\text{NbO}_3-(0.08-x)(\text{Bi}_{0.5}\text{Li}_{0.5})\text{TiO}_3-x\text{BaZrO}_3$ ternary system was investigated to study the features of morphotropic phase boundary.

The tetragonal phase is stabilized in $(1-x)(\text{Na}_{0.5}\text{K}_{0.5})\text{NbO}_3-x\text{SrTiO}_3$ piezoceramics at room temperature with the amount of SrTiO_3 modification higher than 0.05 mol%. However, when SrTiO_3 content further increases, the Curie temperature and piezoelectric properties are reduced. Therefore, $0.96(\text{K}_{0.5}\text{Na}_{0.5})_{1-y}\text{Li}_y\text{NbO}_3-0.04\text{SrTiO}_3$ piezoceramics system was also investigated.

Two systems of $(\text{K}_{0.5}\text{Na}_{0.5})(\text{Nb}_{1-x}\text{Zr}_x)\text{O}_3$ and $(1-y)(\text{Na}_{0.5}\text{K}_{0.5})\text{NbO}_3$ are compared to investigate the relaxor behaviors and clarify the stabilized phase in KNN-based ceramics. The pseudocubic phase can be found in KNN-100yBZ around room temperature with $y \geq 0.08$, corresponding with the relaxor stabilization.

Finally, two components of ferroelectric tetragonal KNN-4ST-4L and relaxor pseudocubic KNN-8BZ are mixed in different KNN-4ST-4L content fractions f . The crystal structure, microstructure, and other properties such as dielectric permittivity, ferroelectric polarization, bipolar strain, piezoelectric responses, etc. were carried out as well as the temperature stability.

1.3. Outline of the thesis

The thesis consists of five Chapters.

The background, research objectives and outline of this thesis are given in Chapter 1. Chapter 2 consists of two parts. The first part provides the basics ferroelectrics and their related properties applicable to the objectives of this research. The second

partments about the review of literature on lead-based piezoelectrics, lead-free piezoelectrics (BT –barium titanate, BNT –bismuth sodium titanate and KNN –sodium potassium niobate), phase boundaries and relaxor ferroelectricity in KNN-based materials. Chapter 3 presents the experimental procedure with particular compositions, detailed fabricating conditions and characterization techniques that had been used in this research work.

Chapter 4 is the main content in this study and includes five parts. An example of tetragonal–rhombohedral morphotropic phase boundary in $0.92(\text{Na}_{0.5}\text{K}_{0.5})\text{NbO}_3$ – $(0.08-x)(\text{Bi}_{0.5}\text{Li}_{0.5})\text{TiO}_3$ – $x\text{BaZrO}_3$ ternary system using conventional solid solution is considered in the first part. Next two parts investigate the effects of SrTiO_3 and Li^+ modification on the tetragonal stabilization of KNN-based ceramics. The fourth part determines the orthorhombic–pseudocubic polymorphic phase transition and ferroelectric–relaxor crossover in BaZrO_3 –modified KNN ceramics. The last part studies new phase boundary in the composites of ferroelectric tetragonal $0.96(\text{K}_{0.5}\text{Na}_{0.5})_{0.96}\text{Li}_{0.04}\text{NbO}_3$ – 0.04SrTiO_3 and relaxor pseudocubic $0.92\text{Na}_{0.5}\text{K}_{0.5}\text{NbO}_3$ – 0.08BaZrO_3 .

Finally, Chapter 5 presents the summary of this research work.

Chapter 2: Theory and literature review

2.1. Basics of ferroelectrics

2.1.1. Crystal symmetry

A point group is a group of symmetry operations all of which leave at least one point unmoved [15]. There are 32 three-dimensional crystallographic point groups (classes) for crystalline materials, which is reduced from 230 space groups by ignoring the translational repetition. Among them, 11 classes are centrosymmetric and 21 are non-centrosymmetric.

Since combined symmetry element, one of the non-centrosymmetric classes is does not render piezoelectric effect. Therefore, only 20 classes would perform the piezoelectric effects. Among them, 10 classes can exhibit piezoelectric as well as pyroelectric effects originating from their spontaneous polarization. Within these classes, there is a subgroup with spontaneous and reversible polarization, which shows all piezoelectric, pyroelectric, and ferroelectric effects. Meanwhile, remained 10 classes with internal stress induced polarization can show the piezoelectric effect only. The relatively classification of dielectrics, piezoelectrics, pyroelectrics and ferroelectrics are shown in Figure 2.1.

These 32 point groups can be also classified as seven basic crystal systems, according with the degree of symmetry. Seven basic crystal systems are triclinic, monoclinic, orthorhombic, tetragonal, trigonal (rhombohedral), hexagonal, and cubic. The corresponding classes for each system are listed in Table 1.

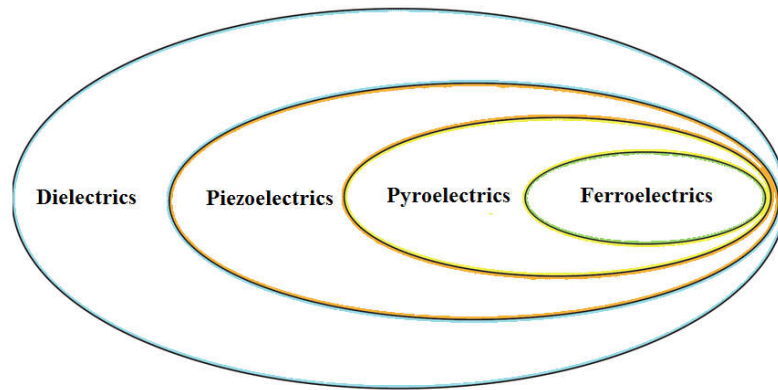


Figure 2.1. Relationship between dielectrics, piezoelectrics, pyroelectrics and ferroelectrics.

Table 1. 32 three-dimensional crystallographic point groups in crystals

Crystal system	Centrosymmetric	Non-centrosymmetric
Triclinic	$\bar{1}$	1
Monoclinic	2/m	2, m
Orthorhombic	mmm	222, mm2
Tetragonal	4/m, 4/mmm	4, $\bar{4}$, 422, 4mm, $\bar{4}2m$
Trigonal	$\bar{3}$, $\bar{3}m$	3, $\bar{3}2$, $\bar{3}m$
Hexagonal	6/m, 6/mmm	6, $\bar{6}$, 622, 6mm, $\bar{6}m2$
Cubic	m $\bar{3}$, m $\bar{3}m$	23, $\bar{4}3m$, 432

2.1.2. Dielectrics

Dielectrics (or dielectric materials) are electrical insulator which can be polarized by the applied electric field. Unlike metals, dielectrics have no free electrons through the material, practically causing no current flows even under electric field. Instead, electric polarization occurs in the dielectrics with the positive charges are displaced minutely in the direction of the electric field, and the negative charges in the opposite direction. This slight separation of charge, or polarization, generates the internal field and reduces the effects of external applied electric field. A common example of a dielectric is the

electrically insulating material between the metallic plates of a capacitor (Figure 2.2) increases the capacitor's surface charge for the given electric field strength. The presence of dielectric materials affects other electrical phenomena. Comparing with vacuum, dielectric medium can reduce the force between two electric charges but increase the quantity of energy stored in an electric field per unit volume. The capacitance C of a capacitor fulfilled with dielectric material is greater than the capacitance C_0 of a capacitor with vacuum (or air), follows the formula:

$$C = \frac{\epsilon\epsilon_0 A}{d} = \epsilon C_0$$

The factor ϵ is called as dielectric constant of the dielectric material. Effects of the dielectric on electrical phenomena are described on a macroscopic scale by employing such concepts as dielectric constant, permittivity, loss and polarization. Although the term insulator implies low electrical conduction, dielectric typically means materials with a high polarizability.

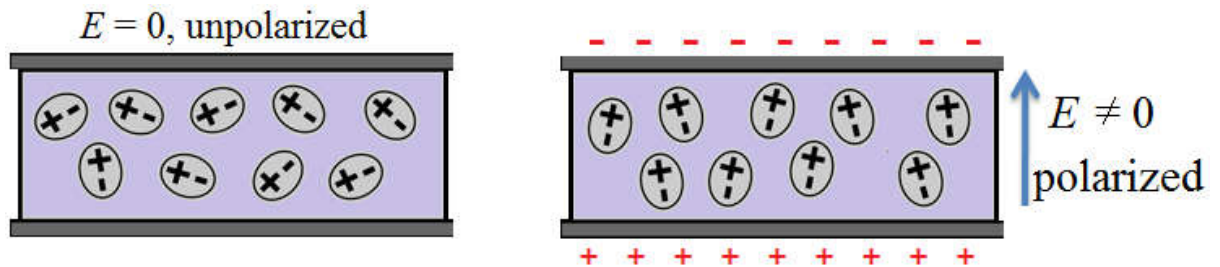


Figure 2.2. Polarization of dielectrics by an applied electric field.

2.1.3. Piezoelectrics

Piezoelectricity (also called the piezoelectric effect) is defined as the electric charge accumulating in certain solid materials under applied mechanical stress. The word

piezoelectricity means electricity resulting from pressure and latent heat. In 1880, the French physicists of Jacques and Pierre Curie firstly discovered the direct piezoelectricity in single-crystal quartz which can induce electrical charge/voltage under the pressure, and then Gabriel Lippmann (1881) observed the converse piezoelectric effect. The reversible piezoelectric effect can be defined as a linear electromechanical interaction between the mechanical and the electrical state of piezoelectric material. Under an applied mechanical force, electrical charges can be internally generated, cause the direct piezoelectric effect. In contrast, the internal generation of mechanical strain resulting from electric fields shows the reverse piezoelectric effect. Both effects are shown in Figure 2.3. History of piezoelectric materials follows the sequence of quartz, Rochelle salt, BaTiO_3 (BT), $\text{Pb}(\text{Zr,Ti})\text{O}_3$ (PZT), relaxor ferroelectrics, PVDF, lead-free piezoelectrics, and composites. According to environment issue, lead-free piezoelectric materials recently have been strongly developed to replace the lead-based ones.

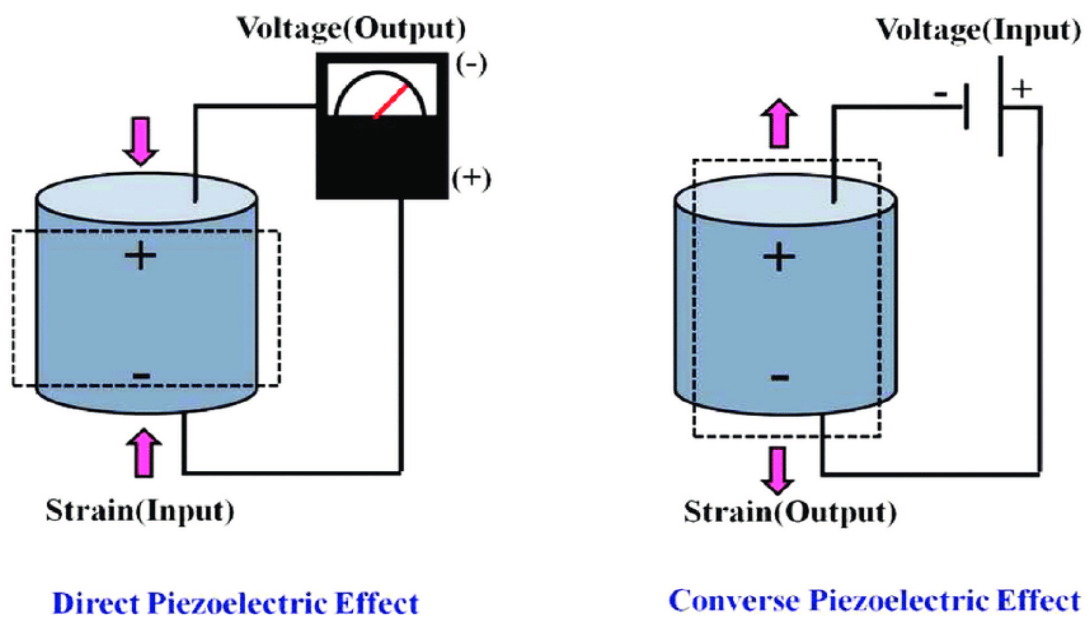


Figure 2.3. Sketch images for two piezoelectric effects [16].

2.1.4. Ferroelectrics

One of the most fascinating properties of dielectric materials is the ferroelectricity, a characteristic of certain materials that have a spontaneous electric polarization that can be reversed by the application of an external electric field. Materials exhibiting ferroelectric properties must possess reversible spontaneous polarization; they must also be either single crystals or polycrystalline solids composed of crystallites. The spontaneous polarization can be switched under an external electric field and maintains after removing of electric field [17]. In the case of polycrystalline ceramics, based on the distribution of the randomly oriented dipole moments, the net permanent dipole moment in the unit cell of ferroelectric materials does not translate immediately into a macroscopic polarization. Also in single crystals, the orientation distribution of the dipole moments is organized in groups called domains (areas with same dipole direction of individual adjacent unit cells) but not completely random on the unit cell level [18]. Though each domain have a net non-zero polarization, the macroscopic polarization of the material with a large number of domains arrange in random way can be zero. The interface between two domains is called domain wall [19], and the polarization of ferroelectric materials is based on the domain switching, or domain wall movement [20]. In Figure 2.4, the difference in domain structures with 180° domain wall and non- 180° domain wall (represented by 90° domain wall) causes the electric and elastic boundary conditions in ferroelectric materials [17]. All ferroelectrics are pyroelectric, therefore, piezoelectric (see Figure 2.1).

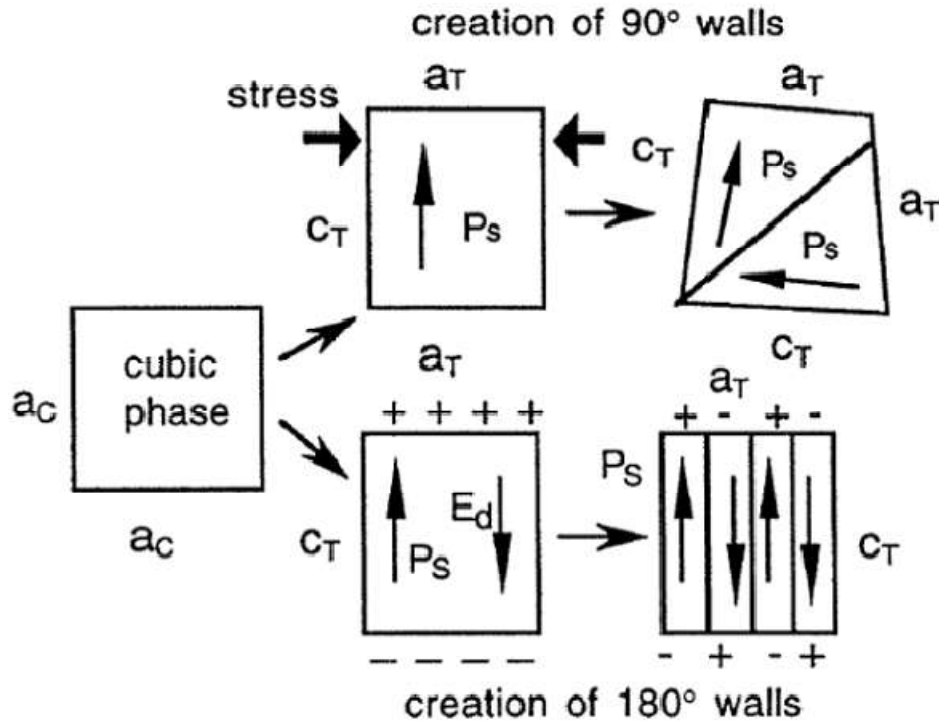


Figure 2.4. Electric and elastic boundary conditions in ferroelectric materials [17].

Polarization Switching and Hysteresis Loops

Important characteristics of ferroelectric materials are the polarization (domain) switching and ferroelectric hysteresis loop. Polarization switching is a reversible process in which the polarization can be reoriented in the direction of the electric field until parallel when an external field is applied in a direction opposite to the remnant polarization (domain) [20]. Domain switching is an extrinsic process, which can occur out of unit cell length scale. Consequently, the polarization loop of a ferroelectric material involves the nonlinear of polarization with electric field [21]. The polarization and strain hysteresis loop for ferroelectric materials are shown in Figure 2.5. Various values such as maximum polarization P_{max} , spontaneous polarization P_s , remnant polarization P_r , and coercive electric field E_c ... are also determined. At unpoled state, the

initial polarization and strain values ferroelectric material are macroscopic zero. When a high electric field is applied, the domain walls are oriented along the field direction and reach a saturation of polarization state, exhibit linear increase until all of the domains are aligned in that direction. When the electric field is removed, some domain walls will back-switch, a non-zero macroscopic remanent polarization P_r is observed since the polarization reduces but still maintains aligned domains. An electric field called the coercive field E_c must be applied in the opposite direction to cancel that polarization. The net polarization equals zero at the coercive field based on the randomness. Higher than Curie temperature, ferroelectric phase changes to paraelectric phase, in which both macroscopic and microscopic polarizations are invalid.

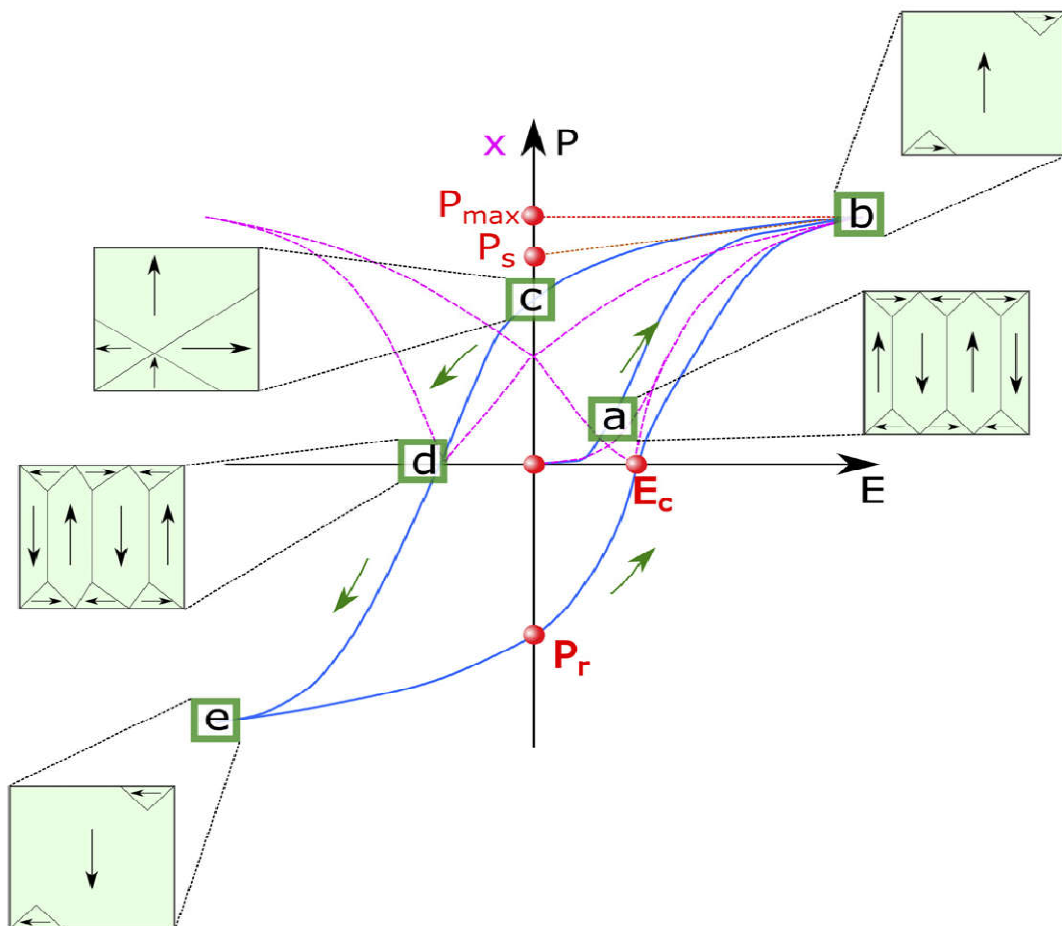


Figure 2.5. Polarization and strain versus electric field loops of ferroelectric crystal [21].

2.1.5. Perovskite structure

Perovskite structure ABO_3 is the most common group of ferroelectric materials, with hundreds of compositional modifications was currently formed using solid solution substitutions and/or dopants. Basically, a perovskite unit cell is structured from eight large A^{a+} ions (“ a ” is the valence of A, from 1 to 3), one small B^{b+} ion (“ b ” from 3 to 6), and six O^{2-} ions, respectively [22]. The perovskite unit cell can be pictured as a face centered cubic structure at elevated temperatures in

Figure 2.6 (a), where the A^{a+} ions sit on the corners of the unit cell, and the O^{2-} ions sit on the faces of the unit cell. The B^{b+} ion occupies the octahedral interstitial site. The A-site ions are coordinated by 12 O^{2-} ions, while the B-site ion is coordinated by six O^{2-} ions. Initially, this structure is neutral and symmetric, causes the non-polarized lattice and does not exhibit any piezoelectric properties. The structure in

Figure 2.6 (b) distorts into an off-centre and elongated structure, such as tetragonal, rhombohedral, orthorhombic, etc through the cooling to form a polar structure.

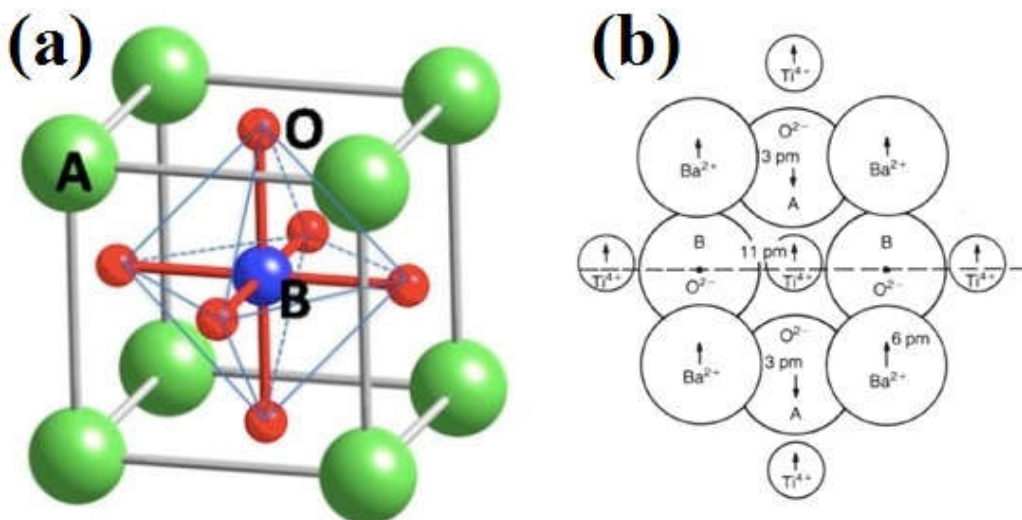


Figure 2.6. (a) Perovskite structure of unit cell and (b) ferroelectric BaTiO₃ [22].

2.2. Status of piezoelectric materials

2.2.1. Lead-based piezoelectric materials

The era of lead-based piezovskite materials started in 1950s and these materials become the most well-known compounds, which are now widely used in various electromechanical devices. The excellent and stable piezoelectric properties in PZT based on the morphotropic phase boundary was first discovered by Jaffe *et al.* [13] exhibit some of the of known compounds and Other candidates with high piezoelectric coefficients for academic and commercial requirements in different applications are lead magnesium niobate (PMN), and lead thanthanum zirconate titanate (PLZT). The properties of these typical lead-based material groups are briefly mentioned in the following subsections.

Lead zirconate titanate

Lead zirconate titanate (PZT) is the solid solution of PbZrO_3 (PZ) and PbTiO_3 (PT), which was reported by Shirane, Suzuki, and Takedal in 1952 [23]. The mixing of orthorhombic structure anti-ferroelectric PZ and tetragonal structure ferroelectric PT forms the compositions of PZT with the performance of the morphotropic phase boundary (Figure 2.7) near 45 mol% of PT [1,13]. Unlike ferroelectric with domains of polarization, the anti-ferroelectric materials are not piezoelectric since they contain the spontaneous electric polarization in anti-parallel direction and cancel out each other due to the net polarization is zero. Binary PZ-PT solid solution exhibits good piezoelectric and ferroelectric properties. With increase of PT content, the structure undergoes a phase transition from an anti-ferroelectric orthorhombic phase with non-polar state to a ferroelectric tetragonal phase with the spontaneous polarization is along the $\langle 100 \rangle$ direction. When cooling down, the rhombohedral crystal structure can be formed with the polarization is along the $\langle 111 \rangle$ direction.

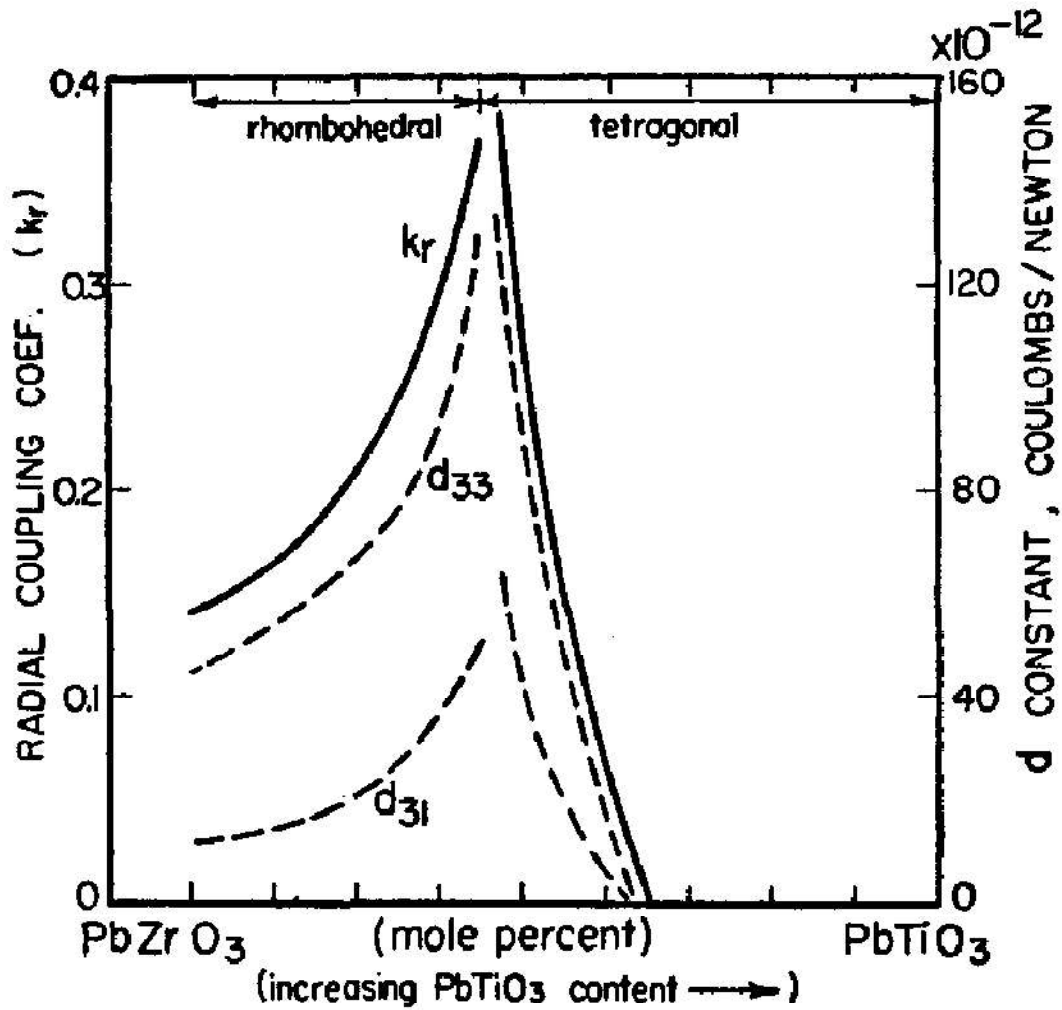


Figure 2.7. Electromechanical properties of PbZrO₃-PbTiO₃ solid-solution ceramics on composition.

Figure 2.8 describes the overall phase diagram PZT ceramics, respected to the composition and temperature [24]. At high PbZrO₃-rich phase (≥ 95 mol%), PZT shows the anti-ferroelectric orthorhombic phase with double hysteresis loop in polarization [25]. Increase the PT amount up to 47 mol%, the crystal structure transits to ferroelectric rhombohedral phase with 2 types: F_R(L) at low temperature with $R3c$ symmetry, and F_R(H) at high temperature with $R3m$ symmetry. For the PbTiO₃-rich region, ferroelectric

tetragonal phase is stable and PZT with around 0.45–0.47 mol% of PT performs a morphotropic phase boundary with nearly vertical boundary of rhombohedral ($R3m$) and tetragonal ($P4mm$) coexistence. PZT shows excellent piezoelectric properties and temperature independence at this MPB region. At higher than the Curie temperature T_C , ferroelectric rhombohedral and/or tetragonal phase crystallizes to paraelectric cubic structure.

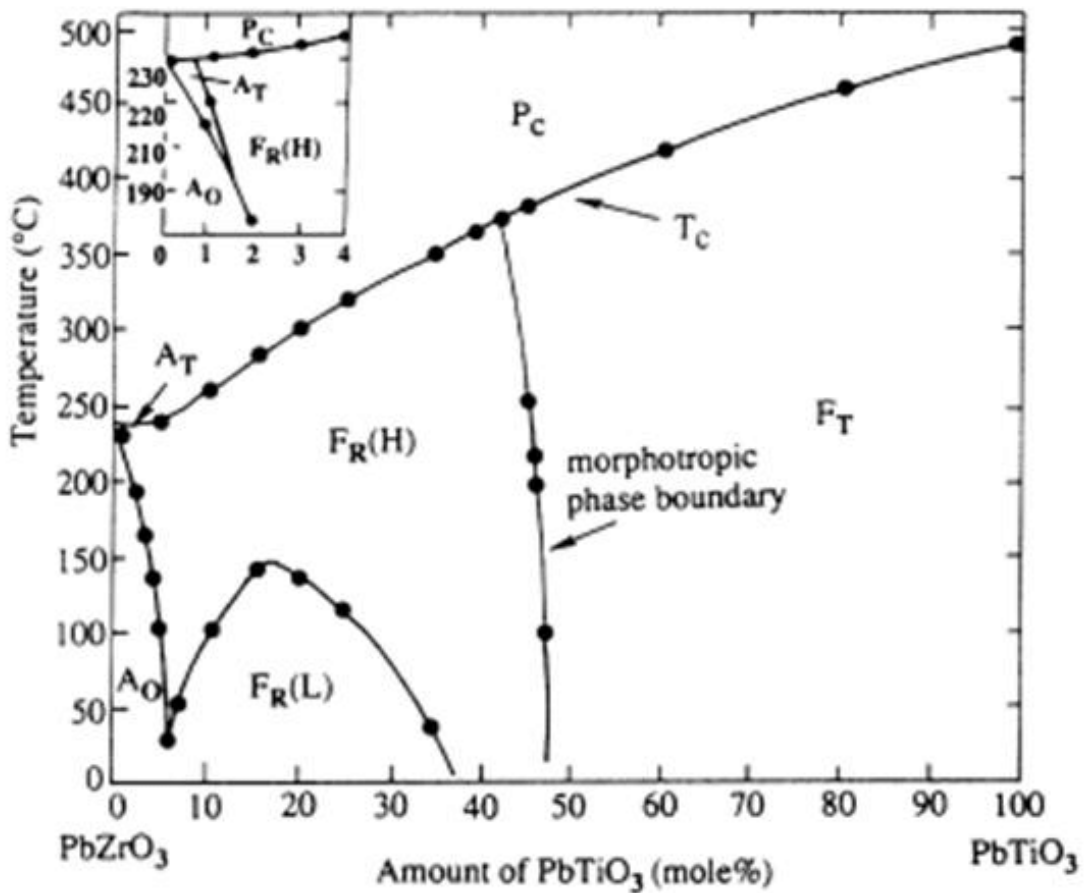


Figure 2.8. Phase diagram of the PbZrO_3 – PbTiO_3 solid solution system. [24]

To improve the piezoelectric properties in PZT ceramics, there were many studies on MPB composition with chemical modification. Acceptor dopants, such as K^+ , Na^+ (for

A-site) and Fe³⁺, Al³⁺, Mn³⁺ (for B-site), cause the hard PZT with lower permittivity, smaller electrical loss, and lower piezoelectric coefficients [26]. In contrast, donor dopants such as La³⁺ (for A-site) and Nb⁵⁺, Sb⁵⁺ (for B-site) generate the soft PZT with higher permittivity, larger loss, higher piezoelectric coefficient and is easy to pole and depoled [27].

Lead magnesium niobate

Lead magnesium niobate (PMN) was first introduced on 1961 by Smolenskii *et al.* with the dispersive and broad dielectric permittivity signal, namely the diffuse phase transition [28]. This work can be considered as the first report on relaxor ferroelectrics. PMN is a representative of class of lead-based perovskite class with the Pb(B₁,B₂)O₃ formula where cation B₁ (like Mg²⁺, Zn²⁺, Ni²⁺, Fe³⁺) has lower valence than B₂ (Nb⁵⁺, Ta⁵⁺, W⁵⁺). Relaxor ferroelectric PMN shows a very high and strong frequency-dependent dielectric constant near room temperature and low temperature. The mechanism of diffused phase transitions in PMN can be related with the B-site distortion based on the compositional heterogeneity [29]. At higher frequencies, the maxima in dielectric constant at Curie temperature T_C shift to higher temperatures.

Recently, PMN and PMN-based materials received much attention for applications which require not only good electrostrictive strain, but also large dielectric constant [30]. With the addition of PbTiO₃, the piezoelectric MPB composition 0.65PMN–0.35PbTiO₃ shows the excellent piezoelectric properties for transducers. Meanwhile, 0.95PMN–0.05PbTiO₃ has very large dielectric constant with a Curie point near room temperature, and nearly double for 10 mol% of PT-modified PMN (Figure 2.9).

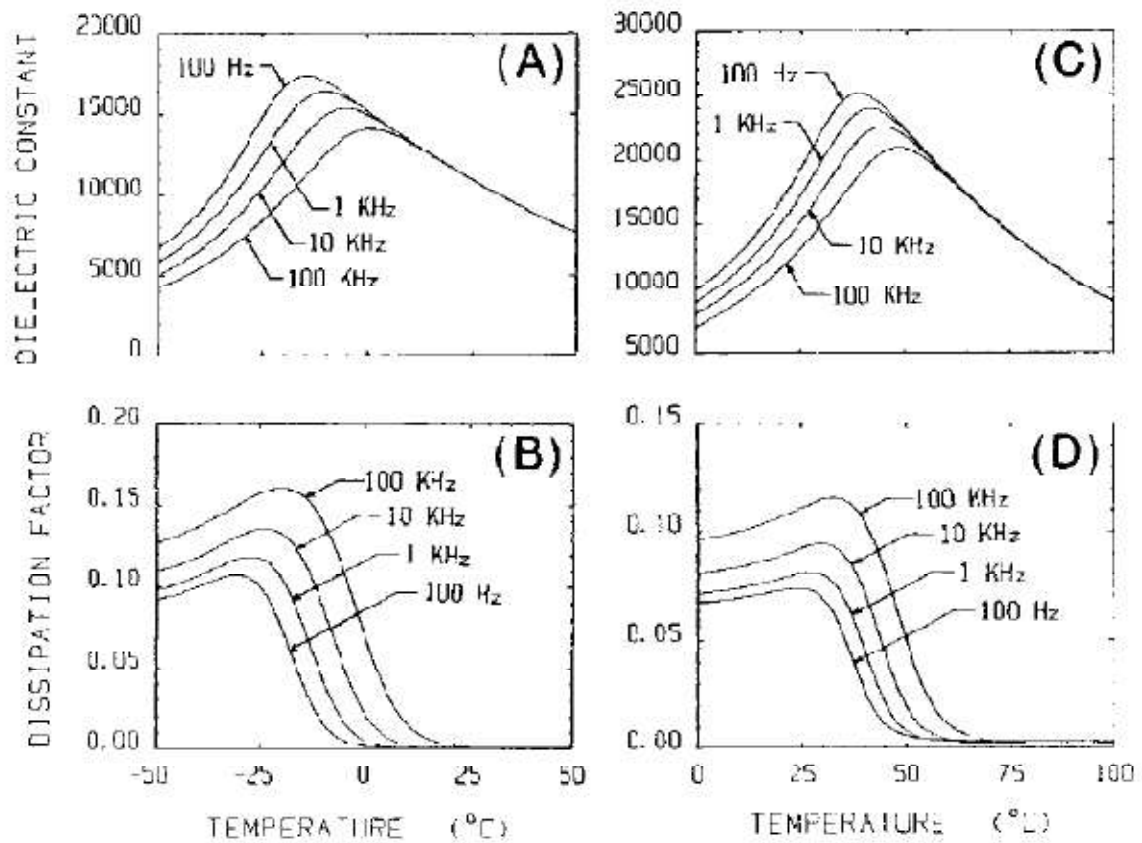


Figure 2.9. Temperature dependent dielectric constant and dissipation factor of PMN and PMN-10PT compositions. [30]

Lead lanthanum zirconate titanate

Translucent lanthanum doped lead zirconate titanate (PLZT) was fabricated with hot-press sintering method [31]. This is a transparent ferroelectric ceramic of same perovskite structure as PZT, and used in electro-optic applications to replace single crystals [3].

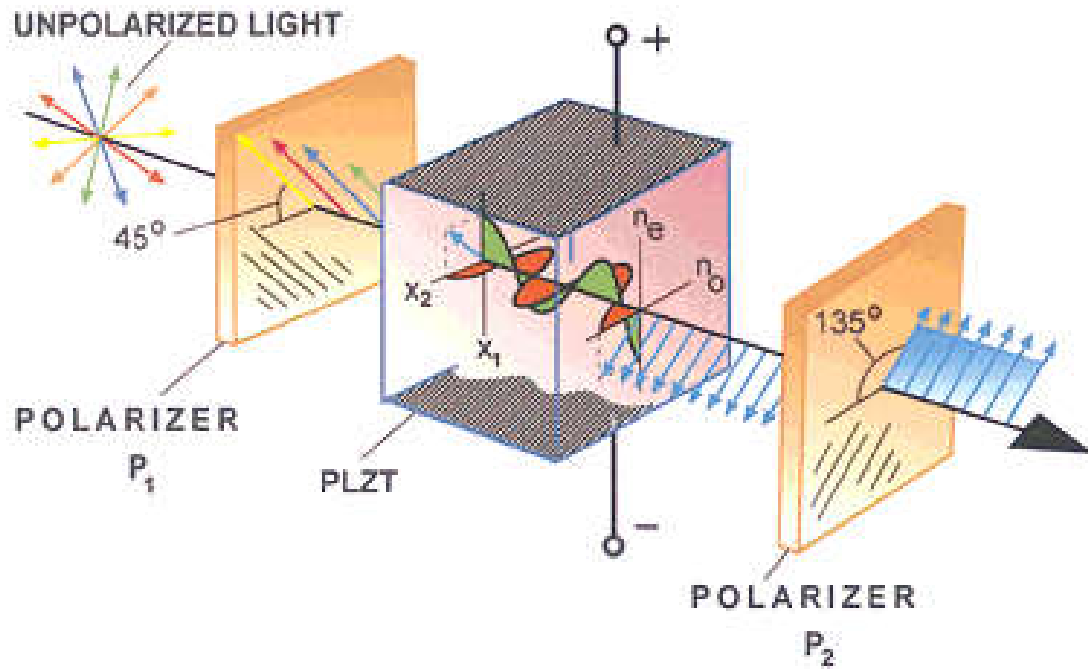


Figure 2.10. Basic setup for evaluating electrooptic shutter/modulator characteristics [31].

Relaxor behavior can be observed in PLZT ceramic compositions with a diffused, frequency-dependent permittivity maximum. For PLZT 4/85/15, the relaxation spectrum can be characterized by a slim hysteresis loop and much broader than Debye-type. A relaxor-like state with dielectric behavior and nano-domains in $100x/85/15$ was improved with increasing La content x . On the other hand, the composition 6/85/15 performs an anti-ferroelectric behavior with nano-domains. In high La content rhombohedral PLZT ceramics, the order within the nanodomain state is suggested to be anti-polar over a range of compositions [32].

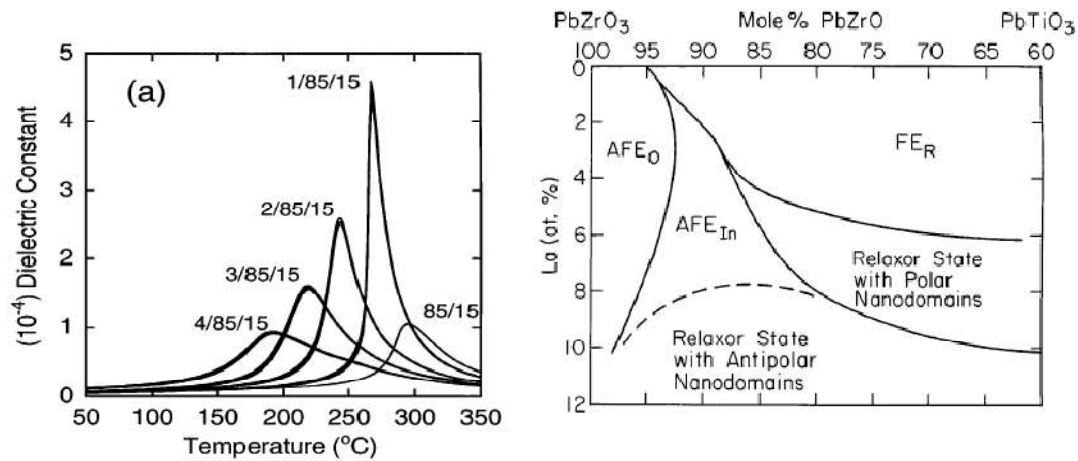


Figure 2.11. Temperature dependent dielectric constant and phase diagram of PLZT [32].

2.2.2. Lead-free piezoelectric materials

Lead-based materials contain high amount of lead (Pb), one of the most toxic element, which causes serious environmental and health problems, especially for children. Recently, lead-free piezoelectric ceramics have received much research attention to replace the current lead-based materials [4]. The lead-free piezoelectric ceramics candidate for ceramic filter and resonator applications can be divided into two main types, based on the basic of structure: (i) perovskite, and (ii) tungsten bronze. These materials show high Curie temperature, high mechanical quality, low permittivity, and low piezoelectric response, related with 2-dimensional restrictions on the permissible rotation of the spontaneous polarization. Besides, perovskite piezoelectric materials show high piezoelectric properties readily forms solid solutions with high possibilities of new compounds and interesting compositions. The mechanisms by which the additives alter the desired properties are still remaining challenges.

Basically, lead-free piezoelectric ceramics can be classified as three big groups, namely barium titanate (BaTiO₃ or BT), bismuth sodium titanate (Bi_{0.5}Na_{0.5}TiO₃ or BNT), and

potassium sodium niobate ($\text{K}_{0.5}\text{Na}_{0.5}\text{NbO}_3$ or KNN). In the following, a brief review of these different material groups have given in the following section. According to the researches of lead-free piezoelectric materials, the construction of phase boundaries is very effective to promote piezoelectric properties. For example, the d_{33} can be enhanced in BaTiO_3 by constructing R-T phase boundary, but a low T_C (< 100 °C) is often shown. Moreover, the phase boundaries of most lead-free materials are often sensitive to both temperature and composition. Although the MPB can be constructed in the $\text{Bi}_{0.5}\text{Na}_{0.5}\text{TiO}_3$ -based ceramics, the poor d_{33} and a low T_d seriously limited its practical applications. Our group recently improved the piezoelectricity of $(\text{K},\text{Na})\text{NbO}_3$ -based ceramics by constructing new phase boundary, with the good temperature insensitivity of d_{33} .

Barium titanate

The first investigated ferroelectric oxide with perovskite structure was barium titanate BaTiO_3 (BT), which has a relatively high electromechanical coupling factor k_{33} . Figure 2.12 describes the phase transitions of BT respected to the change of temperature. Start at rhombohedral from low temperature, the rhombohedral-orthorhombic phase transitions is detected near -76°C , then orthorhombic-tetragonal around below room temperature, and tetragonal-cubic at 120°C [33]. BT and its compounds have been widely used for piezoelectric sensors, capacitors, memories, and optical devices because of their fascinating electric and piezoelectric properties. At 1460°C , perovskite BT tranforms to hexagonal structure, and then melts near 1620°C .

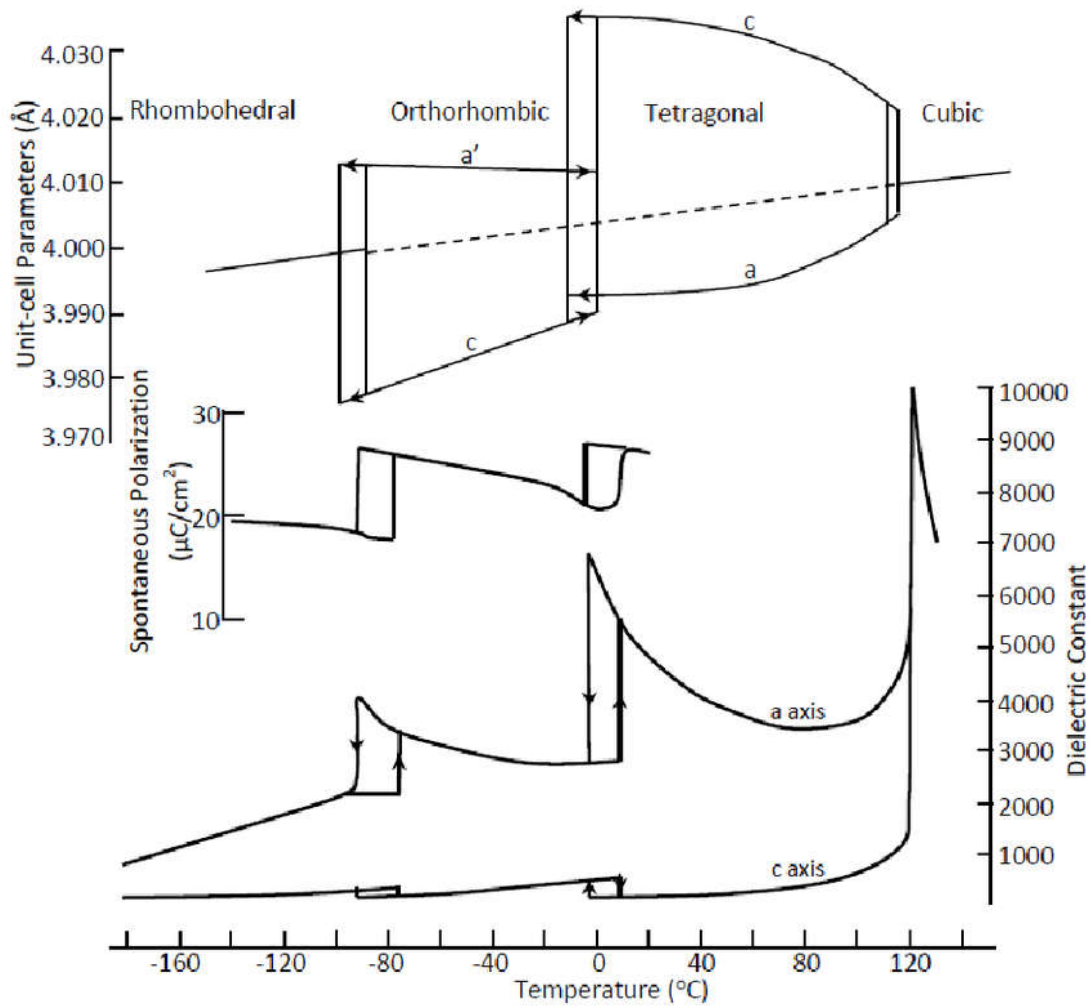


Figure 2.12. Polymorphic phase transitions in barium titanate single crystals [33].

In 2009, a high piezoelectric coefficient of $d_{33} \approx 620$ pC/N was showed in lead-free piezoceramic system of $\text{Ba}(\text{Ti}_{0.8}\text{Zr}_{0.2})\text{O}_3-(\text{Ba}_{0.7}\text{Ca}_{0.3})\text{TiO}_3$ by the construction of phase boundaries using the chemical modifications [40], which greatly motivated further investigations of the whole solid solutions containing BT. It was reported that a MPB consisted of a tricritical triple point of a cubic paraelectric phase (C), ferroelectric rhombohedral (R) and tetragonal (T) phases according to the temperature dependence of dielectric properties, which was responsible for the high piezoelectricity [34]. Keeble *et al.* [35] studied the phase diagram of $\text{Ba}(\text{Ti}_{0.8}\text{Zr}_{0.2})\text{O}_3-(\text{Ba}_{0.7}\text{Ca}_{0.3})\text{TiO}_3$ ceramics using the high-resolution synchrotron X-ray diffraction, and the intermediate

orthorhombic phase bridging T–R can be observed in the same material system. Therefore, the polarization rotation between R and T phases through the intermediate phase can result in the strong piezoelectric properties. Although some disputes concerned about the types of phase boundaries, the piezoelectric properties can be always enhanced. The superior piezoelectricity can be revealed in BaTiO₃–based ceramics, which is comparable with soft PZT. We have to point out that the material system has the drawback of low Curie temperature ($T_C < 130\text{ }^\circ\text{C}$), restricting its application for its temperature stability performance. However, it can be thought as an excellent model system for exploring the physical mechanisms of high performance Pb–free piezoelectric materials.

Bismuth sodium titanate

After BT, bismuth sodium titanate Bi_{0.5}Na_{0.5}TiO₃ (BNT) is the next most important lead–free materials, which was strongly used in many piezoelectric applications, especially for actuators. The perovskites form of the BNT ceramics is (A₁A₂)BO₃ with complex A–site of Bi³⁺ and Na⁺, and Ti⁴⁺ on the B–site [25]. At room temperature, BNT ceramic has a rhombohedral and monoclinic crystal structure [36]. Pure BNT ceramic shows strong ferroelectric [37], but has problem in the poling process because of high conductivity, high leakage current, and large coercive field. Otherwise, related with vaporization of Bi³⁺ ions occurred during the sintering process, BNT ceramic requires a high sintering temperature above 1200°C.

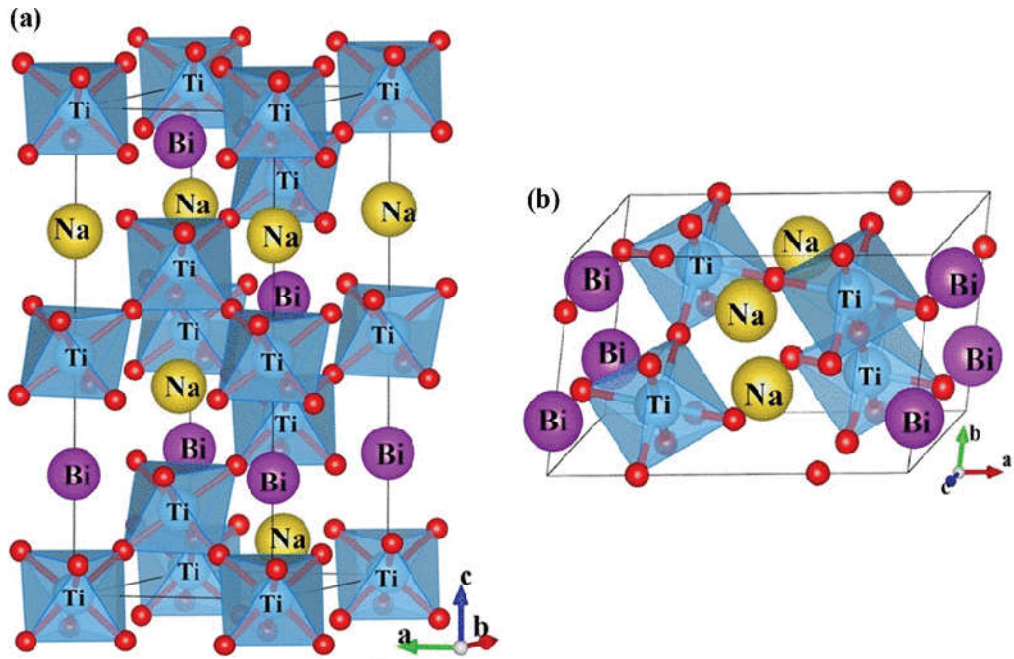


Figure 2.13. Possible crystal models of BNT [36].

One potential branch of BNT materials is SrTiO₃ modification, namely BNST ceramics. Based on the temperature dependent permittivity and ferroelectric properties, BNT ceramic can be considered as ferroelectrics (nonergodic relaxor) and ergodic relaxors [7]. The phase transition at 26 mol% of SrTiO₃ offers the high strain $d_{33}^* \approx 600$ pm/V under 4 kV/mm, and the low poling field around 2 kV/mm give BNST system a competitive advantage of larger strain under lower operating field compared with other BNT-based lead-free piezoelectric ceramics.

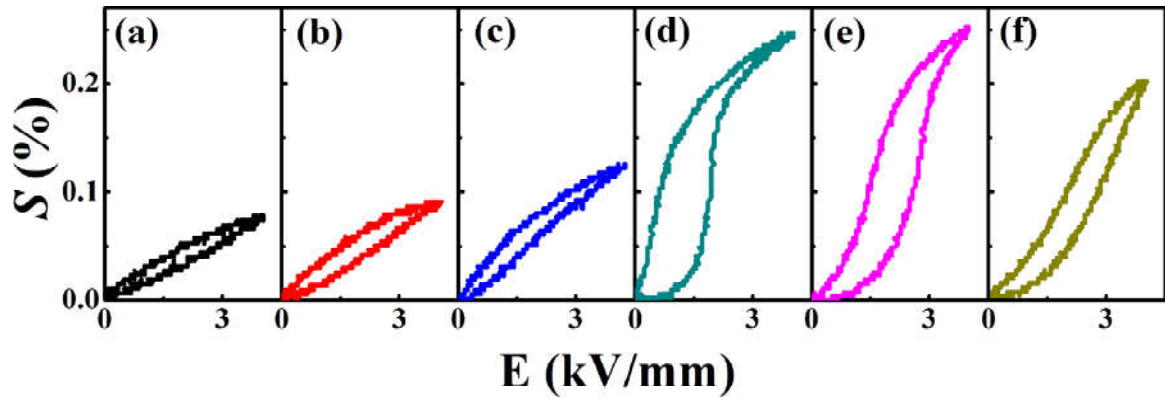


Figure 2.14. Electric field–induced unipolar strain curves for BNST ceramics [7].

Sodium potassium niobate

Lead–free sodium potassium niobate piezoelectric materials are the solid solution of ferroelectric KNbO_3 and the anti–ferroelectric NaNbO_3 , with the phase diagram is shown in Figure 2.15 [38]. Among the compositions, $\text{K}_{0.5}\text{Na}_{0.5}\text{NbO}_3$ (KNN) are the promising candidates for sensors and energy harvesting applications because of their excellent dielectric and piezoelectric properties. Pure KNN ceramics have rhombohedral–orthorhombic phase transition below room temperatures, orthorhombic–tetragonal phase transition at 210°C and tetragonal–cubic near 420°C [39]. Normally, KNN ceramics sintered by conventional method have the piezoelectric constant d_{33} of 80 pC/N, electromechanical coupling factor k_p of 0.36, and mechanical quality factor Q_m of 130.

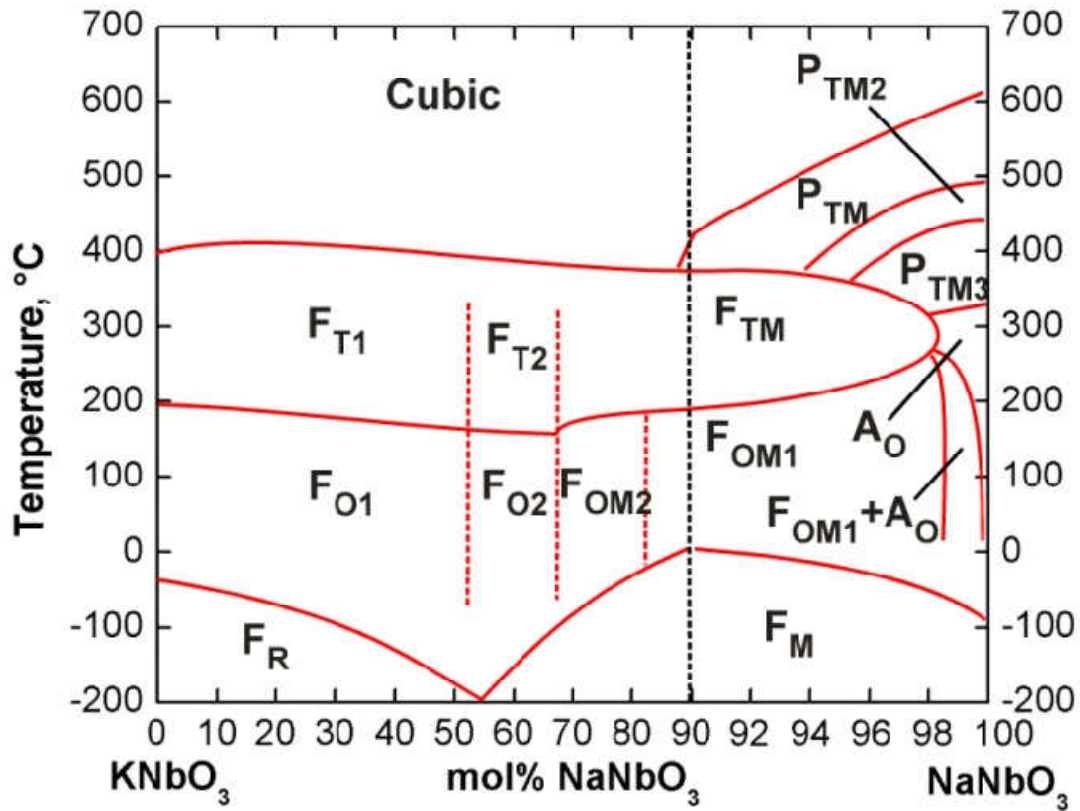


Figure 2.15. Phase diagram of the KNN solid solution [39].

However, the conventional sintering in air brings a problem when forming high density samples, causes the induced porosities and poor densification in specimen. The formation of extra phases like $K_4Nb_6O_{17}$ and an extremely narrow sintering-temperature range are also disadvantages [40]. Therefore, various techniques such as hot pressing, hot forging and spark plasma sintering can be effective methods for enhancing the density of KNN ceramics. Higher density and a more uniform microstructure of KNN ceramics have been reported when sintered in reducing conditions or inert atmospheres, rather than in air or oxygen [38].

2.2.3. Phase boundaries in KNN-based materials

Polymorphic phase boundary, PPB

In the region of multiphase coexistence, a high degree of alignments of ferroelectric dipoles can be driven by the thermodynamically-equivalent states under the electric fields during the poling process, easily resulting in the piezoelectricity enhancement. Recently, it has been thought that the free energy instability in phase boundaries is proposed to interpret the enhancement of piezoelectric properties. Phase boundaries in KNN depend on not only compositions but also temperatures. Most researchers define the O-T phase boundary of KNN as the intrinsic characteristics of “polymorphic phase transition (PPT)”. Even if the phase boundaries of KNN belong to be PPT characteristics, the piezoelectricity can be well enhanced when the compositions approach the phase boundaries because of the polarization rotation and polarization extension. The O-T phase boundary can be well constructed by moving T_{O-T} using the chemical modifications, such as BiScO₃ [41], MTiO₃ (with M = Pb, Ba, Sr, Ca, Bi_{0.5}Li_{0.5}...) [42,43], LiMeO₃ (with Me = Nb, Ta, Sb...) [44-46]. Unfortunately the R-O phase boundary is often ignored due to low d_{33} . Some elements can be employed to form the R-O phase boundary in KNN by bringing the T_{R-O} to above room temperature, such as AZrO₃ (A = Ba, Ca, Sr) [47,48], Sb⁵⁺ [49,50] and BiScO₃ [51].

However, the PPT approach leads to a temperature sensitivity problem because the phase boundary corresponding to R-O or O-T possesses the PPT characteristic depending on not only the compositions but also the temperature. There are several typical KNN-based ceramics systems that perform the R-O or O-T PPT behaviors. A general phase diagram for the PPB is sketched in Figure 2.16 (a).

Table 2. Polymorphic phase boundary in KNN-based materials

Materials	T_C ($^{\circ}\text{C}$)	Phase transition	d_{33} (pC/N)	k_p
$(1-x)\text{KNN}-x\text{SrTiO}_3$ [52]	280	O-T	195	0.37
$(\text{K}_{0.5-x/2}\text{Na}_{0.5-x/2}\text{Li}_x)(\text{Nb}_{1-y}\text{Ta}_y)\text{O}_3$ [53]	310	O-T	190	0.46
$(\text{Na}_{0.5}\text{K}_{0.5})_{1-x}(\text{LiSb})_x\text{Nb}_{1-x}\text{O}_3$ [54]	390	O-T	260	0.5
$(1-x)\text{KNN}-x(\text{Bi}_{0.5}\text{Na}_{0.5})\text{TiO}_3$ [55]	375	O-T	195	0.43
$(1-x)\text{KNN}-x\text{CaZrO}_3$ [56]	320	R-O	154	0.32
$(1-x)\text{KNN}-x\text{BiScO}_3$ [57]	350	R-O	210	0.45
$(1-x)\text{KNN}-x\text{BaZrO}_3$ [47]	220	R-O	~	~

Morphotropic phase boundary, MPB

To prevent above problem, another concept was pointed out, namely morphotropic phase boundary (MPB). The MPB is the nearly vertical phase boundary separating rhombohedral, tetragonal, and/or monoclinic ferroelectric phases and nearly temperature independent. Recently, there were some studies to construct MPB in lead-free piezoelectric ceramics [58-62], especially, in KNN-based materials. Liu *et al.* [14] introduced a way of forming MPB by shifting diffused R-O and O-T phase transition closer to create a partially overlapped phase transition over a broad temperature range. Another approximation to form an MPB was using two end members, one with tetragonal symmetry and the other with rhombohedral symmetry at room temperature [25]. Figure 2.16 (b) shows the phase diagram of a typical rhombohedral-tetragonal MPB.

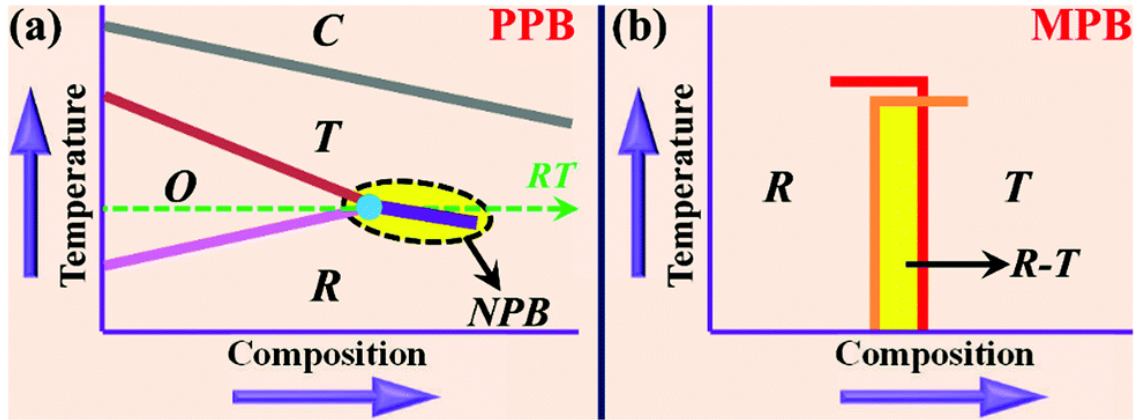


Figure 2.16. Intrinsic traits of (a) the polymorphic phase boundary and (b) the morphotropic phase boundary [63].

Table 3 summarizes the influences of different additives on the phase transition temperatures of KNN materials. Most of additives can simultaneously increase T_{R-O} and decrease T_{O-T} of KNN [47-49,56,57,64], and then the formation of new phase boundaries may become possible if their contents can be tailored.

Table 3. Effect of 1 mol% additives on the phase transition temperatures of KNN ceramics

Modification	Li [56]	Ta [64]	Sb [49]	CaZrO ₃ [56]	BaZrO ₃ [47]	SrZrO ₃ [48]	Bi _{0.5} Na _{0.5} ZrO ₃ [65]	Bi _{0.5} Na _{0.5} TiO ₃ [66]
T_C (°C)	+10	-6.5	-25.1	-28.0	-28.0	-32.0	-26	-14
T_{O-T} (°C)	-30	-4.0	-10.7	-11.0	-7.0	-13.0	-25	-5
T_{R-O} (°C)	-	+2.3	+14.8	+17.0	+19.0	+19.0	+4	+10

2.2.4. Relaxor ferroelectricity in KNN-based materials

First mentioned in 1950s with PMN, relaxor ferroelectrics (short called as relaxors) performed some abnormal dielectric permittivity behaviors [28]. In contrast with normal ferroelectrics, relaxor shows broad and higher frequency dispersive maxima. A brief

comparison was introduced by Li *et al.* [67] and partially shown in Figure 2.17. Several models, such as diffuse phase transition model, dipolar glass model, random field model, and etc., have been studied to explain the origin of relaxor features.

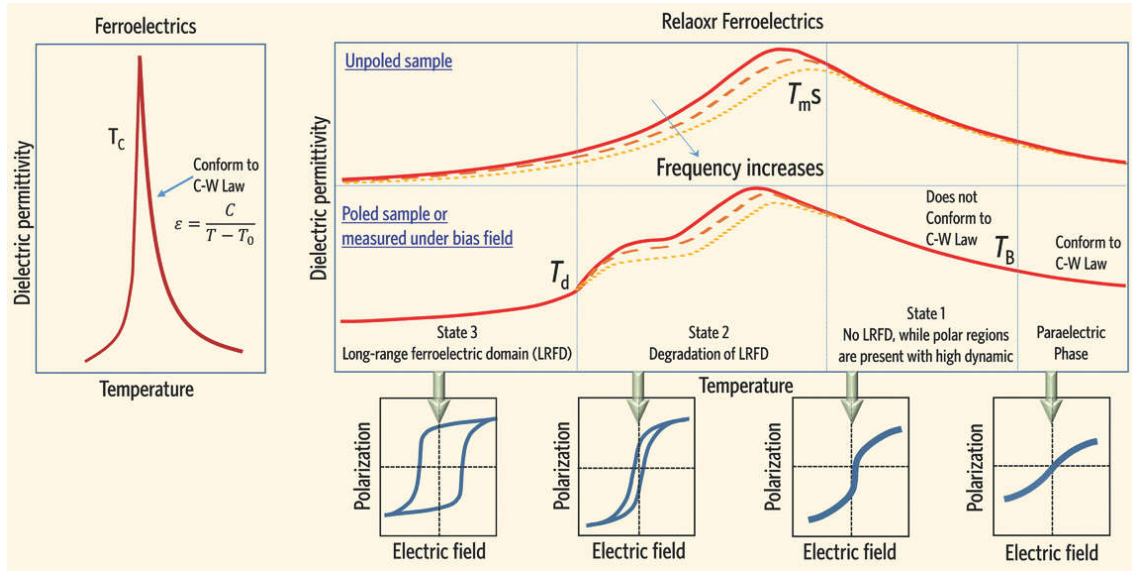


Figure 2.17. Characteristics of relaxor ferroelectrics as compared to normal ferroelectrics [67].

Recently, some studies paid their attention on the stabilization of a relaxor based on noncubic (more precisely, orthorhombic or tetragonal) phases that transit to pseudocubic phases [68-73]. The KNN-based relaxors exhibit some features, such as the extremely broad maximum in temperature dependent permittivity, diffuse phase transitions, and Vogel-Fulcher relaxations [74]. Guo *et al.* [75] firstly suggested that Sr^{2+} and Ti^{4+} co-doping in KNN ceramics can induce phase transition from the normal ferroelectric to relaxor ferroelectric with the diffuse phase transition behaviors. Kosec *et al.* [76] and Bobnar *et al.* [77] observed the relaxor behavior through a broad dispersive dielectric maximum and a Vogel-Fulcher relationship in KNN-SrTiO₃ ceramics. These relaxor features has been also observed in other KNN-based ceramics systems such as KNN-BaTiO₃ [78,79], KNN-Bi_{0.5}Na_{0.5}TiO₃ [80], KNN-BiFeO₃ [81], KNN-SrZrO₃ [82], and so on.

In fact, several studies on lead-based materials considered the tetragonal and pseudocubic phase in ferroelectric relaxor behaviors as MPB [83,84], while most of studies on lead-free piezoceramics mentioned them as PPT [71,85,86]. The enhancement of piezoelectric constant and/or electromechanical strain can be observed; however, the temperature stability of piezoelectric properties was not mentioned.

Chapter 3: Experimental procedure and characterization

3.1. Materials synthesis

3.1.1. Powders processing

Compositions

Five different systems of powders were investigated:

1) $0.92(\text{Na}_{0.5}\text{K}_{0.5})\text{NbO}_3 - (0.08-x)(\text{Bi}_{0.5}\text{Li}_{0.5})\text{TiO}_3 - x\text{BaZrO}_3$ ($x = 0.04, 0.05, 0.06, 0.07,$ and 0.08), abbreviated KNN-BLT-100x BZ.

2) $(1-x)\text{Na}_{0.5}\text{K}_{0.5}\text{NbO}_3 - x\text{SrTiO}_3$ ($x = 0, 0.01, 0.03, 0.04, 0.05, 0.06, 0.07, 0.10$), abbreviated KNN-100x ST.

3) $0.96(\text{K}_{0.5}\text{Na}_{0.5})_{1-y}\text{Li}_y\text{NbO}_3 - 0.04\text{SrTiO}_3$ ($y = 0, 0.01, 0.02, 0.03, 0.04, 0.05, 0.06$) ($x = 0; 0.01; 0.02; 0.03; 0.04; \text{ and } 0.05$), abbreviated KNN-4ST-100y L.

4) $(\text{K}_{0.5}\text{Na}_{0.5})(\text{Nb}_{1-x}\text{Zr}_x)\text{O}_3$ ($x = 0, 0.01, 0.05$), abbreviated KNN-100x Z.

5) $(1-y)(\text{Na}_{0.5}\text{K}_{0.5})\text{NbO}_3 - y\text{BaZrO}_3$ ($y = 0, 0.03, 0.06, 0.08, 0.10, 0.15$), abbreviated KNN-100y BZ.

Raw materials

Commercially available reagent grade metal oxide and carbonate powders were used to fabricate above compositions as the raw materials. They are carbonate powders Na_2CO_3 (99%), K_2CO_3 (99%), SrCO_3 (99.9%), Li_2CO_3 (99.99%), BaCO_3 (99.95%) and oxide powders Nb_2O_5 (99.9%), TiO_2 (99.99%), ZrO_2 (98%), Bi_2O_3 (99%).

These powders were dried in an oven at 100°C for at least 12h to remove any moisture and then weighed according to stoichiometric formula.

Milling and drying

After weighing to make the 20g-batch for each composition, the mixtures of raw materials were separately milled with 60g Zirconia balls and 80ml ethanol inside a polyethylene bottle at the rate of 350 rpm for 24h. During this process, each mixture was mixed thoroughly to form a uniform slurry. Then, the wet slurries were dried at 100°C for 24h.

The two times of calcination had been applied for these well-mixed powders. After each calcinating time, the resulting powders were milled and dried again. Beside the mixing purpose, the milling process also fracture, flatten and reweld the calcined powders to reduce the particle size, based on the ball-ball and ball-bottle wall collisions.

Calcinations

Each system of powders were calcined two times at different conditions as shown in Table 4. All compositions were covered in alumina crucibles, heated with rate of 5°C/min, kept at calcinated temperature T_{cal} for soaking time t_{cal} and naturally cooled in the furnace. The sketch of calcination process is provided in Figure 3.1 (a).

Table 4. Conditions for calcination and sintering.

System	T_{cal} (°C)	t_{cal} (h)	T_{sin} (°C)	t_{sin} (h)
KNN-BLT-100xBZ	1000	5	1080-1180	3
KNN-100xST	950	5	1110-1220	3
KNN-4ST-100yL	950	5	1120-1200	3
KNN-100xZ	850	3	1110-1200	3
KNN-100yBZ	850	3	1110-1220	3

3.1.2. Ceramics processing

Pellet preparation

After calcinations, the powders were added with an organic binder polyvinyl alcohol (PVA, 10%). To get uniform and fined grain, the granules were passed through a 150 μm sieve. Pellets of 0.4g were made by using a 10 mm–diameter cylindrical steal mold. The powder were uniaxially pressed with a pressure of 98 MPa in a hydraulic press, holding for 10 second. The green pellets were then surrounded by the sacrificed powders and sintered.

Sintering

The sintering process is described in Figure 3.1 (b), following the conditions shown in Table 4. The pellets of the prepared compositions were put in alumina crucible and were taken in to the furnace for sintering with the increased temperature rate of $5^\circ\text{C}/\text{min}$. The temperature were increased to 550°C and maintained there for 2h to remove all PVA binders, before heating up to the designed sintering temperature.

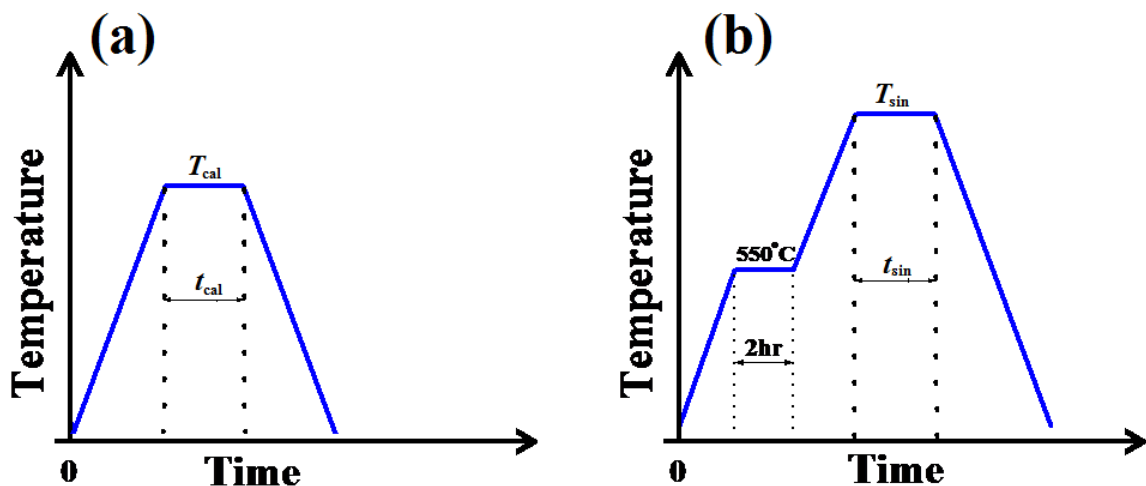


Figure 3.1. The sketch of (a) calcination and (b) sintering process.

3.1.3. Composites processing

Compositions

For composite specimens, two different calcined compositions were used:

[1] $0.96(\text{K}_{0.5}\text{Na}_{0.5})_{0.96}\text{Li}_{0.04}\text{NbO}_3-0.04\text{SrTiO}_3$, as a seed phase or T-phase component.

[2] $0.92\text{Na}_{0.5}\text{K}_{0.5}\text{NbO}_3-0.08\text{BaZrO}_3$, as a matrix phase, or PC-phase component.

These composites were mixed in different T-phase content fractions f ($f = 0, 0.1, 0.3, 0.5, 0.7, 0.9, 1.0$).

Pellet preparation and sintering

Similar with ceramics processing, the calcined powders were weighed for different ratios, mixed with PVA, sieved, pressed, and then sintered. All composites were sintered at 1180°C for 3h.

3.2. Characterization

3.2.1. Density measurement

Density of the as sintered ceramic pellets was measured by using Archimedes' immersion principle method using an electronic densimeter (SD-120L). First the mass of the pellets was measured and then sample was immersed in DI water, where it displaced an amount of water equal to its own volume and its weight is apparently diminished by the weight of the liquid displaced. The density ρ of sample was calculated from the relation:

$$\rho = \frac{\rho_w m_0}{m_0 - m}$$

where ρ_w is the density of water at measuring temperature, m_0 is the mass of sample in air, and m is the mass of the sample in water.

3.2.2. X-ray diffraction analysis

Room temperature X-ray diffraction

X-ray diffraction (XRD) technique is a powerful tool for material characterization as well as for detailed structural elucidation. Crystallographic and phase analyses were performed by an X-ray diffractometer (XRD RAD III, Rigaku, Japan) by using monochromatic CuK_α radiation with the wavelength $\lambda = 1.54178 \text{ \AA}$. The detection range was $20^\circ - 80^\circ$ with a step size of 0.02° and a speed of $2^\circ/\text{min}$. From the value of $2\theta_{hkl}$ detected from the (hkl) peaks in XRD pattern, the inter planar spacing d_{hkl} was calculated by using Bragg's law:

$$\lambda = 2d_{hkl} \sin \theta_{hkl}$$

After then, the lattice parameters were estimated for several crystal structures using following relationships:

+ For cubic or pseudocubic:

$$\frac{1}{d_{hkl}^2} = \frac{h^2 + k^2 + l^2}{a^2}$$

+ For tetragonal:

$$\frac{1}{d_{hkl}^2} = \frac{h^2 + k^2}{a^2} + \frac{l^2}{c^2}$$

+ For orthorhombic:

$$\frac{1}{d_{hkl}^2} = \frac{h^2}{a^2} + \frac{k^2}{b^2} + \frac{l^2}{c^2}$$

+ For rhombohedral:

$$\frac{1}{d_{hkl}^2} = \frac{(h^2 + k^2 + l^2)\sin^2\alpha + 2(hk + kl + hl)\cos^2\alpha - \cos\alpha}{a^2(1 - 3\cos^2\alpha + 2\cos^3\alpha)}$$



Figure 3.2. (a) Multi Purpose X-Ray Diffractometer and (b) JEOL Field Emission Scanning Electron Microscope.

High temperature X-ray diffraction

The high temperature XRD measurements were carried out with an Ultima IV X-ray diffractometer (Multi Purpose XRD, H-2, Rigaku, Japan), which was pictured in Figure

3.2 (a). The measurements were performed in a temperature chamber with the studied pellet mounted onto a heating trip with a step size of 0.02° at speed of $1^\circ/\text{min}$ in the range of $30^\circ\text{--}50^\circ$. Samples were heated up to a given temperature with $10^\circ\text{C}/\text{min}$ and kept there for 20 minutes before the start of the XRD run.

3.2.3. Surface morphology and microstructure analysis

The microstructure of samples were studied by Field Emission Scanning Electron Microscope (FE-SEM, JEOL, JSM-650FF, Japan), pictured in Figure 3.2 (b). For sample preparation, the sintered specimens were polished with sandpapers (600Cw, 1000Cw, 1500Cw and 2000Cw) to obtain 1mm thickness and smooth surface, then fine polished with alumina polishing powders by an electric polishing machine (Dong ILT, 802-0408) to get the mirror surface. The polished specimens were washed with ethanol in ultrasonic machine (Branson 3210) for 30min, dried and thermally etched at the etching temperature (100°C lower than sintering temperature) for 1h.

3.2.4. Piezoresponse force microscopy analysis, PFM

Piezoresponse force microscopy (PFM) has been established as a reliable approach to study the dynamic behavior, piezoelectric properties, switching mechanism, and configuration of the ferroelectric domains in the piezoelectric materials. For PFM observations, the sintered samples were polished to $20\mu\text{m}$ thickness using polycrystalline diamond paste with abrasive particles of 3.5, 1.0, and $0.25\mu\text{m}$ (DP-Paste P by Struers A/S, Ballerup, Denmark) for 1h each. The PFM experiments were carried out using a commercial atomic force microscopy (MFP-3D, Asylum Research, Goleta, CA). The PFM signal was recorded at room temperature under an AC voltage of 5V at frequency of 280kHz, applied to a conductive Pt-Ir-coated cantilever PPP-NCHPt (Nanosensors, Neuchatel, Switzerland).

3.2.5. Dielectric and piezoelectric properties analysis

For dielectric and electrical properties measurements, the sintered specimens were carried out to obtain 1mm thickness using 800Cw and 1500Cw sandpapers. The lapped specimens were then with ethanol in ultrasonic machine (Branson 3210) for 30min. The silver paste (Ag, Sung Jee Tech, Co.) was screen printed on whole area of the opposite faces of the dried specimens. The deposited electrodes were then fired at 700°C for 30min. The baked ceramics are composed of randomly oriented grains, which possess identical structure but have a random orientation, resulting in a small or zero net spontaneous polarization. The side of those samples were polished to prevent to electrical leakage between two electrodes. To measure the properties at poled states, the ceramic specimens were poled at 100°C in a silicon oil bath by applying an electric field of 4 kV/mm for 30min using a high voltage power supply (Conver Tech, SHV30) and field cooling down to room temperature.

Dielectric properties analysis

The room temperature capacitance C_P and the dissipation factor (D or $\tan\delta$) were measured using the impedance grain phase analyzer (Hewlett Packard 4194A) with a working frequency range from 0.1 Hz to 40 MHz. The relative dielectric permittivity ϵ_r can be calculated using following relation:

$$\epsilon_r = \frac{C_P \cdot d}{A \cdot \epsilon_0}$$

where $\epsilon_0 = 8.854 \times 10^{-12}$ F/m is the permittivity of vacuum, d is the thickness and A is the area of the specimen.

The temperature-dependent dielectric properties of both poled and unpoled specimens were determined using an impedance analyzer (HP4192A, USA) attached to a computer

programmable electric furnace at different frequencies (0.1–10MHz) in temperature range 30°C–450°C under a heating rate of 3°C/min. Each specimen was measured three times for unpoled, poled and depoled states.

Polarization and strain analysis

The electromechanical strain S – E and polarization P – E hysteresis loops were measured by using a commercial aixPES setup (aixACCT Systems GmbH, Germany) at frequency of 1Hz. The full-set form of device is performed in Figure 3.3. Whole system was stayed in a room with certain temperature and humidity. Before measuring, all samples were thermal annealed at 450°C to remove the remnant polarization.



Figure 3.3. AixPES (aixACCT) setup for measuring P–E and S–E hysteresis loop.

Piezoelectric properties analysis

The piezoelectric coefficient d_{33} of specimens was measured using the applied stress and measured polarization by PIEZO d_{33}/d_{31} METER (IACAS, Model ZJ-6B). The resonance (f_r) and anti-resonance (f_a) frequencies, minimum impedance at resonance frequency Z_m , and represents the low frequency capacitance C_0 of specimens were measured using the impedance gain phase analyzer (Hewlett Packard 4194A) with a working frequency range from 0.1 Hz – 40 MHz. From them, the planar coupling coefficient k_p and the mechanical quality factor Q_m was calculated using following equations:

$$k_p = \frac{f_a^2 - f_r^2}{f_r^2}$$

$$Q_m = \frac{1}{2\pi f_a Z_m C_0} \frac{f_a^2}{f_a^2 - f_r^2}$$

Chapter 4: New phase boundary in lead-free piezoelectric KNN-based composites originating from coexistence of ferroelectrics and relaxor

4.1. Investigation of high temperature phase transition behaviors and piezoelectric properties for BaZrO₃-modified lead-free KNN-BLT ceramics

The formation of morphotropic phase boundary (MPB) in piezoelectric ceramics is one of the most important concepts to enhance the dielectric and piezoelectric properties. In this work, rhombohedral (R) and tetragonal (T) phase boundary has been designed and clarified using the lead-free $0.92(\text{Na}_{0.5}\text{K}_{0.5})\text{NbO}_3-(0.08-x)(\text{Bi}_{0.5}\text{Li}_{0.5})\text{TiO}_3-x\text{BaZrO}_3$ ternary system. The R-T phase coexistence region is identified in the ceramics with $0.06 \leq x \leq 0.07$. We successfully demonstrated that a relatively enhanced d_{33} and its excellent temperature stability are originated from phase transition behaviors that were confirmed by temperature-dependent dielectric properties and temperature-dependent X-ray diffraction (XRD) patterns. The ceramic fabrication was mentioned in detail in chapter 3.

This work has been published on Journal of Electroceramics (04/2021).

4.1.1. Motivation and scope

Lead-based piezoelectric materials have been used in various applications for sensors and actuators [25,87]. However, lead contained high toxicity, made harmful effects on the environment and human. Therefore, waste electric equipment (WEEE), restrictions on hazardous substances (RoHS), and end-of-life vehicles (ELV) were established to prevent pollutants. Recently, lead-free materials were strongly developed to replace lead-based piezoelectric materials [88-92].

$K_{0.5}Na_{0.5}NbO_3$ and its compounds have been considered as one of promising candidates because of their excellent dielectric and piezoelectric properties [93-96]. Pure KNN is a well-known lead-free piezoelectric ceramic because of its high Curie temperature T_C around 420 °C and large electromechanical coupling factors with the orthorhombic-tetragonal phase transition temperature T_{O-T} around 200°C [12]. There were many studies to improve the properties for KNN-based materials by addition, substitution, modification some elements in pure KNN [9,92,97-102] defined the concept of polymorphic phase transition (PPT) at room temperature. The PPT compositions have improved properties at room temperature, in comparison with pure KNN. Thong *et al.* systematically provided a historical evolution of KNN-based materials with the improvement of piezoelectric properties based on phase boundaries [11]. However PPT concept has the temperature sensitive problem [12,96], the phase boundary corresponding to R-O or O-T possesses the PPT characteristic depending on not only the compositions but also the temperatures [58,103]. To overcome this problem, several possible solutions have been considered. One is a producing highly textured ceramics [104,105], but it requires complex synthesis process with high cost. Another way is an inducing a single tetragonal phase by shifting the T_{O-T} to below room temperature with chemical modifications, which is accompanied by degradation of the piezoelectric properties [96,106]. One more useful concept, namely the morphotropic phase boundary (MPB) is able to expect enhancement of both thermal stability and piezoelectric properties.

The MPB is the nearly vertical phase boundary separating rhombohedral, tetragonal, and/or monoclinic ferroelectric phases and nearly temperature independent. MPB plays a very important role in PZT ceramics because of the excellent piezoelectric and dielectric properties. Some examples of MPB in PZT is considered in the field of piezoelectric materials [13,107-109]: the crystal structure changes abruptly and the piezoelectricity is maximized for compositions at MPBs, which is frequently reported as a region of phase

coexistence. Materials in this region exhibit a very high piezoelectric response, and it has been conjectured that these two features are intrinsically related. $\text{Pb}(\text{Zr}_{0.52}\text{Ti}_{0.48})\text{O}_3$ has shown high performance actuators and transducers, since its superior dielectric, piezoelectric, and electromechanical coupling coefficients, as a result of enhanced polarizability arising from the domain wall mobility [110] at MPB. Besides, it was reported that the coupling between tetragonal and rhombohedral phases further allows an optimal domain reorientation during the poling process [13,25,107-109,111].

Recently, there were some studies to construct MPB in lead-free piezoelectric ceramics [58-62], especially, in KNN-based materials. Liu *et al.* [14] introduced a way of forming MPB by shifting diffused R-O and O-T phase transition closer to create a partially overlapped phase transition over a broad temperature range. Another approximation to form an MPB was using two end members, one with tetragonal symmetry and the other with rhombohedral symmetry at room temperature [25]. Wang *et al.* reported the phase diagrams of the $(1-x)\text{Na}_{0.5}\text{K}_{0.5}\text{NbO}_3-x\text{MTiO}_3$ (with $M = \text{Pb}, \text{Ba}, \text{Sr}, \text{Ca},$ and $\text{Bi}_{0.5}\text{Li}_{0.5}$) solid solutions, showed that $(1-x)\text{Na}_{0.5}\text{K}_{0.5}\text{NbO}_3-x\text{Bi}_{0.5}\text{Li}_{0.5}\text{TiO}_3$ has a tetragonal phase for $0.06 \leq x \leq 0.15$ at room temperature [42]. Wang *et al.* also study the effects of A-site ions on the successive phase transition temperatures of $(1-x)\text{Na}_{0.5}\text{K}_{0.5}\text{NbO}_3-x\text{AZrO}_3$ ($A = \text{Sr}, \text{Ca}$) solid solutions, and found that with increasing x , the tetragonal-orthorhombic phase transition temperature $T_{\text{T-O}}$ shift to the lower-temperature region, while the orthorhombic-rhombohedral phase transition temperature $T_{\text{O-R}}$ shifts to the higher temperature region, then, stabilized a rhombohedral phase for $0.08 \leq x \leq 0.15$ at room temperature [48].

By co-incorporating BaZrO_3 and $(\text{Bi}_{0.5}\text{Li}_{0.5})\text{TiO}_3$ into $(\text{Na}_{0.5}\text{K}_{0.5})\text{-NbO}_3$, Zushi *et al.* [112] found that the formation of an MPB was possible for $0.92(\text{Na}_{0.5}\text{K}_{0.5})\text{NbO}_3-(0.08-x)(\text{Bi}_{0.5}\text{Li}_{0.5})\text{TiO}_3-x\text{BaZrO}_3$ ceramics between $x = 0.07$ and 0.08 , using Raman scattering spectra and Rietveld analyses. Wang *et al.* [113], focus on $x = 0.05$ and 0.06 for

composition $0.92(\text{Na}_{0.5}\text{K}_{0.5})\text{NbO}_3-(0.08-x)(\text{Bi}_{0.5}\text{Li}_{0.5})\text{TiO}_3-x\text{BaZrO}_3$, mainly investigate for temperature dependent permittivity and the stability of d_{33} at high temperature. However, there was no study investigated the crystal structure of these composition at high temperature to prove the existence and maintaining the phase coexistence. Therefore, this study focused on temperature dependent dielectric properties and the X-ray diffraction patterns and the temperature stability of piezoelectric constant d_{33} to emphasize the phase diagram, so on, impress the existence of morphotropic phase boundary.

4.1.2. Results and discussions

Polished and thermally etched surface images of KNN-BLT-100xBZ ceramics are displayed in Figure 4.1. The obtained density values for sintered KNN-BLT-100xBZ ceramics were around 4.4g/cm^3 which are corresponding to around 95% as the relative density. The calculated average grain sizes for KNN-BLT-100xBZ ceramics slightly increased from $1.27 \pm 0.04 \mu\text{m}$ for KNN-BLT-4BZ ceramics to $1.43 \pm 0.08 \mu\text{m}$ for KNN-BLT-6BZ ceramics, which then decreased to $1.28 \pm 0.03 \mu\text{m}$ for KNN-BLT-8BZ ceramics. However, the surface images for KNN-BLT-4BZ and KNN-BLT-5BZ seem to be not treated with polishing, even all samples were simultaneously prepared (polishing and thermal etching) with same method. In fact, it was reported that similar behaviors were observed in other studies on KNN-based materials [114-116]. These phenomena may be originated from the effect of etching process [114], or naturally induced porosities in specimen [115].

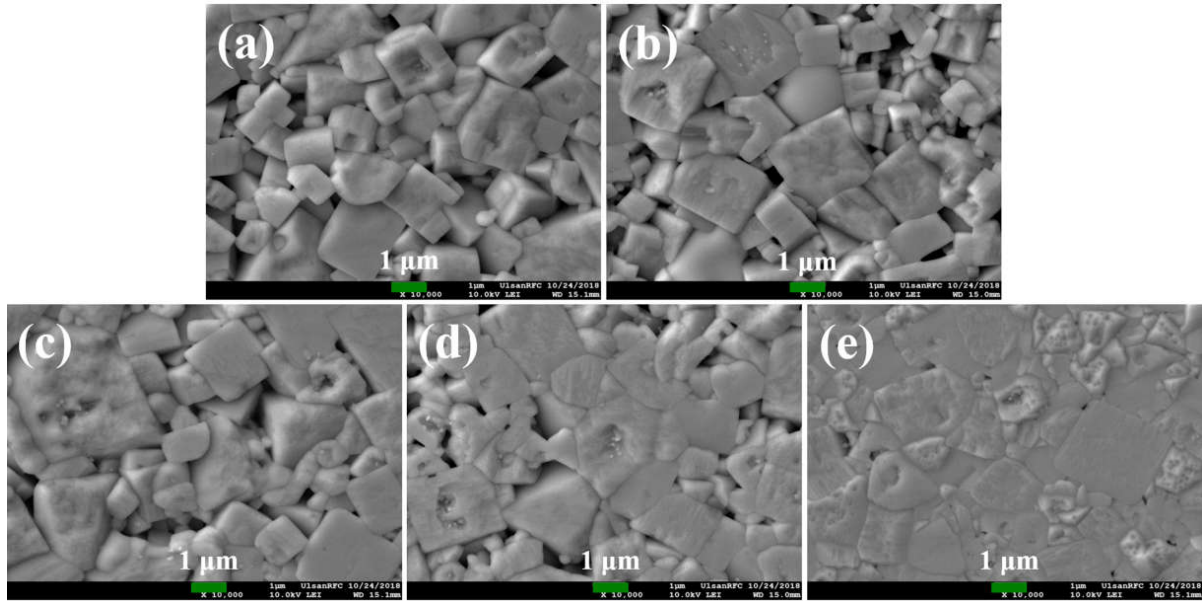


Figure 4.1. Polished and thermally etched surface images of KNN–BLT–100xBZ ceramics, (a) $x = 0.04$, (b) $x = 0.05$, (c) $x = 0.06$, (d) $x = 0.07$, and (e) $x = 0.08$.

Figure 4.2 depicts X-ray diffraction patterns for KNN–BLT–100xBZ ceramics as a function of BZ content. A single perovskite structure without any secondary phases was obtained in all samples. This indicates that KNN–BLT–100xBZ ceramics as a solid solution were stably synthesized. To clarify the phase transition behaviors of KNN–BLT–100xBZ ceramics, around 45° peaks for all compositions were deconvoluted using pseudo–Voigt peak shape function that are displayed in Figure 4.2(c). In the case of KNN–BLT–4BZ ceramics, two distinct peaks as (002) and (200) were observed that corresponded to tetragonal structure. On the other hand, KNN–BLT–8BZ ceramics was refined as rhombohedral structure with single (200) peak at 45° . In fact, the effects of BZ modification on the stabilization of rhombohedral phase in KNN–based ceramics that was firstly reported by Wang *et al.* [47] in 2009. Moreover, two peaks for tetragonal phase and one peak for rhombohedral phase were observed from the deconvoluted XRD analysis for KNN–BLT–6BZ ceramics in Fig. 2(c). Accordingly, it is suggested that a coexistence of

tetragonal and rhombohedral phases was formed in KNN–BLT–6BZ ceramics.

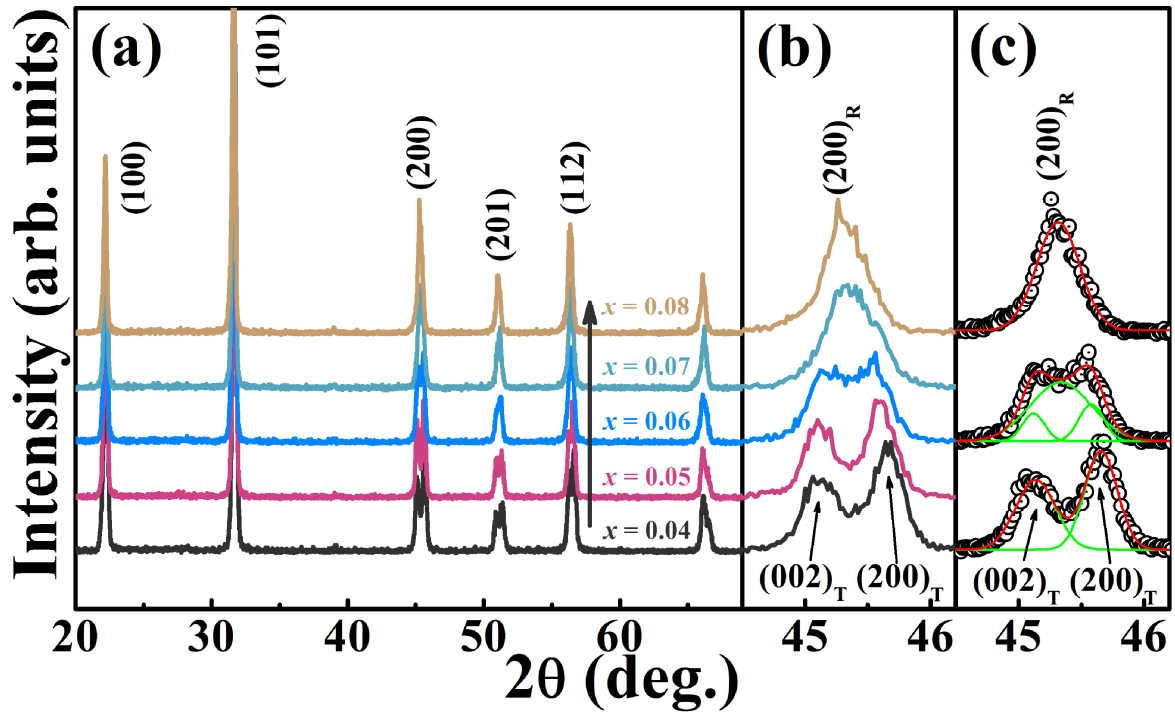


Figure 4.2. X-ray diffraction patterns of KNN–BLT–100xBZ ceramics in the 2θ ranges of (a) 20° – 70° , (b) 44.5° – 46.2° and (c) deconvoluted peaks.

Figure 4.3 presents polarization (P – E) and bipolar strain (S – E) curves for KNN–BLT–100xBZ ceramics. The square-shaped P – E and butterfly-shaped S – E curves as normal ferroelectric features were observed at all samples. Maximum polarization (P_{\max}), remanent polarization (P_r), coercive field (E_c), maximum strain (S_{\max}), and negative strain (S_{neg}) values under the applied electric field of 4 kV/mm were extracted from Figure 4.3 that are described in Figure 4.4. The highest values for P_{\max} and P_r were obtained in KNN–BLT–5BZceramics. E_c values for KNN–BLT–100xBZ ceramics were monotonically decreased with increasing BZ content. It can be assumed that the stabilized rhombohedral phases in KNN–BLT–100xBZ ceramics by added BZ are responsible for these polarization changes. In fact, it is known that E_c for tetragonal phase are relatively

stronger than rhombohedral phase due to the existence of 90° domains [117,118]. The strain value was firstly increased then decreased with increasing BZ content. We could obtain the highest strain value in KNN–BLT–6BZ ceramics. In fact, these changes of strain properties can be found in many other studies on ferroelectric and relaxor materials. The enhancement of strain properties at MPB region with rhombohedral–tetragonal [119,120] may be based on the relatively attribution and the interaction between interface of rhombohedral and tetragonal [121,122]. More recently, some studies also investigated on strain behavior for ferroelectric–relaxor boundary and figured out the similar trend, which originated from the contribution of polar–nano regions [123,124].

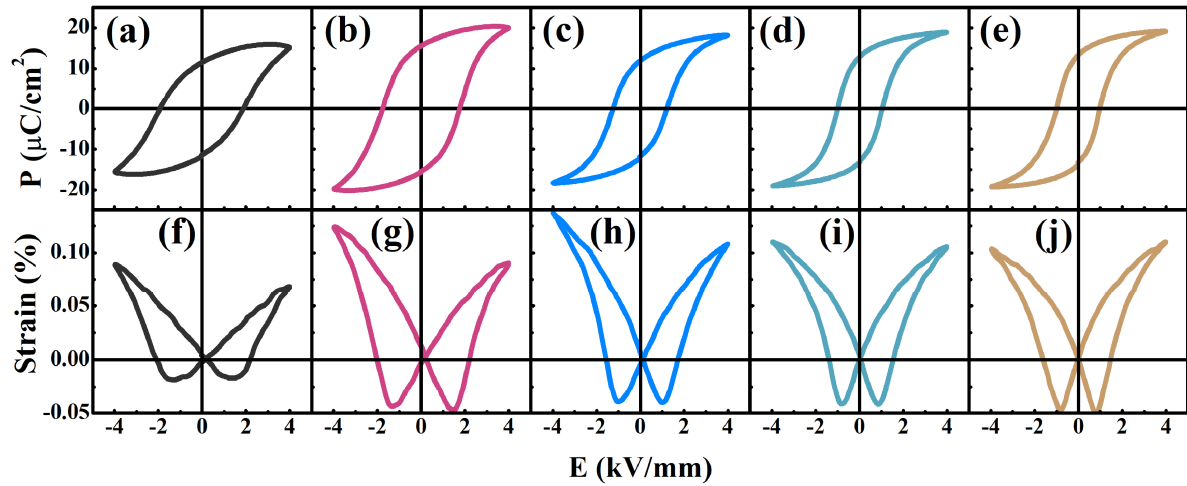


Figure 4.3. Polarization (top) and bipolar strain curves (bottom) of KNN–BLT–100xBZ ceramics as a function of BZ content.

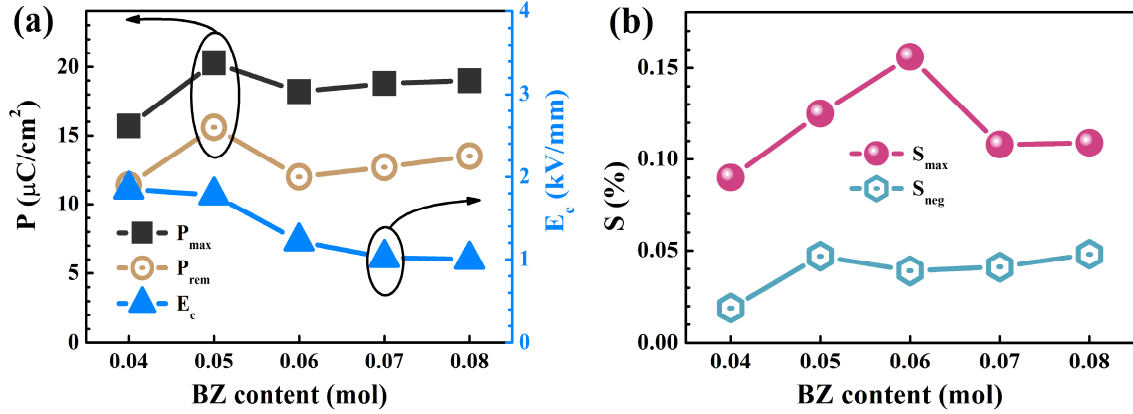


Figure 4.4. Changes of (a) P_{\max} , P_r , E_c values and (b) S_{\max} , S_{neg} values of KNN-BLT-100xBZ ceramics as a function of BZ content.

The dielectric constant (ϵ_r) and dielectric loss ($\tan\delta$) for KNN-BLT-100xBZ ceramics as a function of temperature is shown in Figure 4.5(a) and (b), respectively. The ϵ_r values at room temperature for KNN-BLT-100xBZ ceramics were increased, then decreased by BZ adding, which were culminated in the highest ϵ_r value in KNN-BLT-6BZ ceramics. On the other hand, the minimum value of $\tan\delta$ was obtained in KNN-BLT-6BZ ceramics. The ϵ_r and $\tan\delta$ of KNN-BLT-6BZ ceramics is represented in Figure 4.5(c) that was measured at different frequencies as a function of temperature. The detected cubic-tetragonal phase transition temperature (T_C) and tetragonal-rhombohedral phase transition temperatures (T_{R-T}) are provided in Figure 4.5(d). T_C for all samples was monotonically decreased from 305°C for KNN-BLT-4BZ ceramics to 255°C for KNN-BLT-8BZ ceramics. There are no abnormal peaks on ϵ_r or $\tan\delta$ for KNN-BLT-4BZ and KNN-BLT-5BZ ceramics in between room temperature (RT) and T_C . This implies that those samples were stabilized as a tetragonal phase. On the other hand, a weak discontinuous peak was detected in KNN-BLT-6BZ ceramics. Besides, apparent peaks were observed at around 100°C for KNN-BLT-7BZ ceramics and 150°C for KNN-BLT-8BZ ceramics that may be originated from the existence of rhombohedral

phase. As we discussed in Figure 4.2, it can be assumed that rhombohedral phases in KNN–BLT–100xBZ ceramics were stabilized by BZ adding. Indeed, it is well–know that BZ strongly affects the stabilization of rhombohedral phase in KNN–based ceramics [47].

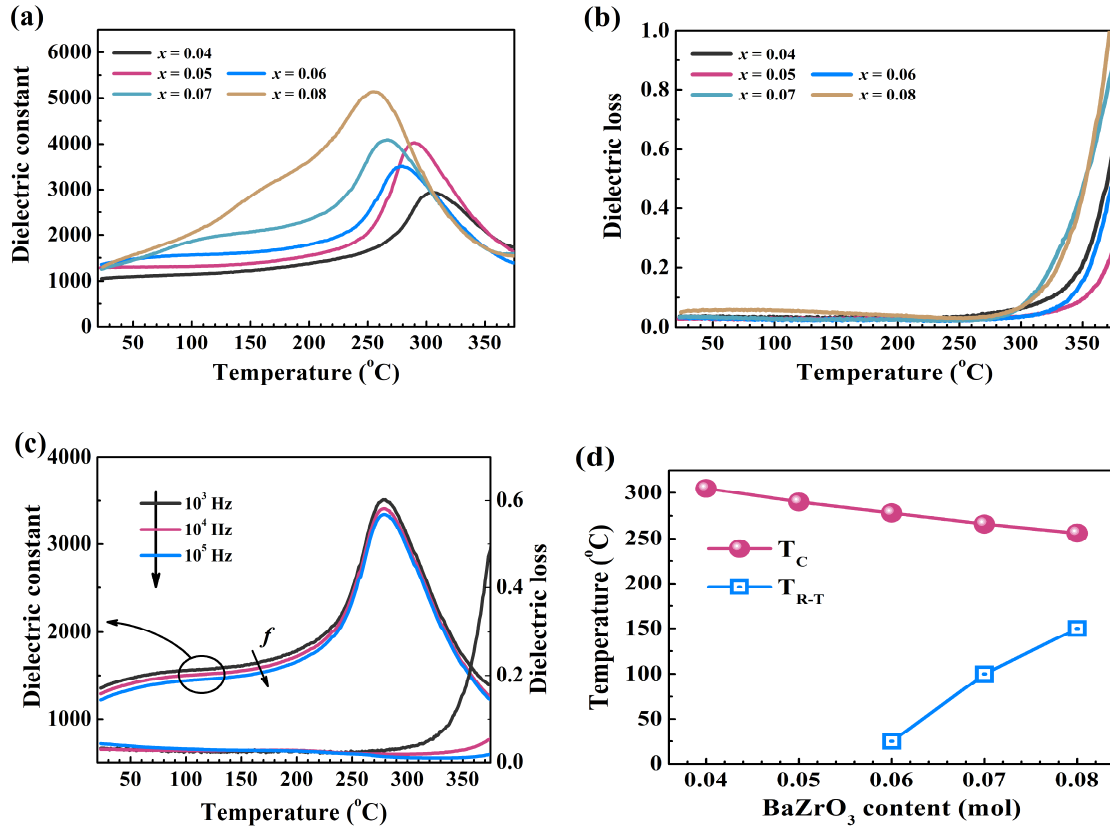


Figure 4.5. (a) Temperature–dependent dielectric constant and (b) dielectric loss of KNN–BLT–100xBZ ceramics, (c) temperature–dependent dielectric constant for KNN–BLT–6BZ ceramics at different frequencies, and (d) changes of phase transition temperatures as a function of BZ content.

Figure 4.6(a) provides the changes of piezoelectric constant (d_{33}) and electromechanical coupling factor (k_p) values for KNN–BLT–100xBZ ceramics as a function of BZ content. Furthermore, the relationship between changes in temperature–dependent dielectric constant and d_{33} for KNN–BLT–5BZ, KNN–BLT–6BZ,

and KNN–BLT–8BZ ceramics are contrasted in Figure 4.6(b), (c), and (d), respectively. The highest d_{33} of 240 pC/N was obtained in KNN–BLT–6BZ ceramics due to the coexistence of tetragonal and rhombohedral phases, where k_p reached the highest value of around 34%. The samples were annealed for 5 min at different temperature steps, with the increasing step increment of 25°C, from room temperature to 350°C, to check the temperature stability of the piezoelectric constant d_{33} . The measuring temperature for d_{33} in Figs. 6 (b), (c), and (d) was the annealing temperature.

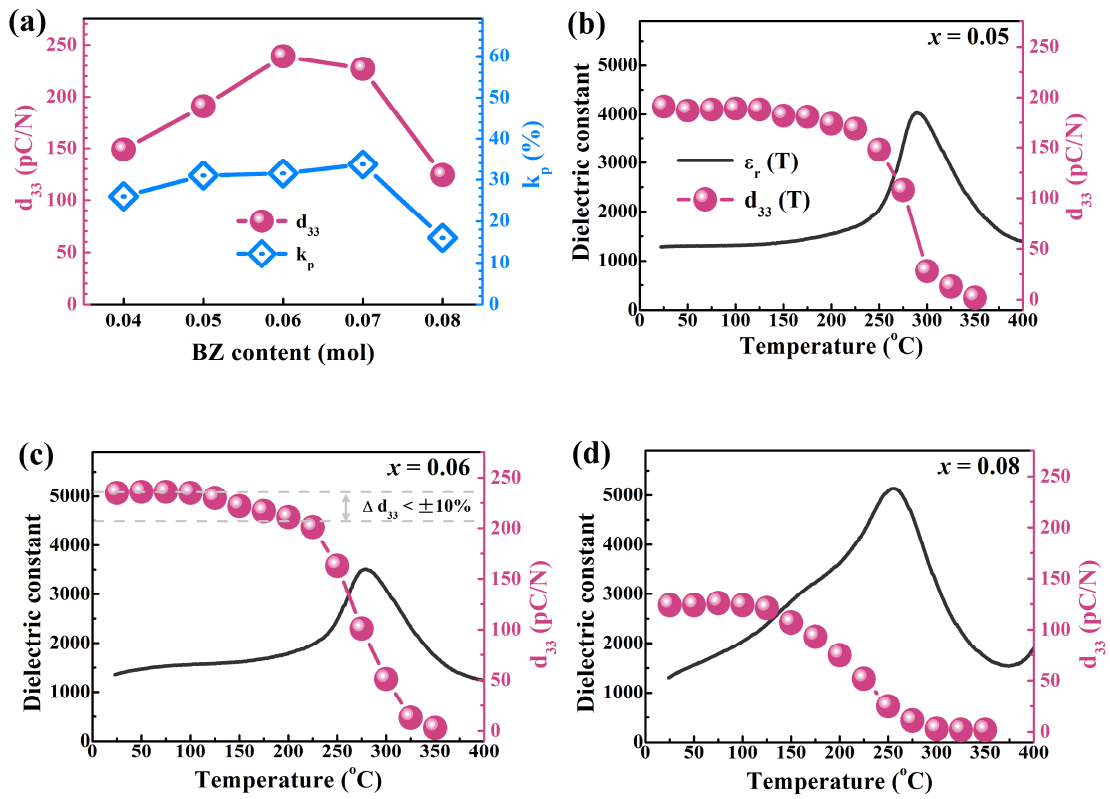


Figure 4.6. Changes of (a) d_{33} and k_p for KNN–BLT–100xBZ ceramics as a function of BZ content, temperature–dependent dielectric constant and d_{33} for (b) KNN–BLT–5BZ, (c) KNN–BLT–6BZ, and (d) KNN–BLT–8BZ ceramics.

In the case of KNN–BLT–5BZ ceramics, the nearly constant d_{33} values in temperature range of 25°C ~ 225°C might be based on the detected single tetragonal phase. In fact, similar phenomena were reported in some studies [57,96,106]. In addition, in KNN–BLT–6BZ ceramics, we could obtain the highest d_{33} with comparatively good temperature stability (Δd_{33} less than $\pm 10\%$). It can be suggested that these behaviors are related to coexistence of tetragonal and rhombohedral phases in the temperature range of 25°C – 250°C. On the other hand, d_{33} for KNN–BLT–8BZ ceramics revealed relatively sensitive temperature dependence. The reason for this might be that KNN–BLT–8BZ ceramics additionally undergoes a phase transition (rhombohedral to tetragonal phase) at 150°C as shown in Figure 4.6(d) and discussed in Figure 4.5. Initially, d_{33} was 125 pC/N from 25°C to 150°C, then it descends gradually.

To clarify the relationship between the crystal structures and temperature–dependent d_{33} behaviors, temperature–dependent XRD patterns for KNN–BLT–100xBZ ceramics are exhibited in Figure 4.7. There are notable differences can be found in these three materials, based on their crystal structure at room temperature. In the case of KNN–BLT–5BZ ceramics in Figure 4.7(a) and (d), two distinct peaks with a couple of $K\alpha_2$ peaks corresponding to tetragonal phase were detected from 25°C to 250°C. This result is well–matched with the changes of temperature dependent ϵ_r in Figure 4.5 and d_{33} in Figure 4.6(b). Those peaks were merged as cubic structure at temperature above 275°C, eventually. Therefore, we could obtain excellent temperature stability for d_{33} value for KNN–BLT–5BZ ceramics.

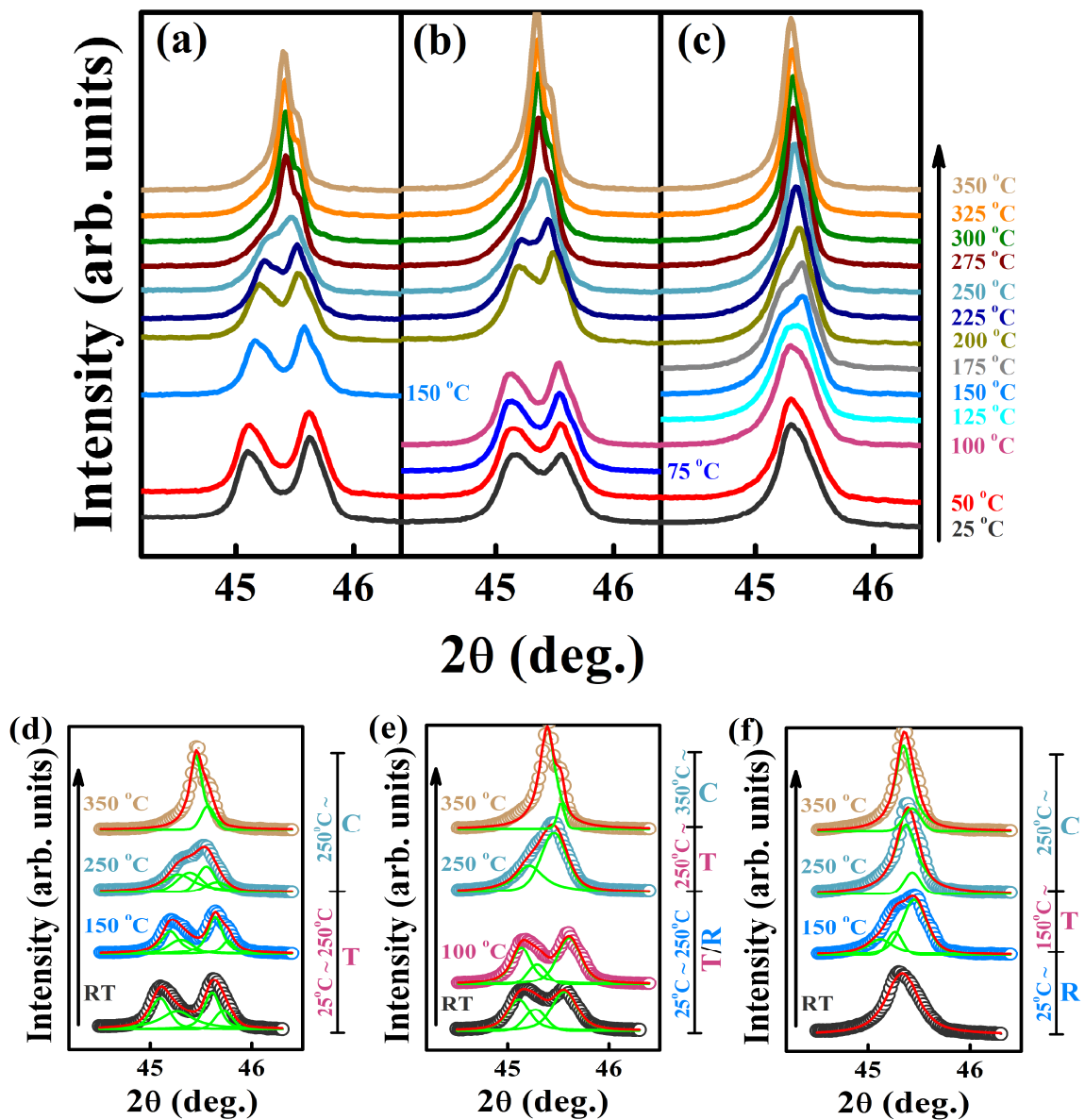


Figure 4.7. Temperature-dependence of X-ray diffraction patterns in the 2θ ranges of 44.5° – 46.2° for (a) KNN–BLT–5BZ, (b) KNN–BLT–6BZ, and (c) KNN–BLT–8BZ ceramics as a function of temperature and the deconvoluted results for (d) KNN–BLT–5BZ ceramics, (e) KNN–BLT–6BZ, and (f) KNN–BLT–8BZ ceramics at representative temperatures.

In case of KNN–BLT–6BZ, Figure 4.7(b) briefly describes two different regions of crystal structure: (i) the coexistence of a tetragonal–rhombohedral phase at temperatures up to 225°C and (ii) a cubic phase at temperatures higher than 275°C . According to the

deconvoluted curves for KNN–BLT–6BZ in Figure 4.7(e), this identification can be more surely consider with the simultaneously contributing of tetragonal and rhombohedral structure at room temperature and 100°C, and the cubic structure at 350°C with a corresponding $K\alpha_2$ peak. Besides, it is suggested that the crystal structure at 250°C could be a coexistence of tetragonal and cubic (or rhombohedral) phases. It is noted that the sequences of these phase transitions are responsible for a relatively enhanced d_{33} value with good temperature stability of KNN–BLT–6BZ ceramics. In Figure 4.7(c) and (f), a single peak of rhombohedral phase was detected in KNN–BLT–8BZ ceramics, which remained until 125°C. We found that the peak for rhombohedral phase was split into a couple of peaks as tetragonal phase at 150°C. In fact, the relatively sensitive temperature dependent d_{33} for KNN–BLT–8BZ ceramics in Figure 4.6(d) is originated from this phase transition behavior. Moreover, a single cubic phase was observed over 250°C.

4.1.3. Conclusion

KNN–BLT–100xBZ ceramics solid solutions have been prepared by the solid–state reaction method. It was found that the coexistence of tetragonal and rhombohedral phase was detected at KNN–BLT–6BZ ceramics. It is noted that coexistence of tetragonal and rhombohedral phase resulted in d_{33} enhancing. Besides, we successfully demonstrated that a relatively enhanced d_{33} and its excellent temperature stability are originated from phase transition behaviors that were confirmed by temperature–dependent dielectric properties and –XRD patterns.

4.2. Effects of SrTiO₃ modification on piezoelectric and strain properties of lead-free K_{0.5}Na_{0.5}NbO₃-based ceramics

Lead-free (1-x)K_{0.5}Na_{0.5}NbO₃-xSrTiO₃ (KNN-100xST) piezoelectric ceramics were prepared using conventional solid-state reaction method to investigate their phase transition behavior and electrical properties. It is known that SrTiO₃ modification in lead-free KNN ceramics is able to improve piezoelectric properties as well as sinterability of KNN ceramics. The previous studies for SrTiO₃-modified KNN ceramics have mainly focused on the enhancement of dielectric and piezoelectric properties using orthorhombic-tetragonal phase transition concept. However, the electromechanical strain behavior near this phase boundary still remains a challenge. In this work, the polymorphic phase boundary between the orthorhombic and the tetragonal phases can be found at 5 mol% of SrTiO₃ content, where enhanced piezoelectric constant (d_{33}) was observed. Besides, the normalized strain (d_{33}^*) was obtained from the unipolar strain at 4 kV/mm, which reached 210 pm/V as the highest values in KNN-5ST ceramics. The ceramic fabrication was mentioned in detail in chapter 3, respectively.

4.2.1. Motivation and scope

Piezoelectric materials have been used in various electronic devices applications, based on their mutual conversion between mechanical energy and electrical energy. Lead-based piezoceramics, such as Pb(Zr,Ti)O₃ (PZT), Pb(Mg_{1/3}Nb_{2/3})O₃-PbTiO₃ (PMN-PT) has been widely used for sensors and actuators, due to their excellent properties [3,25,125]. However, these materials contain high toxicity of lead which has brought serious problems for environment and human being [4]. Recently, lead-free piezoelectric materials were strongly developed in order to replace lead-based materials [88,90-94].

Among lead-free materials, $K_{0.5}Na_{0.5}NbO_3$ (KNN) compounds have been considered as promising candidates for sensors application. High Curie temperature around 420°C , an orthorhombic-tetragonal (O-T) phase transition temperature T_{O-T} around 200°C and large electromechanical coupling factors can be found in pure KNN [87]. To improve the properties of KNN-based materials, several chemical elements then were added, doped or modified [12,58] causing the formation of polymorphic phase transition (PPT) or morphotropic phase boundary (MPB). The PPT compositions in KNN-based materials have improved properties, however, remain the temperature sensitive problem [12,96], since the phase boundary corresponding to rhombohedral-orthorhombic (R-O) or O-T possesses the PPT characteristic depending on not only the compositions but also the temperatures. Meanwhile, the MPB concept with the phase structures dependent on the compositions and independent on temperatures recently has played a very important role in PZT [107,109] and lead-free piezoelectric ceramics [59,61,62], especially in KNN-based materials [60,112].

One method to form a tetragonal-rhombohedral (T-R) MPB is using composites of two end components, one has a tetragonal phase and the other has a rhombohedral phase at room temperature. Some chemical modifications have been used to stabilize the tetragonal phase from the orthorhombic phase in pure KNN, such as BiScO_3 [41], MTiO_3 (with $M = \text{Pb, Ba, Sr, Ca, Bi}_{0.5}\text{Li}_{0.5}\dots$) [42,43], LiMeO_3 (with $\text{Me} = \text{Nb, Ta, Sb}\dots$) [44-46]... Among them, SrTiO_3 is a promising candidate since SrTiO_3 modification in lead-free KNN ceramics is able to improve piezoelectric properties as well as sinterability of KNN ceramics [52,75]. Guo *et al.* firstly reported that the crystal structure changed from orthorhombic to tetragonal in the $[(K_{0.5}Na_{0.5})_{1-x}Sr_x](Nb_{1-x}Ti_x)O_3$ ceramics at $x \approx 0.040$ and the value of piezoelectric constant d_{33} almost monotonically decreased with increasing modification content [75]. Wang *et al.* then observed the orthorhombic-tetragonal phase boundary with enhanced dielectric and piezoelectric

properties in SrTiO₃-modified KNN, fabricated using Spark-plasma-sintering method [52]. Recently, some studies investigated the relaxor behaviors in Na_{0.5}K_{0.5}NbO₃-SrTiO₃ materials, at high SrTiO₃ modification content (≥ 10 mol%) with the crystal structure had been fully tetragonal or pseudo-cubic [126-128]. However, none of them clarified for the electromechanical strain behaviors at PPT region. In this work, lead-free SrTiO₃-modified KNN piezoceramics had been prepared by conventional solid-state reaction method with low modification content (≤ 10 mol%). The piezoelectric and ferroelectric properties near orthorhombic-tetragonal polymorphic phase transition were investigated.

4.2.2. Results and discussions

The surface images of polished and thermally etched KNN-100xST ceramics are displayed in Figure 4.8 (a-e). Abnormal grain growth was strongly observed in compositions around $x = 0.03$. The average grain size firstly increases from 0.6 μm for pure KNN, reaches the maximum value of 1.7 μm for $x = 0.03$, then decreases with the increase of ST content as shown in Figure 4.8 (f). The similar trend was also observed in other studies [124,129,130], which considered the low concentration of modifications can be responsible for the grain growth [131], while excessive content may restrict the movement of grains across the grain boundary causing inhibited grain growth [132,133]. Moreover, the graph for relative density in Figure 4.8 (f) implies that ST modification in KNN ceramics is responsible for the improving of sinterability.

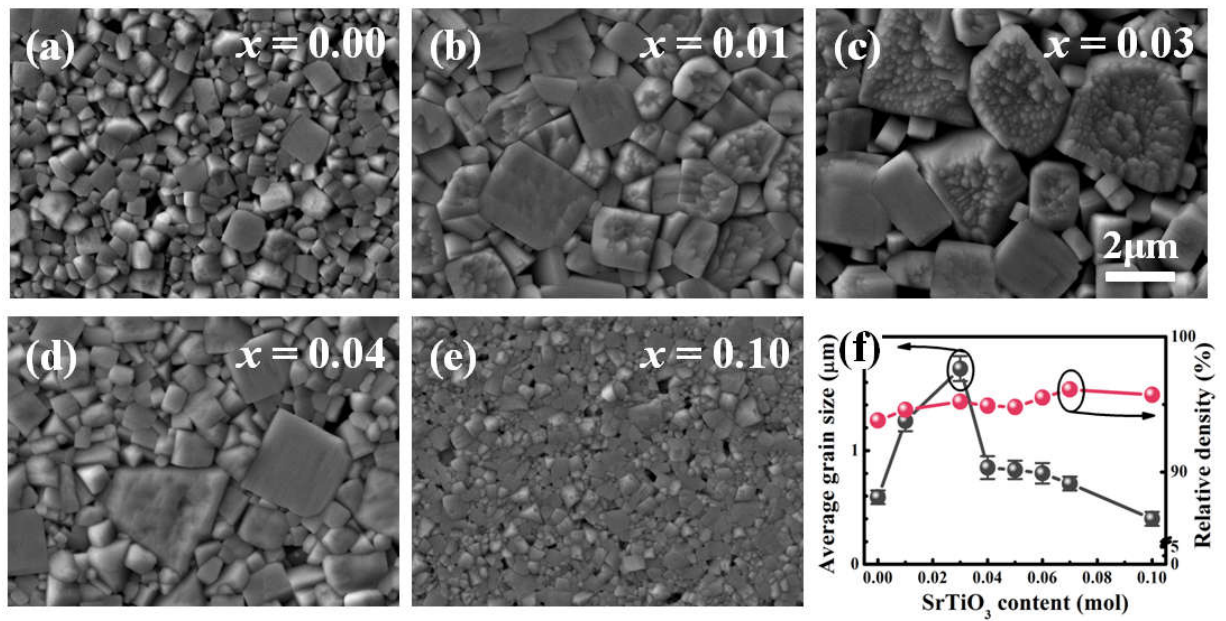


Figure 4.8. Polished and thermally etched surface images of lead-free KNN-100xST ceramics (a) $x = 0$, (b) $x = 0.01$, (c) $x = 0.03$, (d) $x = 0.04$, (e) $x = 0.10$. (f) Average grain size and relative density for KNN-100xST ceramics as a function of ST content.

Figure 4.9 (a) represents the X-ray diffraction patterns of the KNN-100xST ceramics at room temperature (RT). Single perovskite structure without significant secondary phases in all samples indicates the formation of a solid solution among the KNN and SrTiO₃. To clarify the changes of crystal structure for all compositions, (200) reflections with 2θ range of $44.4^\circ \sim 46.4^\circ$ are shown in Figure 4.9 (b). Two distinct peaks as (202) and (020) which were clearly observed in pure KNN and $x \leq 0.04$ compositions correspond to orthorhombic structures. When SrTiO₃ content $x \geq 0.06$, the intensity of peaks at (200) reflections are moderately reversed, corresponding to the (002) and (200) peaks of tetragonal symmetry. Moreover, it is considered that there is a coexistence of orthorhombic and tetragonal phases in $x = 0.05$ ceramic. The crystal structure and data for electrical properties of lead-free KNN-100xST ceramics are listed in Table 1. It is

expected that Sr^{2+} (with ionic radius of 1.44 Å) could substitute for Na^+ (1.39 Å) and K^+ (1.64 Å), while Ti^{4+} (0.61 Å) substituted for Nb^{5+} (0.64 Å). The lattice parameters and tetragonality were calculated from XRD data and shown in Figure 4.9 (c). It implies that for each phase of crystal structure the change of lattice parameters is not significant. Otherwise, the highest degree of tetragonality has been found at $x = 0.07$ compositions.

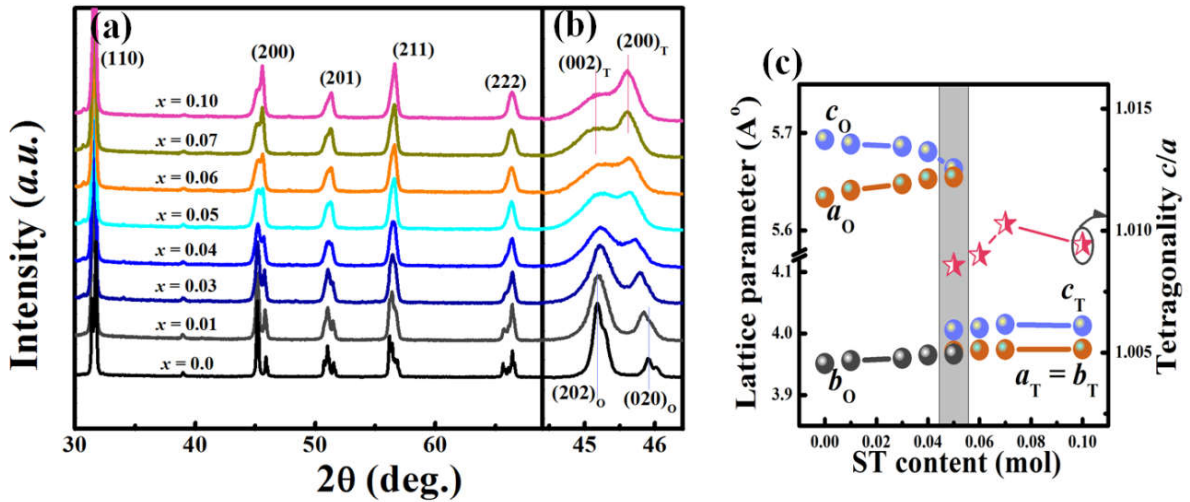


Figure 4.9. X-ray diffraction patterns of KNN–100xST ceramics as a function of ST content in the 2θ ranges of (a) 20° – 70° and (b) 44.4° – 46.4° . (c) Lattice parameters and tetragonality.

Table 5. Crystal structure and electrical properties of lead-free KNN–100xST ceramics

SrTiO ₃ content (x)	0	0.01	0.03	0.04	0.05	0.06	0.07	0.10
Crystal structure	O	O	O	O	O–T	T	T	T
ϵ_r	464	785	866	1069	1352	1426	1496	1490
P_r ($\mu\text{C}/\text{cm}^2$)	23.8	20.3	19	17.4	13.8	11.5	10	3.9
E_c (kV/mm)	1.09	1.57	1.52	1.50	1.42	1.57	1.56	1.05
T_c ($^\circ\text{C}$)	414	382	350	324	308	286	267	196
$T_{\text{O–T}}$ ($^\circ\text{C}$)	212	189	131	80	~RT			
d_{33} (pC/N)	90	95	99	108	130	125	78	65
d_{33}^* (pm/V)	90	100	175	185	210	175	130	95

The temperature dependent dielectric properties of KNN–100xST compositions are shown in Figure 4.10. In the range from RT to 450°C, pure KNN has two phase transition temperature namely the orthorhombic–tetragonal phase transition temperature (T_{O-T}) and Curie temperature (T_C) around 210°C and 410°C, detected by the corresponding peaks in the graphs of dielectric constant (ϵ_r) and dielectric loss ($\tan\delta$). With the increasing of SrTiO₃ content, both T_C and T_{O-T} are monotonically decreased and plotted in Figure 4.10 (d). There are no abnormal peaks between RT and T_C for $x \geq 0.06$ ceramics, which implies that T_{O-T} is lower than RT and those samples are stabilized as a tetragonal phase [134]. Otherwise, the peak at T_C becomes broader may be an evidence for relaxor–like behaviors in KNN–100xST ceramics [74].

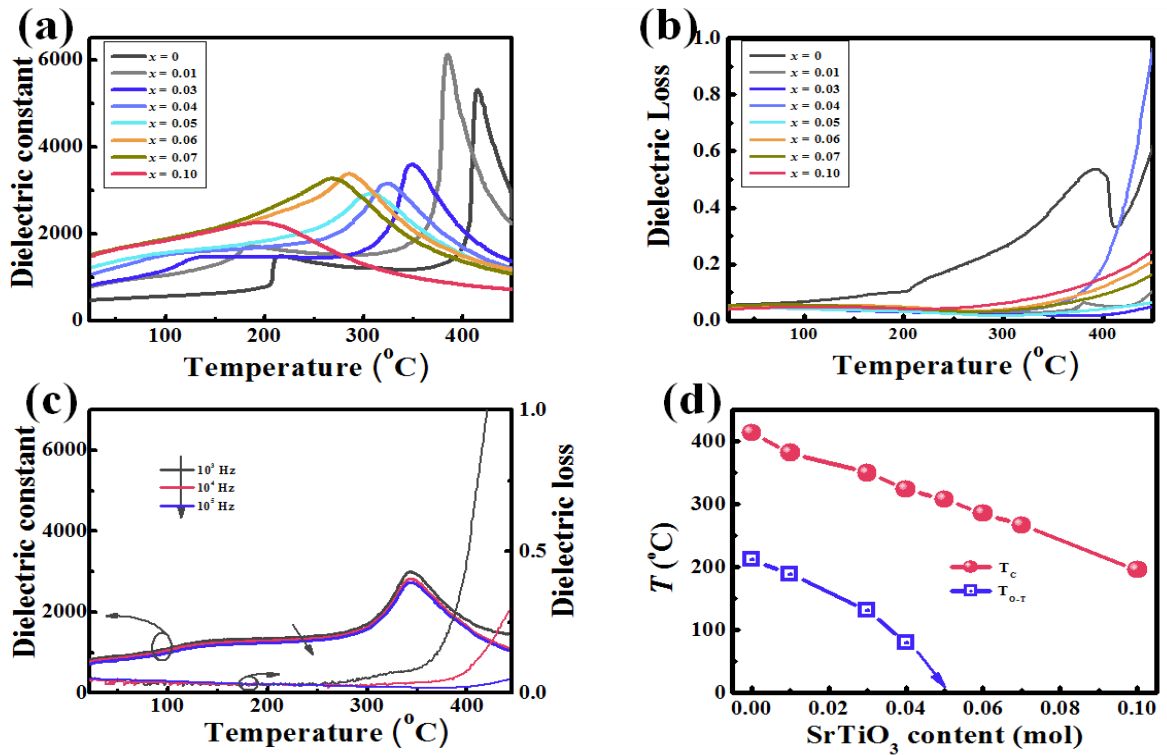


Figure 4.10. Temperature–dependent dielectric properties of KNN–100xST ceramics, (a) temperature–dependent dielectric constant (ϵ_r), (b) dielectric loss of KNN–100xST ceramics, (c) ϵ_r for KNN–3ST ceramics at different frequencies, and (d) the extracted phase transition temperatures as a function of ST content.

The polarization (P - E) and strain (S - E) virgin curves for KNN-100xST ceramics measured under an electric field of 4kV/mm, and the extracted parameters are shown in Figure 4.11. Pure KNN ceramics is well-known as a normal ferroelectric material with square-shaped P - E and butterfly-shaped S - E curves, as well as high remnant polarization (P_r) and remnant strain (S_{rem}). Those quantities are monotonically degraded with the increase of ST content. However, the total strain (S_{tot}) plot shows a local peak at $x = 0.04$ and 0.05 , resulting to the improvement for the usable strain (S_{usable}) at O-T phase transition region, following the equation:

$$S_{usable} = S_{tot} - S_{rem} \quad (1)$$

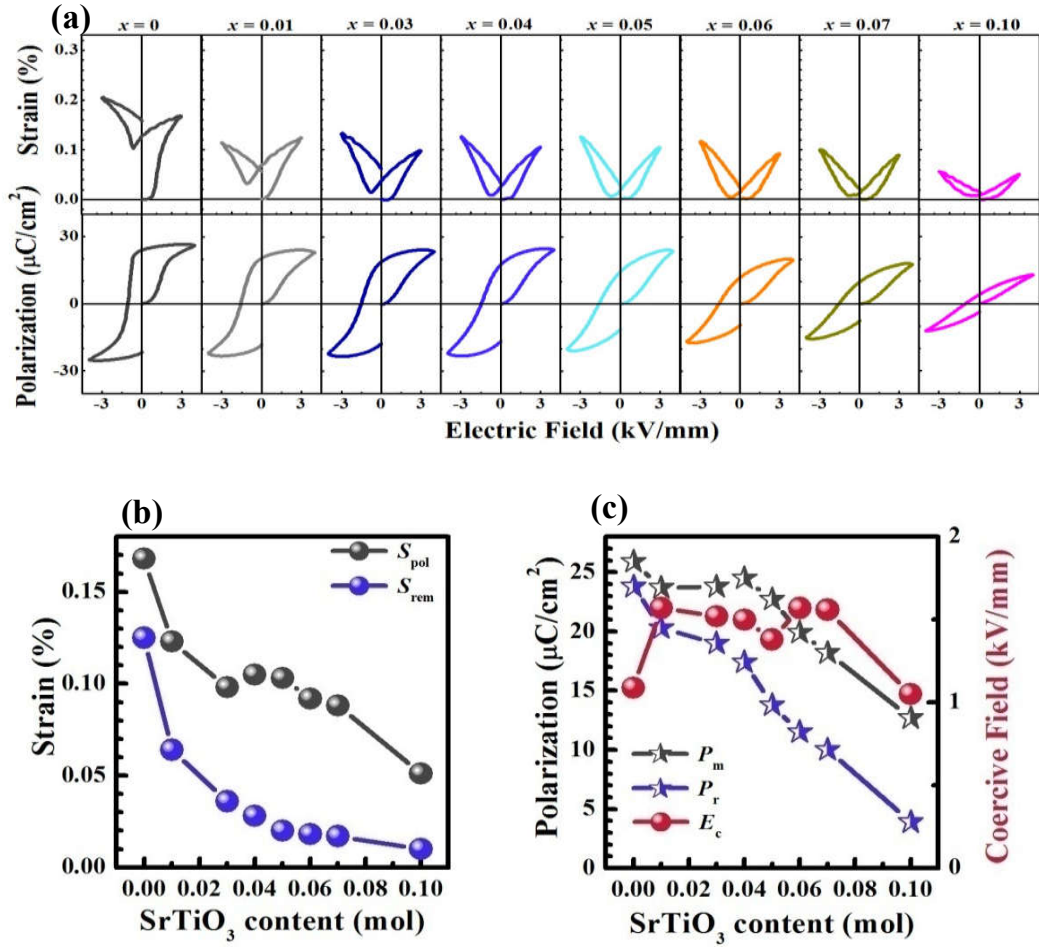


Figure 4.11. (a) Bipolar strain and polarization curves, (b) S_{pol} , S_{rem} values, (c) P_{max} , P_r and E_c values of KNN-100xST ceramics.

Figure 4.12 (a) performs the unipolar strain curves for KNN-100xST ceramics measured under an electric field of 4kV/mm. The maximum unipolar strain firstly increases, reaches highest value at $x = 0.05$ composition, then decreases. The normalized strain (d_{33}^*) is derived from unipolar strain values S_{uni} and shown in Figure 4.12 (b), in relationship with bipolar strain and polarization. The similar trend in the behaviors of normalized strain d_{33}^* , difference $S_{tot} - S_{rem}$, and $P_m^2 - P_r^2$, indicates the electrostrictive behavior in ferroelectric piezoelectric materials [135], following the equation:

$$S_{uni} \approx S_{usable} = S_{tot} - S_{rem} = Q(P_m^2 - P_r^2) \quad (2)$$

where Q is the electrostrictive constant of materials [136].

The strain enhancement near PPT region was mentioned in several publications [137-139] and suggested to be related with the domain mobility, based on the coexistence of orthorhombic and tetragonal phase. The relatively high maximum polarization (P_m) and low coercive field (E_c) around $x = 0.04$ – 0.05 can be strong evidences for this mechanism. At $x = 0.10$, the strain loops with small negative strain and low remnant polarization show a transition from a normal ferroelectric to relaxor-like ferroelectric in the SrTiO₃-modified KNN ceramics [75].

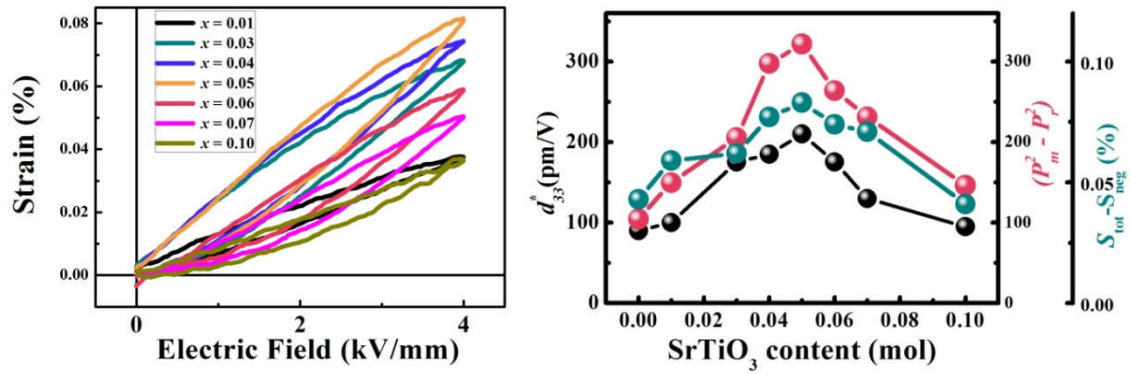


Figure 4.12. The (a) unipolar strain curves (b) normalized strain d_{33}^* , difference $S_{pol} - S_{rem}$ and $P_m^2 - P_r^2$ of KNN–100xST ceramics.

Figure 4.13 performs the phase diagram of KNN–100xST ceramics. The piezoelectric constant d_{33} slightly increased with increasing ST content, culminated in the highest d_{33} value of 130 pC/N at $x = 0.05$ ceramics, then drastically declined with further increasing ST content. In fact, the change in d_{33} values in ferroelectric materials is strongly affected by the dielectric and ferroelectric properties [124], following the relation:

$$d_{33} = 2Q\epsilon_r P_r \quad (3)$$

According to Figure 4.13 (a) and Table 5, the values of ϵ_r increase with the stabilizing

of tetragonal phase. Meanwhile, the decrease of P_r values in Figure 4.13 (c) is resulted from the destabilization of ferroelectrics in KNN ceramics with the increase of modification content. Moreover, the product $\epsilon_r P_r$ values perform the same trend with d_{33} indicates the influence of dielectric and ferroelectric features on the piezoelectric behavior.

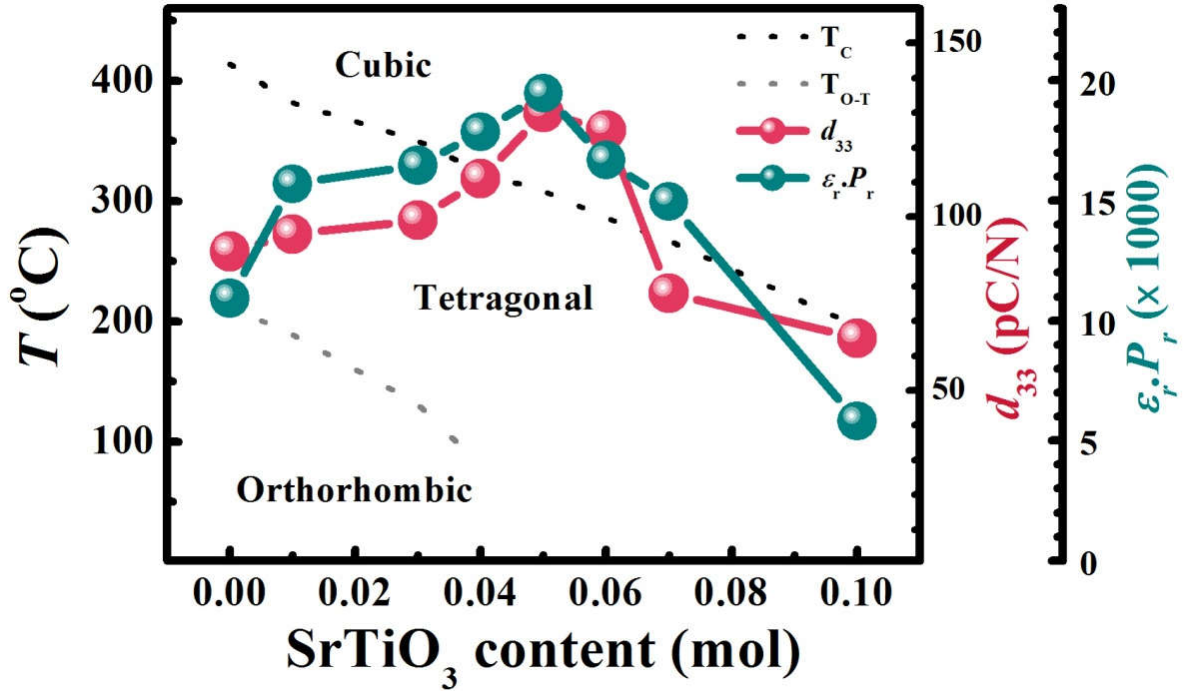


Figure 4.13. Phase diagram of KNN–100xST ceramics.

4.2.3. Conclusion

SrTiO₃ (ST) is a promising candidate for tetragonal phase stabilization on lead-free KNN piezoelectric ceramics. KNN–100xST piezoceramics were prepared using conventional solid-state reaction method to study their phase transition behavior and electrical properties. The polymorphic phase boundary between the orthorhombic and the tetragonal phases is observed at 5 mol% of SrTiO₃ content with the improved piezoelectric constant d_{33} . Meanwhile, the enhancement of normalized strain d_{33}^* for KNN–5ST ceramics may be related with the domain wall flexibility resulting from the

simultaneous contribution of orthorhombic and tetragonal phase. The tetragonality is highest at $x = 0.07$. However, $x = 0.06$ composition maintains high piezoelectric constant, which can be a good candidate for the tetragonal phase component to form the MPB.

4.3. Li⁺ -doping effects on tetragonal phase stabilization of lead-free KNN-ST piezoceramics

From previous part, SrTiO₃-modified Na_{0.5}K_{0.5}NbO₃ (KNN) ceramics can be a good candidate for tetragonal phase stabilization. Tetragonal phase was stabilized and maintained good properties for the modification content of 0.06 mol. Such high amount of SrTiO₃ causes the higher sintering temperature and significantly reduces Curie temperature T_C . To maintain the high T_C and improve the piezoelectric properties, this study investigates the effect of Li-doping on 0.96Na_{0.5}K_{0.5}NbO₃-0.04SrTiO₃ ceramics. The ceramics was denoted as KNN-4ST-100yL, and the fabrication was mentioned in detail in chapter 3, respectively.

4.3.1. Motivation and scope

Lead-based piezoceramics, such as Pb(Zr,Ti)O₃ (PZT), Pb(Mg_{1/3}Nb_{2/3})O₃-PbTiO₃ (PMN-PT) has been widely used for sensors and actuators, due to their excellent properties [3,25,125]. However, these materials contain more than 60% of toxic lead, which has brought serious problems for environment and human being [4]. Recently, many countries strongly developed environment-friendly piezoelectric materials to replace lead-based ones [140,141]. Therefore, the development of lead-free piezoelectric ceramics with excellent electrical properties becomes really necessary [88,90-94].

Among various lead-free materials, K_{0.5}Na_{0.5}NbO₃ (KNN) compounds have been considered as potential candidates for sensors application [94,95]. High Curie temperature T_C around 420°C and large electromechanical coupling factors with the orthorhombic-tetragonal phase transition temperature T_{O-T} around 200°C can be found in

pure KNN [87]. The requirements for sensors application are not only high piezoelectric constant (d_{33}) and T_C , but also the temperature insensitivity of properties. One of methods to improve the thermal stability of piezoelectric properties in KNN-based ceramics is the stabilization of a single tetragonal phase by shifting down the orthorhombic–tetragonal phase transition below room temperature. It is reported that some chemical modifications were used to stabilize the tetragonal phase from the orthorhombic phase in pure KNN, such as Li_2CO_3 [46], BiScO_3 [41], MTiO_3 (with $M = \text{Pb, Ba, Sr, Ca, Bi}_{0.5}\text{Li}_{0.5}\dots$) [42,43], LiMeO_3 (with $\text{Me} = \text{Nb, Ta, Sb}\dots$) [44-46]... Among them, SrTiO_3 is a promising candidate since SrTiO_3 modification can improve piezoelectric properties and sinterability of KNN ceramics [52,75]. Guo *et al.* [75] firstly reported that the crystal structure changed from orthorhombic to tetragonal in the $[(\text{K}_{0.5}\text{Na}_{0.5})_{1-x}\text{Sr}_x](\text{Nb}_{1-x}\text{Ti}_x)\text{O}_3$ ceramics at $x \approx 0.040$ and the value of piezoelectric constant d_{33} almost monotonically decreased with increasing modification content. Wang *et al.* [52] then observed the orthorhombic–tetragonal phase boundary with enhanced dielectric and piezoelectric properties in SrTiO_3 -modified KNN, fabricated using Spark–plasma–sintering method. In section 4.2, we had prepared KNN–100xST piezoceramics using conventional solid–state reaction method. The polymorphic phase boundary between the orthorhombic and the tetragonal phases was observed at 5 mol% of SrTiO_3 content with the improved piezoelectric constant d_{33} . However, such high amount of SrTiO_3 required high sintering temperature (above 1200°C) to obtain the dense sample. Moreover, T_C significantly decreases to lower than 300°C for $x > 0.05$. Guo *et al.* [46] reported that Li_2CO_3 doping is able to stabilize the tetragonal phase and increase T_C . Besides, several studies considered Li_2CO_3 as a good sintering aid to reduce the sintering temperature [142-144]. Therefore, this study investigated the phase transition and piezoelectric properties the effects of Li_2CO_3 -doped $0.96\text{Na}_{0.5}\text{K}_{0.5}\text{NbO}_3$ - 0.04SrTiO_3 ceramics.

4.3.2. Results and discussions

Polished and thermally etched surface images of KNN-4ST-100yL ceramics are displayed in Figure 4.14 (a–f). Abnormal grain growth in KNN-4ST is prevented by Li-doping. The average grain size drastically decreases with the contribution of Li^+ . It was reported in previous Section that 0.04 mol ST was high enough to restrict the movement of grains across the grain boundary causing inhibited grain growth [132,133]. Furthermore, Li_2CO_3 is considered as sintering aid with low melting point at 723°C , the formation for liquid state become easier, that can prevent the process of grain growth, which typically takes place during the final sintering stage [38].

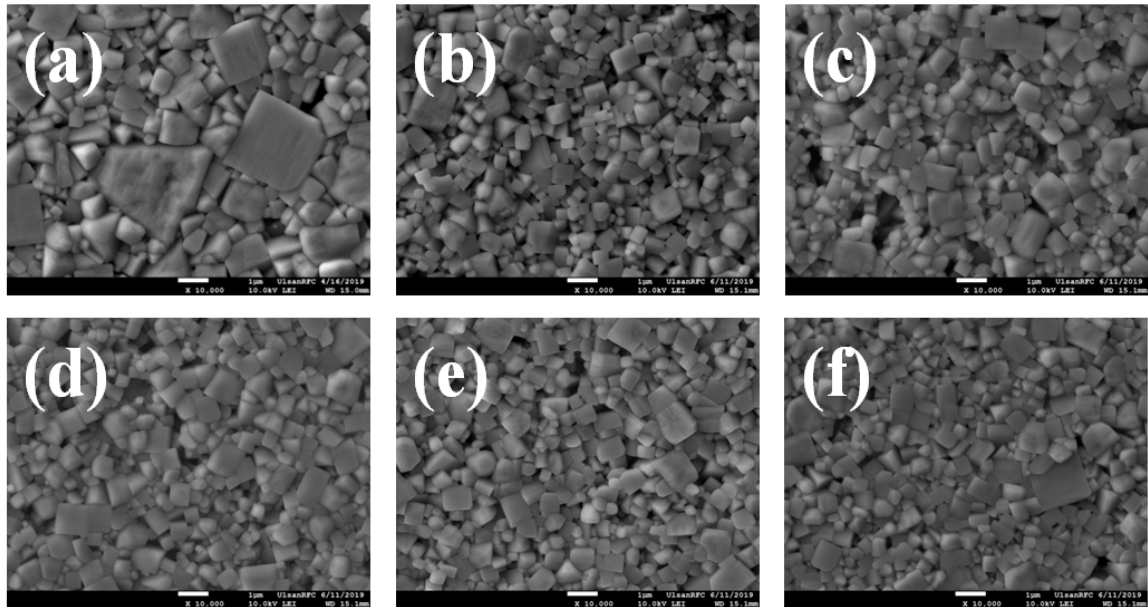


Figure 4.14. Polished and thermally etched surface images of lead-free KNN-4ST-100yL ceramics (a) $y = 0$, (b) $y = 0.01$, (c) $y = 0.02$, (d) $y = 0.03$, (e) $y = 0.04$, and (f) $y = 0.06$

Figure 4.15 (a,b) shows the X-ray diffraction patterns of the KNN-4ST-100yL ceramics at room temperature. Single perovskite structure without significant secondary phases in all samples indicates the formation of a solid solution among the KNN, SrTiO₃ and Li₂CO₃. To clarify changes of crystal structure for all compositions, (200) reflections with 2θ range of 44.4° ~ 46.4° are shown in Figure 4.15 (b). Two distinct peaks as (202) and (020) clearly observed KNN-4ST and KNN-4ST-1L compositions correspond to orthorhombic structures. When Li⁺ content $y \geq 0.03$, the intensity of peaks at (200) reflections are moderately reversed, corresponding to the (002) and (200) peaks of tetragonal symmetry. The changing of relative height of peaks around $y = 0.02$ considers the phase transition from orthorhombic to tetragonal phase. The lattice parameters and tetragonality were calculated from XRD data and shown in Figure 4.9 (c). The broader space between (002) and (200) peaks implies that difference between lattice parameter a and c for tetragonal phase becomes larger with further Li⁺ content, resulting the higher tetragonality c/a . Even for the composition at the phase transition, the tetragonality is stronger than that of KNN-7ST.

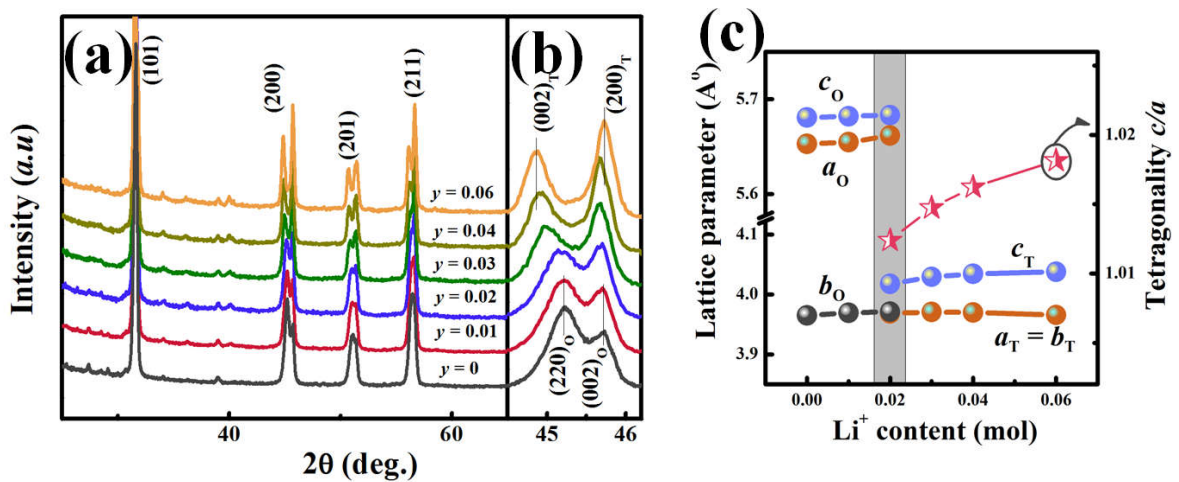


Figure 4.15. X-ray diffraction patterns of KNN-4ST-100yL ceramics as a function of Li content in the 2θ ranges of (a) 20°–70°, (b) 44.4°–46.4°, and (c) lattice parameter.

The temperature dependent dielectric constant of KNN–4ST–100yL compositions are shown in Figure 4.16 (a). The orthorhombic–tetragonal phase transition temperature (T_{O-T}) and Curie temperature (T_C) are detected by the corresponding peaks in the graphs of dielectric constant and plotted in Figure 4.16 (b). With the increasing of Li^+ content, T_{O-T} is shifted from 80°C for KNN–4ST to near room temperature for $y = 0.01$ and cannot be observed for $y \geq 0.02$ compositions. This implies that those samples are stabilized as a tetragonal phase. Meanwhile, T_C monotonically increases with further doping amount.

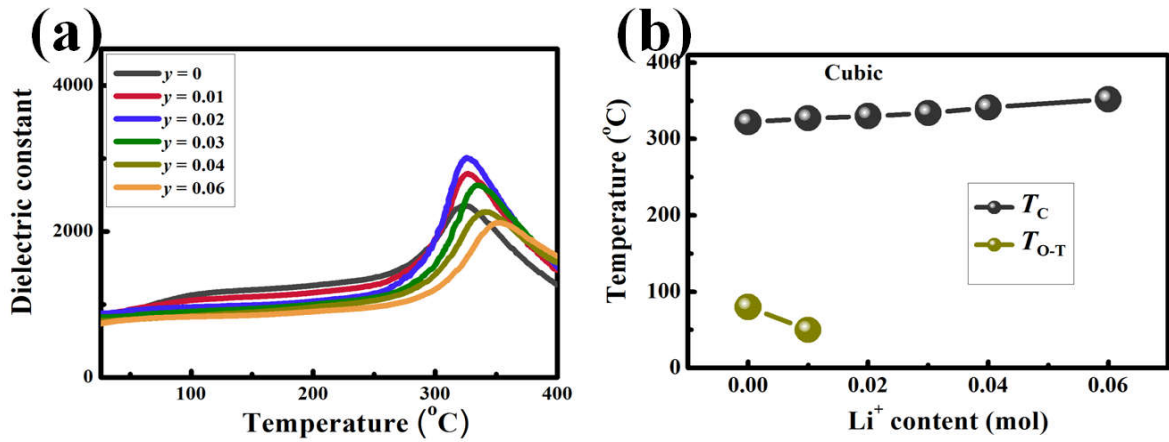


Figure 4.16. (a) Temperature–dependent dielectric dielectric constant ϵ_r of KNN–4ST–100yL ceramics, and (b) the extracted phase transition temperatures as a function of Li^+ content.

Figure 4.17 shows the polarization (P – E) and bipolar strain (S – E) curves for KNN–4ST–100yL ceramics measured under an electric field of 4kV/mm, and the extracted parameters such as maximum polarization (P_m), remanent polarization (P_r), coercive field (E_c), negative strain (S_{neg}), and maximum strain (S_{max}) values. The features of ferroelectric material can be observed in KNN–4ST ceramics, and degraded with the reducing of P_m and P_r when Li^+ content increase. The strain curves for $y \geq 0.03$ compositions with small negative strain may be related with the dissociation of ordered ferroelectricities, and these materials can be considered as relaxor–like ferroelectric.

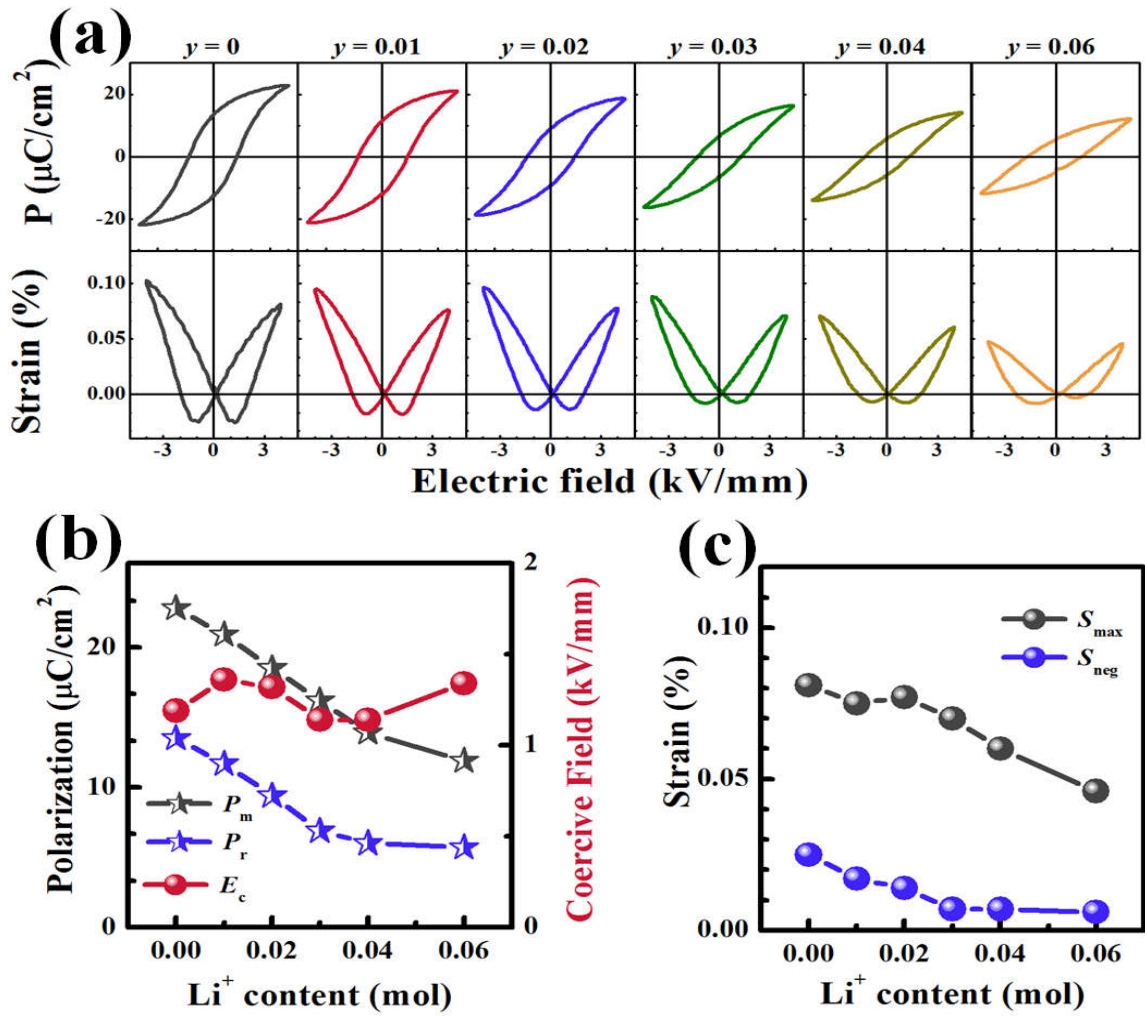


Figure 4.17. (a) Polarization and bipolar strain curves, (b), P_{\max} , P_r , E_c values (c) S_{\max} , S_{neg} values of KNN-4ST-100yL ceramics

Piezoelectric constant d_{33} , electromechanical coupling factor $k_{p,r}$ and phase transition temperature of KNN-4ST-100yL ceramics are shown in Figure 4.18. The piezoelectric constant d_{33} firstly increased with increasing Li^+ content, culminated in the highest d_{33} value of 165 pC/N at $y = 0.02$ ceramics, then drastically declined with further increasing doping content. The electromechanical coupling factor k_p performs the similar trend with d_{33} , corresponding to the orthorhombic-tetragonal polymorphic phase transition.

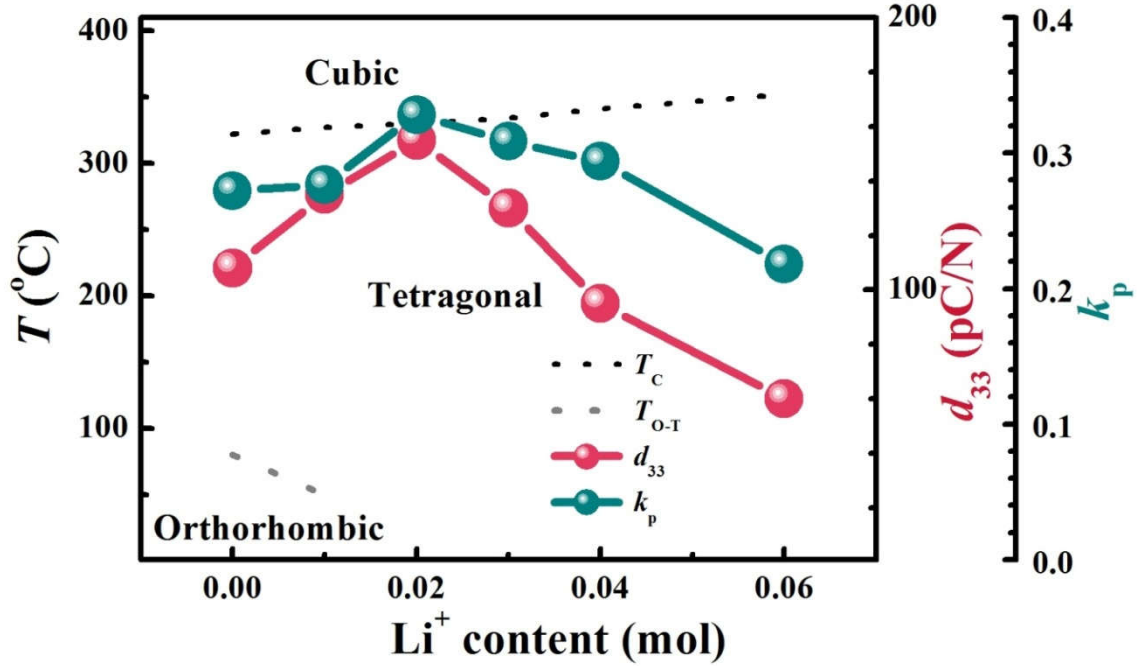


Figure 4.18. Piezoelectric constant d_{33} , electromechanical coupling factor k_p , and phase transition temperature of KNN-4ST-100yL ceramics.

4.3.3. Conclusion

Lead-free KNN-4ST-100yL piezoceramics have been prepared by the solid-state reaction method. Firstly, the sintering temperature was significantly decreased with the contribution of Li_2CO_3 doping. All the prepared samples show the single perovskite phase with the structure change from orthorhombic (O) to tetragonal (T) at room temperature with the increasing of Li content. The temperature-dependent permittivity, XRD and piezoelectric measurements have been carried out to study the phase transition. The orthorhombic-tetragonal phase transition was observed at 2 mol% Li_2CO_3 modified KNN-4ST, with T_C , d_{33} and k_p are 328°C , 165pC/N and 0.33 , respectively. The tetragonality is much higher than those values for KNN-100xST ceramics. Finally, KNN-4ST-4L can be considered as a good candidate for the tetragonal phase component.

4.4. Ferroelectric-to-relaxor crossover in KNN-based lead-free piezoceramics

This study investigated the phase transition behavior and electrical properties of $(\text{K}_{0.5}\text{Na}_{0.5})(\text{Nb}_{1-x}\text{Zr}_x)\text{O}_3$ (KNN-100xZ) and $(\text{K}_{0.5}\text{Na}_{0.5})\text{NbO}_3-y\text{BaZrO}_3$ (KNN-100yBZ) lead-free piezoelectric ceramics. The phase transitions in crystal structures were compared in KNN ceramics between single Zr^{4+} doping and $\text{Ba}^{2+}\text{Zr}^{4+}$ co-doping. Piezoelectric properties such as the piezoelectric constant (d_{33}) and electromechanical coupling factor (k_p) are optimized for KNN-6BZ ceramics and were clarified via the polymorphic phase transition from the orthorhombic to pseudocubic phase. The fitted degree of diffuseness (γ) for a phase transition from the modified Curie-Weiss law indicated that KNN ceramics as ferroelectrics are gradually transformed through BaZrO_3 modification. Accordingly, the enhanced strain properties at $y = 0.08$ consist of coexisting ferroelectric domains and polar nanoregions that are supported by ferroelectric-to-relaxor crossover in KNN-100yBZ ceramics. The ceramic fabrication was mentioned in detail in chapter 3, respectively.

This work has been published on Ceramics International journal (10/2020).

4.4.1. Motivation and scope

Lead-based piezoceramics such as $\text{Pb}(\text{Zr}_{0.52}\text{Ti}_{0.48})\text{O}_3$ (PZT), $\text{Pb}(\text{Mg}_{1/3}\text{Nb}_{2/3})\text{O}_3\text{-PbTiO}_3$ (PMN-PT), and $(\text{Pb,L a})(\text{Zr,Ti})\text{O}_3$ (PLZT) are widely implemented in electronic and electric devices as actuators, sensors, and microelectronic devices due to their superior electrical properties [1-3]. However, the high toxicity of lead (Pb) in wastes of such devices causes serious problems for the environment and human health [4]. Therefore, replacement of lead-based materials with lead-free ones is an important issue in piezoceramics [94]. Several kinds of lead-free piezoceramics have been extensively

investigated, such as BaTiO₃ [5,6], (Bi_{1/2}Na_{1/2})TiO₃ [7,8], and (K_{0.5}Na_{0.5})NbO₃ (KNN) [9-11]. The unique advantages of KNN ceramics such as their high Curie temperature ($T_C \approx 420^\circ\text{C}$) and high piezoelectricity suggest them as a promising candidate for replacing lead-based materials [9,10,145]. Therefore, significant attention has been given to the investigation of KNN-based lead-free ceramics. In fact, the above mentioned major properties of KNN-based lead-free ceramics can be further improved by modifying with other impurities or ABO₃ [12].

Several promising achievements were recently reported in KNN-based ceramics regarding the construction of new phase boundaries, especially for morphotropic phase boundary (MPB) concepts such as PZT [10,12,146]. One MPB forming method is the stabilization of two phases consisting of a tetragonal (T) phase and a rhombohedral (R) phase. There are many candidates to stabilize the T phase at room temperature in KNN-based system [42,147,148], but relatively few materials exhibit rhombohedral symmetry at room temperature. Wang *et al.* (2009) first clarified that the orthorhombic (O)-R phase transition temperature (-120°C for pure KNN) was tuned to above room temperature in solid solution $(1-x)\text{Na}_{0.5}\text{K}_{0.5}\text{NbO}_3-x\text{BaZrO}_3$ for $0.08 \leq x \leq 0.15$ [47]. Then, it was reported that the O-R phase transition for KNN ceramics is almost independent of the A-site ions [48]. Other additives have been used to bring the T_{R-O} of KNN from -123°C to above room temperature, such as Sb⁵⁺ [49,50] and BiScO₃ [51]. After that, there were other studies on forming R-T phase boundaries in KNN-based ceramics by modifying BaZrO₃ (BZ) [112,113,118]. However, this concept is controversial even though most studies claimed that the R phase in KNN ceramics can be stabilized using AZrO₃ (A = Ba, Ca, Sr ...). Although, it is well known that Zr-based compounds such as (AZrO₃) are strongly influence the stabilization of R phase in KNN-based ceramics, we could not find any evidences for those features in a single Zr⁴⁺-doped KNN-based ceramics [102,149]. In fact, some studies have recently suggested stabilization of a

relaxor based on noncubic (more precisely, orthorhombic or tetragonal) phases that transit to pseudocubic phases [68-73]. The KNN-based relaxors exhibit some features, such as the extremely broad maximum in temperature dependent permittivity, diffuse phase transitions, and Vogel–Fulcher relaxations [74]. Guo *et al.* [75] firstly suggested that Sr^{2+} and Ti^{4+} co-doping in KNN ceramics can induce phase transition from the normal ferroelectric to relaxor ferroelectric with the diffuse phase transition behaviors. Kosec *et al.* [76] and Bobnar *et al.* [77] observed the relaxor behavior through a broad dispersive dielectric maximum and a Vogel–Fulcher relationship in KNN– SrTiO_3 ceramics. These relaxor features has been also observed in other KNN-based ceramics systems such as KNN– BaTiO_3 [78,79], KNN– $\text{Bi}_{0.5}\text{Na}_{0.5}\text{TiO}_3$ [80], KNN– BiFeO_3 [81], KNN– SrZrO_3 [82], and so on. Accordingly, these imply that there are still arguments regarding the definition of stabilized phases in KNN ceramics by modifying Zr-based compounds. Therefore, this study investigated the crystal structure, phase transition behavior, and electrical properties of BZ–modified KNN ceramics. Moreover, to clarify the stabilized phases in KNN ceramics, we compared single Zr^{4+} doping with $\text{Ba}^{2+}\text{Zr}^{4+}$ co-doping and their effects on the phase transition behavior and electrical properties of KNN ceramics.

4.4.2. Results and discussions

The polished and thermally etched surface images of the KNN–100xZ and KNN–100yBZ ceramics are displayed in Figure 4.19. The densities of the sintered samples were recorded around 4.2–4.7 g/cm^3 , corresponding to the relative density being higher than 94%. All samples show dense microstructures with very small amounts of holes and abnormal grain distributions, with large grains surrounded by smaller ones. The average grain size of Zr-doped KNN ceramics increased dramatically from 0.59 ± 0.03 μm to 1.25 ± 0.07 μm when $x = 0.01$, then decreased rapidly with further increasing Zr

amount $x = 0.05$, as shown in Figure 4.19(a–c). Meanwhile, with increasing BZ content, the average grain size first increased, reaching the largest grains ($1.67 \pm 0.04 \mu\text{m}$) when $y = 0.03$, then monotonically decreased. Accordingly, it seems that the low concentrations of ZrO_2 and BaZrO_3 are responsible for grain growth, while the high concentrations of ZrO_2 and BaZrO_3 restrained the grain growth. The reason for this is that a low content of Ba or BaZrO_3 can be well diffused into the KNN lattices to form a new homogeneous solid solution [150]. On the other hand, some of the BaZrO_3 particles at high content may exist near the grain boundary, which was responsible for the restrained grain growth [129,130,150,151].

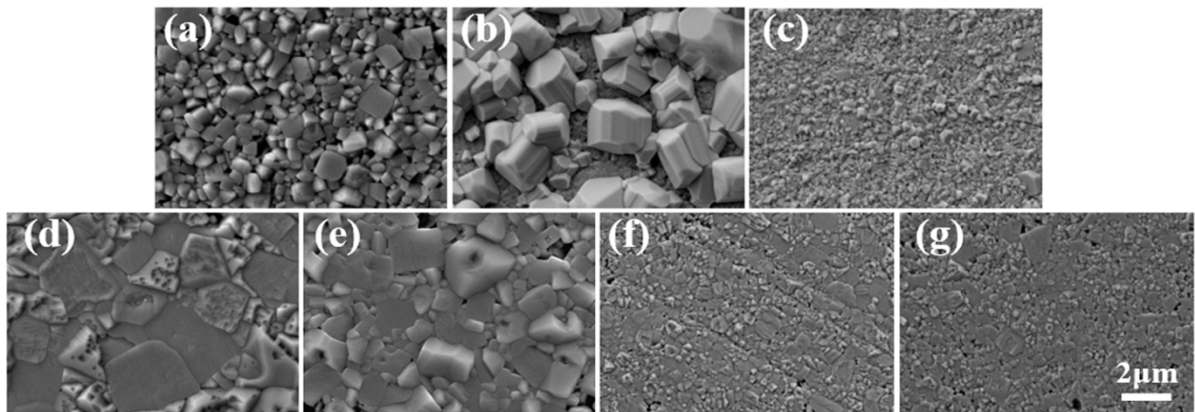


Figure 4.19. The polished and thermally etched surface images of KNN-based ceramics, (a) pure KNN (b) KNN-1Z, (c) KNN-5Z, and KNN-100 y BZ ceramics for (d) $y = 0.03$, (e) $y = 0.06$, (f) $y = 0.08$, (g) $y = 0.10$.

Figure 4.20 displays the XRD patterns at room temperature for pure KNN, Zr- and BaZrO_3 -modified KNN ceramics. A single perovskite structure without significant secondary phases was obtained from each sample, indicating the formation of a stable solid solution among KNN, ZrO_2 or BaZrO_3 . To clarify these changes in crystal structure for all compositions, 2θ ranges of 29.6° – 33.2° and 44.0° – 46.5° peaks are shown in Figure

4.20(d) and (e). In the case of pure KNN and single Zr^{4+} -doped KNN-100xZ ceramics, two distinct peaks as (200)/(002) and (020) were clearly observed near 45° of 2θ regardless of Zr^{4+} concentration, which corresponds to the orthorhombic structures. This implies that a crystallographic phase transition was not induced by single Zr^{4+} doping in KNN ceramics. KNN-3BZ ceramics with a low BZ concentration were clarified to have an orthorhombic structure with a couple of peaks. On the other hand, the split (020) peak for KNN-6BZ ceramics was started to approach into (200)/(002) peak, which was merged into a single (200) peak corresponding to rhombohedral or pseudocubic structure at KNN-8BZ ceramics. Moreover, the single (110) peaks near 30° of 2θ were detected at $y \geq 0.08$ compositions. This result implies that the stabilized crystal structures for KNN-100yBZ ceramics with $y \geq 0.08$ of BZ content are identified as pseudocubic structure [1,152,153]. This indicates that a phase transition was induced by Ba^{2+} and Zr^{4+} co-doping in KNN ceramics. This can be explained by the different sizes of ionic radii between impurities (Ba^{2+} and Zr^{4+}) and elements for the A-/B-sites in the KNN lattice, which are responsible for the crystallographic phase transition based on peak shifting. In fact, the ionic radii for Ba^{2+} (1.61 Å) and Zr^{4+} (0.72 Å) are larger than the average ionic radii for A-site (1.52 Å) ions (precisely, 1.64 Å for K^+ and 1.39 Å for Na^+) and Nb^{5+} (0.64 Å) as B-site ion, respectively. Therefore, it can be assumed that the (020) peak was preferentially shifted to the (200)/(002) peak, then the merged (200) peak was subsequently extended by modifying BZ further.

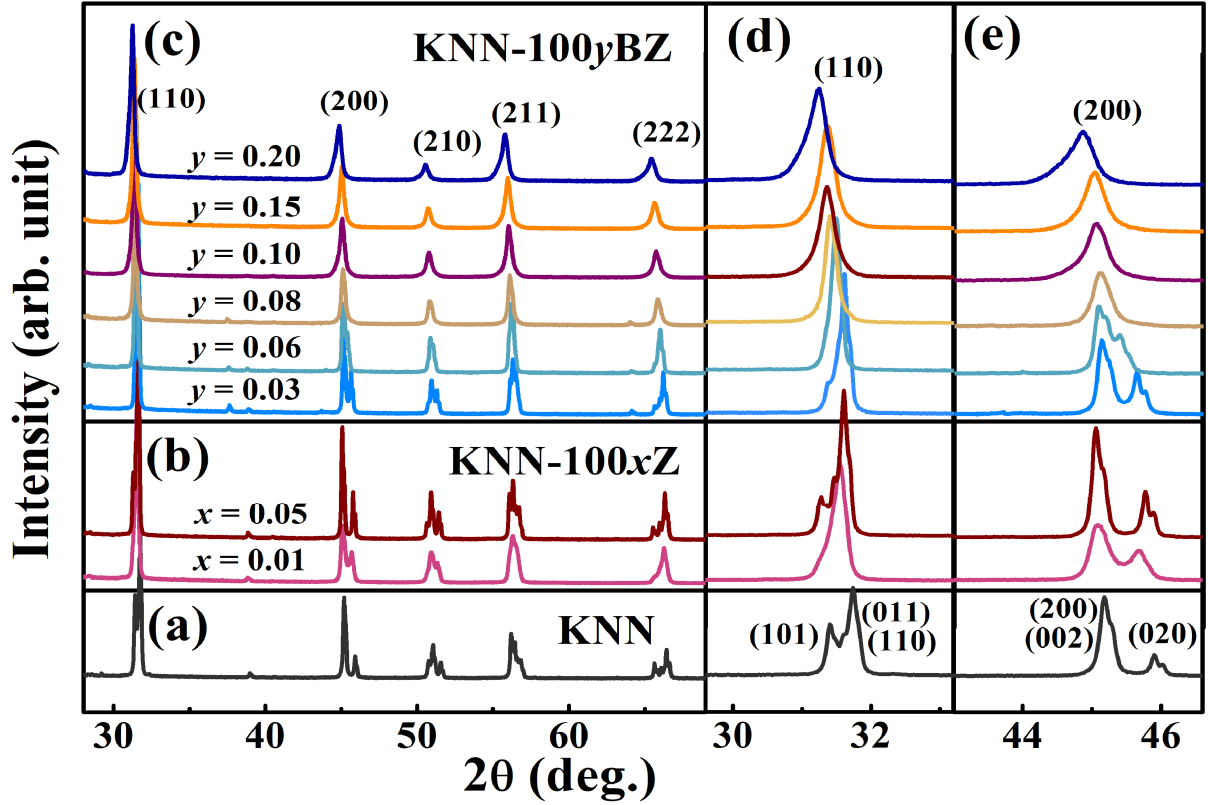


Figure 4.20. X-ray diffraction patterns of (a) pure KNN, (b) KNN-100xZ, (c) KNN-100yBZ ceramics in the 2θ ranges of 20° – 70° , (d) 29.6° – 33.2° and (e) 43° – 46.6° .

Temperature-dependent dielectric properties for KNN, KNN-100xZ, and KNN-100yBZ ceramics are depicted in Figure 4.21. As is well known, the Curie temperature (T_C) and an orthorhombic to tetragonal phase transition temperature (T_{O-T}) for pure KNN were observed near 410°C and 210°C , respectively. In the case of single Zr^{4+} doping, both T_C and T_{O-T} for KNN-1Z ceramics were decreased to 376°C and less than 200°C , respectively. By further increasing the single Zr^{4+} content, T_C no longer changed, while discontinuities in the dielectric behavior at T_{O-T} were prevented. On the other hand, T_C and T_{O-T} for KNN-100yBZ ceramics were decreased with increasing BZ content [47]. Finally, T_{O-T} was vanished at KNN-8BZ ceramics. The frequency-independent dielectric behaviors with sharp phase transitions as features of the

normal ferroelectrics were also determined for pure KNN, KNN-1Z, and KNN-6BZ ceramics, as seen in Figure 4.21(b), (c), and (d). However, frequency-dependent dielectric behaviors with a broad phase transition as a function of the applied frequency was detected in the KNN-8BZ ceramics, which became stronger with dispersion as the BZ content increased. From Figure 4.20, which displays the crystal structures, and Figure 4.21, which displays the dielectric properties, it can be assumed that single Zr^{4+} doping weakly influenced the phase transition in KNN ceramics, while Ba^{2+} and Zr^{4+} co-doping strongly influenced dielectric properties based on the phase transition in KNN ceramics (more precisely, this transition can be defined as a ferroelectrics to relaxor phase transition [154])

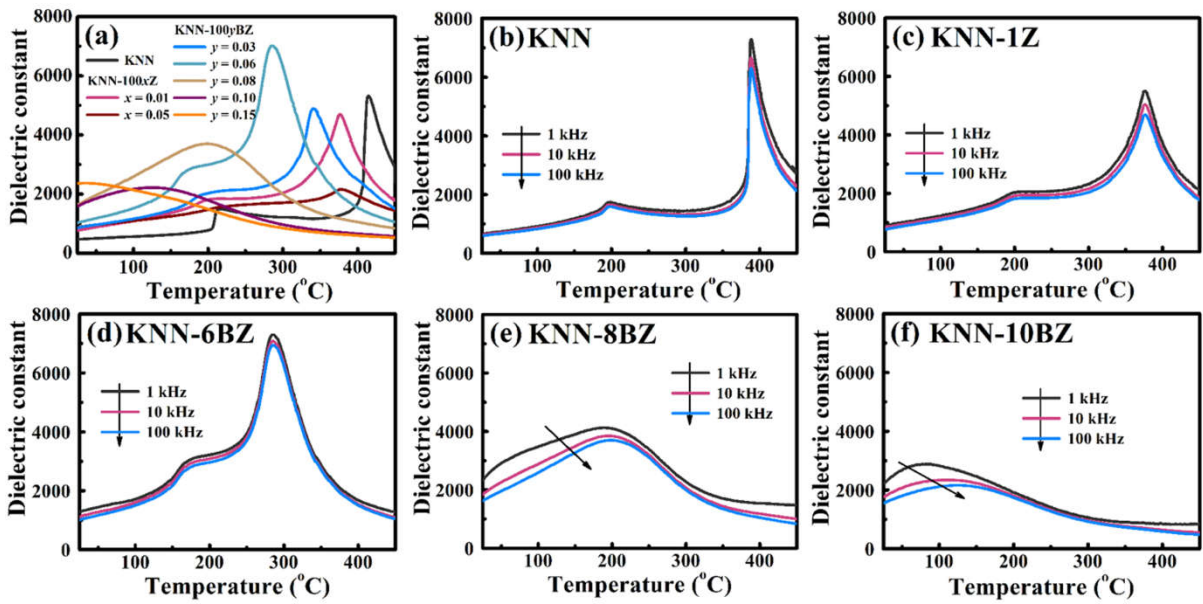


Figure 4.21. Temperature-dependent dielectric constant (ϵ_r) for (a) all compositions at 100 kHz and (b) pure KNN, (c) KNN-1Z, (d) KNN-6BZ, (e) KNN-8BZ, and (f) KNN-10BZ ceramics.

Figure 4.22 indicates the polarization ($P-E$) and strain ($S-E$) curves for KNN, KNN-100xZ, and KNN-100yBZ ceramics, which were considered under an electric field

of 4kV/mm. Furthermore, the extracted parameters such as the dielectric constant (ϵ_r), remanent polarization (P_r), coercive field (E_c), negative strain (S_{neg}), and maximum strain (S_{max}) values are compared as a function of impurity content in Figure 4.23. For the compositions with Z content $x \leq 0.01$ and BZ content $y \leq 0.08$, typical ferroelectric features were observed with butterfly-shaped $S-E$ and square-shaped $P-E$ curves. On the other hand, both the strain and polarization properties for KNN-5Z ceramics were drastically decreased by single Zr^{4+} doping and relatively weak ferroelectricity based on degradation of the P_r , E_c , and S_{neg} values in the KNN-8BZ ceramics. With increasing BZ content, the strain and polarization properties were degraded. The highest S_{max} was obtained at KNN-8BZ ceramics with drastically decreasing E_c and S_{neg} . These results are strongly related to the appearance of relaxor features based on a pseudocubic structure. In fact, the destabilization of ferroelectrics (in other word, the stabilization of the relaxor) is caused by the dissociation of long-range order ferroelectricities based on compositional disorder and lattice distortion. It was reported that ferroelectrics-relaxor transitions can be strongly affected by co-doping heterovalent substitutions, for instance $(1-x)K_{0.5}Na_{0.5}NbO_3-SrTiO_3$ [126], $(Ba_{1-x}K_x)(Ti_{1-x}Ta_x)O_3$ [155], $(Ba_{1-x}K_x)(Ti_{1-x}Nb_x)O_3$ [156], and $(1-x)BaTiO_3-BiAlO_3$ [157]. Accordingly, in the $BaZrO_3$ -modified KNN perovskite lattice, Ba^{2+} replaces K^+ and Na^+ on the A-site donor, while Zr^{4+} replaces Nb^{5+} on the B-site. It is believed that these substitutions lead to the compositional (chemical) disorder from different ions on equivalent crystallographic sites, which can disrupt the long-range order dipoles in ferroelectric materials [157-159]. At low levels of modification, the long-range dipolar interactions are still preserved since the heterogeneous distribution is relatively negligible compared with homogeneous ferroelectric polar states [160], thus KNN-3BZ and KNN-6BZ ceramics are still normal ferroelectric materials with large P_r and S_{neg} . With increasing BZ content, the degree of compositional disorder becomes significant, and the relaxor features appear with an

increasing number of polar nanoregions (PNRs) and local fields. Moreover, both KNN sites are modified by Ba^{2+} and Zr^{4+} with a larger ionic radius, which also can be considered as another mechanism that stabilizes the relaxor. There are various cases of relaxor systems that appear regardless of the chemical valence on one or both sites, such as $(\text{Ba}_{0.95}\text{Ca}_{0.05})(\text{Zr}_x\text{Ti}_{1-x}\text{O}_3)$ [68], $\text{BaZr}_x\text{Ti}_{1-x}\text{O}_3$ [161], and $\text{Pb}_{1-x}\text{Ca}_x\text{TiO}_3$ [162]. It was reported that the periodicity of the lattice structure can be influenced by the modified clusters and lattice distortion. In this case, once a couple of cations with different ionic sizes occupy the same crystallographic sites, BO_6 octahedral clusters are changed and lattice distortions are generated in the materials [163,164]. Accordingly, long-range ordered ferroelectricity can be dissociated by the lattice distortion-derived random fields [165]. Therefore, it is believed that the relaxor features in KNN–8BZ, KNN–10BZ, and KNN–15BZ ceramics are revealed.

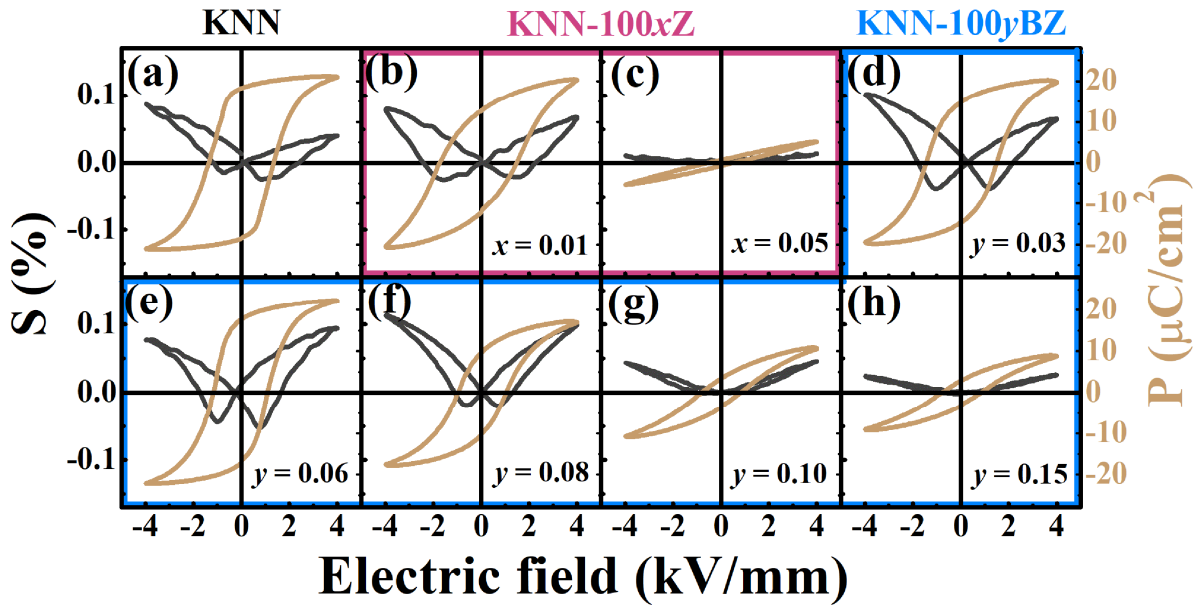


Figure 4.22. Electric-field-induced strain and polarization curves for (a) KNN, KNN–100xZ ceramics as red blocks, (b) $x = 0.01$, (c) $x = 0.05$, and KNN–100yBZ ceramics as blue blocks; similarly for (d) $y = 0.03$, (e) $y = 0.06$, (f) $y = 0.08$, (g) $y = 0.10$, (h) $y = 0.15$.

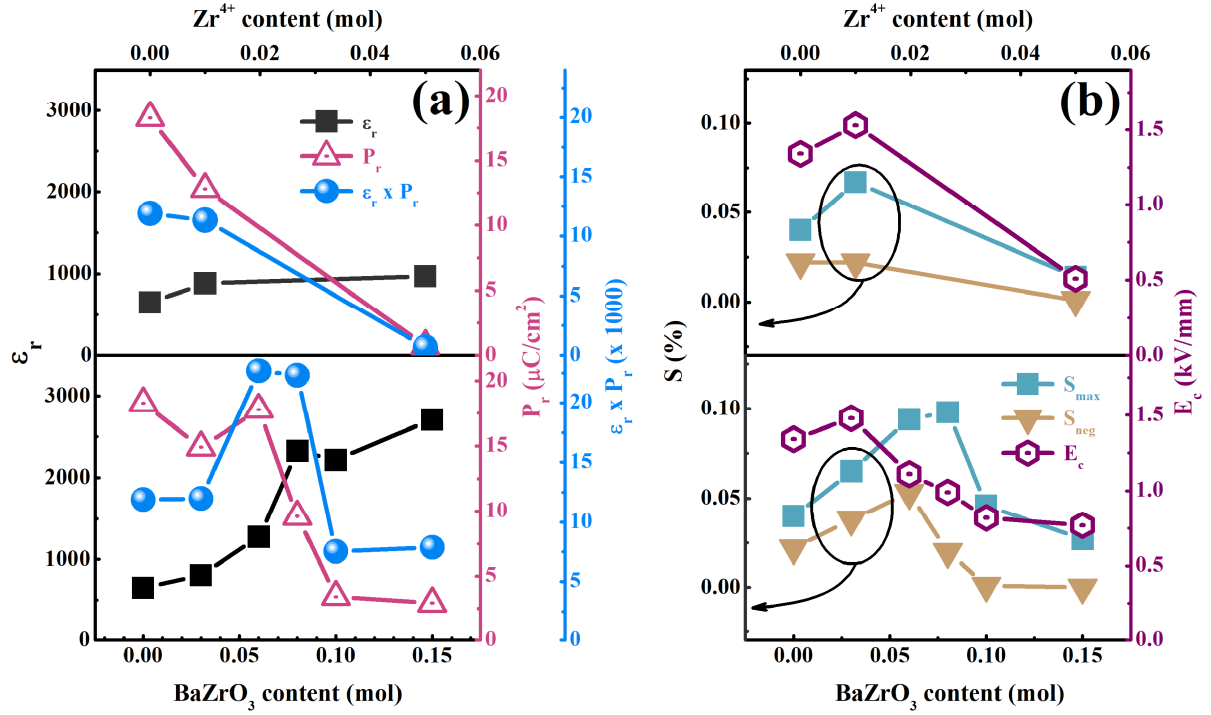


Figure 4.23. The (a) dielectric, ferroelectric, and (b) strain properties of KNN, (top) KNN–100xZ and (bottom) KNN–100yBZ ceramics.

The values of piezoelectric constant (d_{33}) and electromechanical coupling factor (k_p) were determined by using three samples for each composition. Relative errors for the obtained results were consistent, which were less than 10%. At 1 mol % of ZrO_2 doping, d_{33} rapidly decreased to less than 50% compared with pure KNN, then mostly vanished when $x = 0.05$. In the case of KNN–100yBZ ceramics, d_{33} slightly increased with increasing BZ content, then culminated in the highest d_{33} value of 135 pC/N at KNN–6BZ ceramics, which drastically declined with further increasing BZ content. It is noted that these changes in d_{33} values for KNN–100yBZ ceramics are strongly related to the dielectric and ferroelectric properties. In fact, d_{33} can be evaluated by Equation (1):

$$d_{33} = 2Q\epsilon_r P_r \quad (1)$$

where Q , ε_r , and P_r are the electrostrictive coefficient, dielectric constant, and remanent polarization values, respectively. Accordingly, this indicates that changes in d_{33} values are strongly influenced by variations in the $\varepsilon_r P_r$ values, which are compared in the bottom of Figure 4.23(a). Additionally, the k_p values for KNN–100yBZ ceramics monotonically decreased after BZ modification. Furthermore, we suggest that the destabilization of ferroelectrics (in other words, stabilization of the relaxor) is responsible for the degradation of small signal electrical properties such as piezoelectric constant (d_{33}) and electromechanical coupling factor (k_p) in for KNN–100yBZ ceramics.

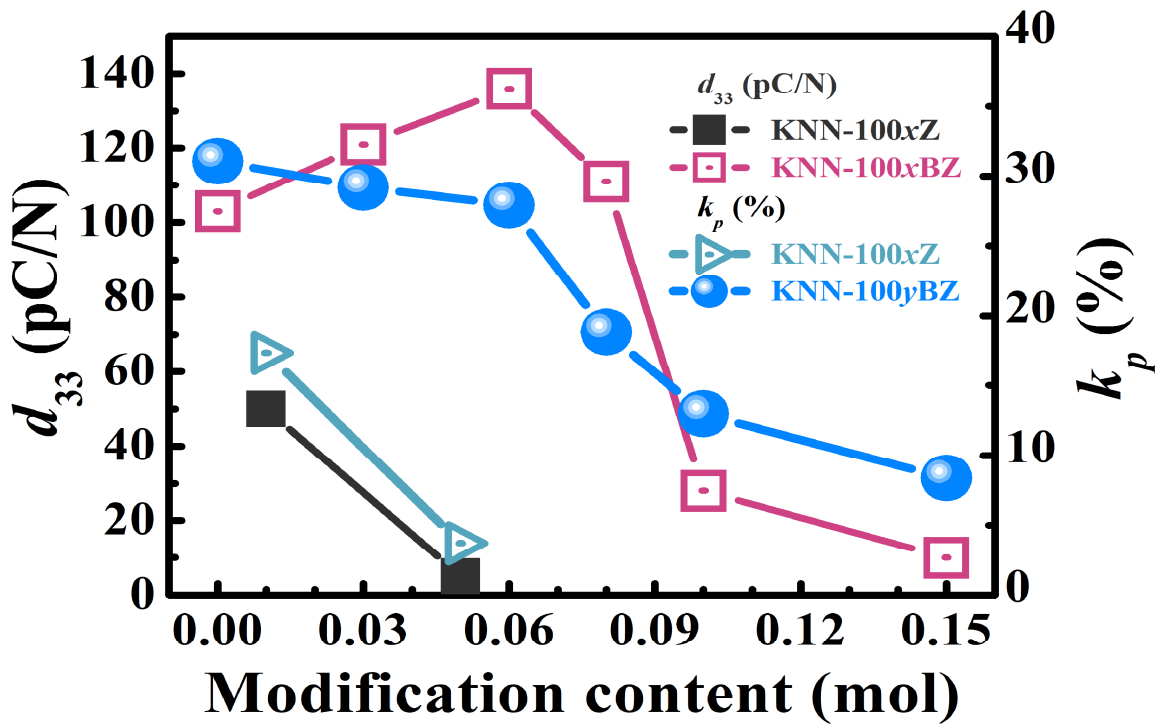


Figure 4.24. Changes in the piezoelectric constant (d_{33}) and electromechanical coupling factor (k_p) for pure KNN, KNN–100xZ, and KNN–100yBZ ceramics.

To clarify the ferroelectrics relative to relaxor crossover behavior in KNN–100yBZ ceramics, we investigated the diffusivity of dielectric properties (diffused phase transition)

for KNN–100yBZ ceramics, which are presented in Figure 4.25. It is known that normal ferroelectrics according to the Curie–Weiss law are satisfied at $T_C < T$, while the relaxor behavior based on diffused phase transition strongly deviates [166]. Further understanding this behavior, the reciprocal of the dielectric constant ($1/\varepsilon'$) for KNN–100yBZ ceramics as a function of temperature at 1 kHz was compared in Figure 4.25(a). As we discussed earlier, 8 mol% BZ–modified KNN ceramics revealed a diffused phase transition with a broad dielectric maximum peak, as is exhibited in Figure 4.21(e). This phenomenon well–matches with the $1/\varepsilon'$ behaviors that was shown in Figure 4.25(a). Moreover, the evaluated Curie–Weiss temperatures (T_{CW}) as determined by tangent lines for all compositions were well matched with the dielectric maximum temperature T_c for pure KNN, KNN–3BZ, and KNN–6BZ ceramics. On the other hand, T_{CW} for KNN–8BZ, KNN–10BZ, and KNN–15BZ ceramics deviated from the dielectric maximum temperatures T_m , as seen in the inset of Figure 4.25(a).

To further determine the diffusivity for phase transition of KNN–100yBZ ceramics, we utilized equation (2) as the modified Curie–Weiss law to evaluate the diffuseness degree [167]:

$$\frac{1}{\varepsilon} - \frac{1}{\varepsilon_m} = \frac{(T - T_m)^\gamma}{C_2} \quad (2)$$

where ε_m , C_2 , and γ are the maximum dielectric constant, the Curie constant, and the degree of diffuseness, respectively. The plots of $\log(1/\varepsilon' - 1/\varepsilon'_m)$ versus $\log(T - T_m)$ at 1 kHz for KNN–100yBZ ceramics are provided in Figure 4.25(b), with the γ values fitted from the slopes of best fit lines. The fitted results are exhibited as an inset in Figure 4.25(b). The γ values were found to be 1.56, 1.28, 1.60, 1.89, 1.87 and 2.00 for $y = 0, 0.03, 0.06, 0.08, 0.10,$ and 0.15 , respectively. In fact, it is known that the γ value for normal ferroelectric materials approached “1”, whereas “2” is seen for the ideal relaxor [168].

Accordingly, it can be determined that pure KNN, KNN-3BZ, KNN-6BZ are ferroelectrics, while KNN-8BZ, KNN-10BZ, KNN-15BZ ceramics can be categorized as relaxors.

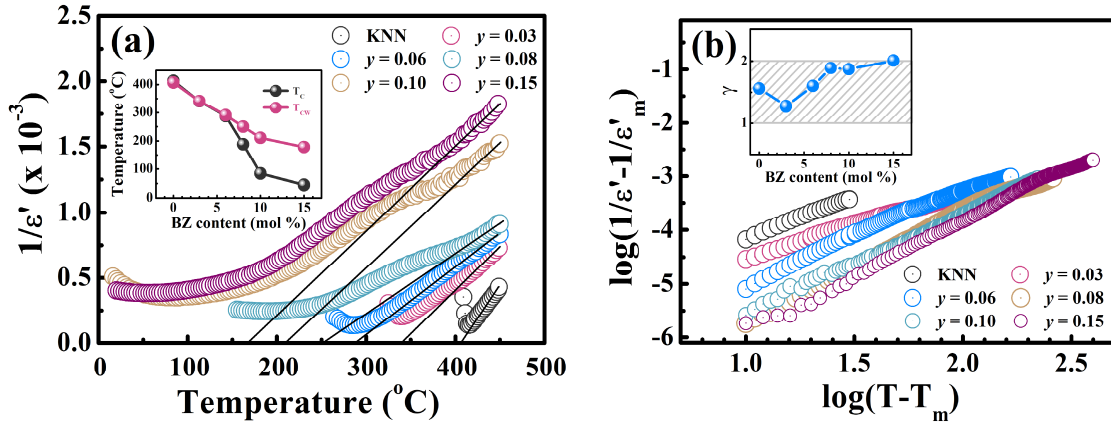


Figure 4.25. Evaluation of diffused phase transition for KNN-100yBZ ceramics using (a) the reciprocal of the dielectric constant ($1/\epsilon'$) as a function of the temperature and (inset) T_{CW} ; (b) the $\log(1/\epsilon' - 1/\epsilon'_m)$ vs. $\log(T - T_m)$ plot at 1 kHz and (inset) the fitted γ values for KNN-100yBZ ceramics.

To better understand the relationship between the stabilized relaxor and changes of electrical properties in KNN-based ceramics, a schematic diagram for three different states of pure KNN, KNN-8BZ, and KNN-15BZ ceramics is given in Figure 4.26. Note that this schematic diagram includes the ferroelectrics state with ferroelectric domains (FDs), the relaxor state with polar nanoregions (PNRs) [169], and the intermediate state with a mixture of PNRs and FDs [170]. Figure 4.26(a) shows the status of FDs in different states (i, ii, and iii) according to the dielectric, strain, and polarization behaviors for pure KNN ceramics. This composition can be considered as normal ferroelectric behavior with orthorhombic ($Amm2$) symmetry at room temperature. The main domain structures for pure KNN ceramics are described in terms of the 180° and non- 180°

domains (detailed as 60° , 90° and 120°) [171]. At state (i) where $E = E_c$, the domains are organized in a random configuration, leading to a macroscopically zero polarization that corresponds to the tail of the butterfly-shaped strain curve. Under an external electric field, domains can be reoriented along the field direction, leading to an extrinsic process known as domain switching [172]. This process happens nonlinearly until the polarization vectors in all domains are aligned with the electric field, resulting in the saturated polarization (P_{\max}) and maximum strain (S_{\max}) exhibited in state (ii) [173]. The FDs in this model are described as low mobility static domains with micro size. As a consequence, the aligned polarizations can be strongly maintained in the poling direction even when the external field is removed. Therefore, a large remanent polarization (P_r) and large negative strain (S_{neg}) can be obtained in state (iii). Here, S_{neg} can be defined by the difference in strain values between state (iii) and state (i). To randomize this energetic polarizing, a high coercive field (E_c) in the opposite direction is required.

In the case of KNN–15BZ ceramics as a relaxor state, it is assumed that all FDs of pure KNN ceramics as ferroelectrics have been completely dissociated and that only the PNRs are exhibited via BZ modification. The PNRs can be described as nano-scaled domains with high mobility and electrical response speed in comparison to micro FDs. From state (i) in Figure 4.26(c), it is suggested that the randomized PNRs seem to be responsible for the zero polarization and lowest strain value. When the electric field is applied, PNRs can be easily and immediately reoriented along the field direction. However, it is difficult to completely induce this across the macroscopic domain, even with a strong applied electric field. Thus, the P_{\max} and S_{\max} values at state (ii) are smaller than those of pure KNN. At state (iii) where $E = 0$, PNRs quickly transition back to the initial state, i.e., the randomized state (i) of PNRs. Therefore, a small P_r and a negligible S_{neg} are observed in KNN–15BZ ceramics. In other words, the stabilized relaxor with PNRs is responsible for the electrostriction behavior with low hysteresis in the strain

properties [174].

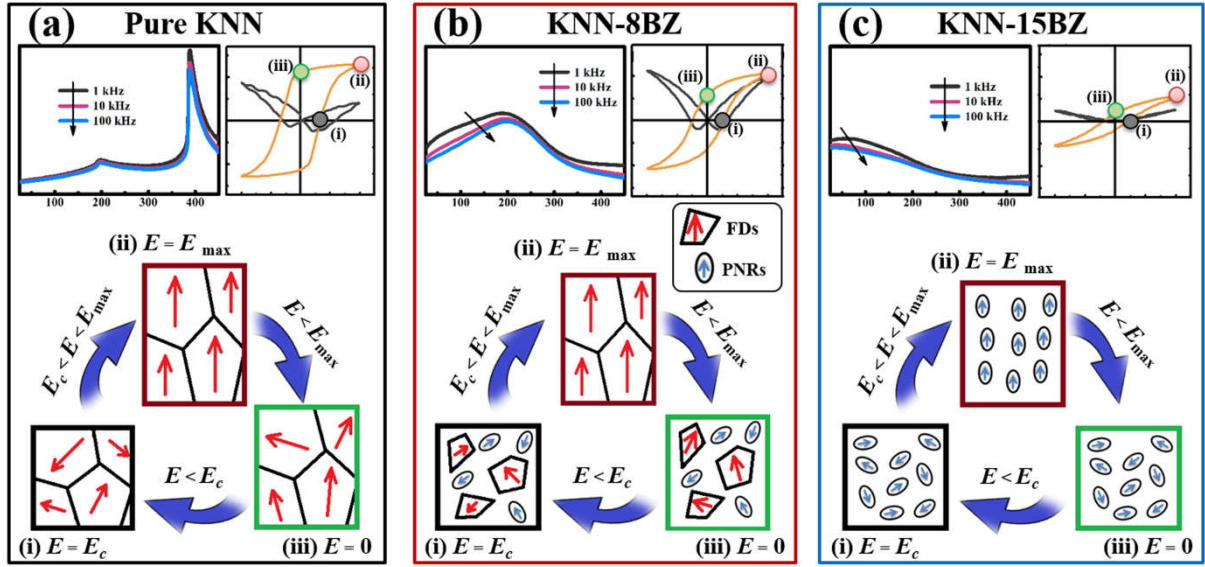


Figure 4.26. Schematic diagram for the three different states of (a) pure KNN, (b) KNN–8BZ, and (c) KNN–15BZ ceramics.

KNN–8BZ ceramics are determined as an intermediate stage at the ferroelectric–to–relaxor crossover with coexistence of the microscopic domains and PNRs. As shown in Figure 4.26(b), the coexisted domains and PNRs are sequentially reoriented to the applied electric field direction. It is noted that the presence of PNRs reduces the energy barrier and supports domain switching as an “accelerator” [175]. Therefore, the significantly decreased E_c with relatively small S_{neg} and enhanced S_{max} may originate from the existence of PNRs with FDs in KNN–8BZ ceramics.

4.4.3. Conclusion

$(K_{0.5}Na_{0.5})(Nb_{1-x}Zr_x)O_3$ (KNN–100xZ) and $(K_{0.5}Na_{0.5})NbO_{3-y}BaZrO_3$ (KNN–100yBZ) lead-free piezoelectric ceramics were successfully prepared by means of a conventional solid-state reaction method. The phase transitions in crystal structures were compared between single Zr^{4+} doping and $Ba^{2+}Zr^{4+}$ co-doping. We found that a crystallographic phase transition was not induced by a single Zr^{4+} doping in KNN ceramics, while the orthorhombic–pseudocubic phase transition was induced by Ba^{2+} and Zr^{4+} co-doping in KNN ceramics. The piezoelectric properties such as the piezoelectric constant (d_{33}) and electromechanical coupling factor (k_p) are optimized with KNN–6BZ ceramics, as clarified by the polymorphic phase transition from the orthorhombic to pseudocubic phases. The degree of diffuseness (γ) for phase transition from the modified Curie–Weiss law indicated that KNN ceramics as ferroelectrics are gradually transformed via $BaZrO_3$ modification. Accordingly, the enhanced strain properties at $y = 0.08$ coexist between ferroelectric domains and PNRs, which is supported by ferroelectric–to–relaxor crossover in KNN–100BZ ceramics.

4.5. New phase boundary in lead-free piezoelectric KNN-based composites

This study investigated a formation of new phase boundary in lead-free KNN-based piezoelectric ceramics. For this work, $0.96(\text{K}_{0.5}\text{Na}_{0.5})_{0.96}\text{Li}_{0.04}\text{NbO}_3-0.04\text{SrTiO}_3$ (KNLN-4ST) and $0.92\text{K}_{0.5}\text{Na}_{0.5}\text{NbO}_3-0.08\text{BaZrO}_3$ (KNN-8BZ) calcined powders have been separately prepared by the solid-state reaction method. According to the X-ray diffraction analysis, KNLN-4ST ceramics was identified as a tetragonal structure (T), while KNN-BZ ceramics was clarified as the pseudocubic phase (PC). The new phase boundary was explored by mixing two compositions with different mixing ratios. To clarify the phase transition behaviors of the formed composites, the various analyses such as temperature-dependent permittivity, temperature-dependent X-ray diffraction (XRD), piezoelectric force microscopy (PFM) and piezoelectric measurements have been carried out. As a result, the new phase boundary was obtained in 70 mol% of T phase content composites. We obtained that room temperature piezoelectric constant (d_{33}) and electromechanical coupling factor k_p of 210 pC/N and 0.35 as the highest values, respectively. The ceramic and composite fabrication was mentioned in detail in chapter 3, respectively.

4.5.1. Motivation and scope

Lead-based piezoceramics such as $\text{Pb}(\text{Zr}_{0.52}\text{Ti}_{0.48})\text{O}_3$ (PZT), $\text{Pb}(\text{Mg}_{1/3}\text{Nb}_{2/3})\text{O}_3-\text{PbTiO}_3$ (PMN-PT), and $(\text{Pb},\text{La})(\text{Zr},\text{Ti})\text{O}_3$ (PLZT) are widely implemented in electronic and electric devices as actuators, sensors, and microelectronic devices due to their superior electrical properties [3,125]. However, lead with high toxicity brings harmful effects on the environment and human [4]. Therefore, waste electrical and electronic equipment (WEEE), restrictions on hazardous substances (RoHS), and end-of-life vehicles (ELV)

were established to prevent pollutants. Therefore, replacement of lead-based materials with lead-free ones is an important issue in piezoceramics. Several kinds of lead-free piezoceramics have been extensively investigated, such as BaTiO₃ [5,6,176], (Bi_{1/2}Na_{1/2})TiO₃ [7,8,37], and (K_{0.5}Na_{0.5})NbO₃ (KNN) [9,10].

Among them, K_{0.5}Na_{0.5}NbO₃ (KNN) and its compounds have been considered as one of promising candidates because of their excellent dielectric and piezoelectric properties. Pure KNN ceramics have orthorhombic (O)–tetragonal (T) phase transition temperature T_{O-T} around 200°C, and T–cubic (C) phase transition temperature (or Curie temperature) T_C around 420°C [87,177]. Many studies have been carried out to improve the properties for KNN-based materials by introducing the concept of polymorphic phase transition (PPT) [12]. The piezoelectric properties can be well improved when the compositions approach the PPT boundaries, based on the polarization rotation and polarization extension. However, those compositions exhibit the temperature sensitive problem since the PPT in KNN depend on not only compositions but also temperatures [134,178]. One of solutions to overcome this problem is the concept of morphotropic phase boundary (MPB), a nearly vertical phase boundary separating rhombohedral, tetragonal... phases and nearly temperature independent.

The MPB, especially R–T MPB, plays a very important role in PZT ceramics because of the excellent piezoelectric and dielectric properties [13,107-109]. Composition of Pb(Zr_{0.52}Ti_{0.48})O₃ exhibits a very high piezoelectric response and electromechanical coupling coefficients, as a result of enhanced polarizability arising from the domain wall mobility [110] at MPB. In KNN-based materials, many studies mentioned about R–T MPB with excellent properties and good thermal stability [14,60,112]. The main way of forming those MPB was the shifting of diffused R–O and O–T phase transition closer by chemical modification to create a partially overlapped phase transition over a broad

temperature range. Another approximation is making the composites by using two end members, one with tetragonal symmetry and the other with rhombohedral symmetry at room temperature [25]. For tetragonal phase stabilization, it is reported that some chemical modifications were applied on pure KNN, such as Li_2CO_3 [46], BiScO_3 [41], MTiO_3 (with $M = \text{Pb, Ba, Sr, Ca, Bi}_{0.5}\text{Li}_{0.5}\dots$) [42,43], LiMeO_3 (with $\text{Me} = \text{Nb, Ta, Sb}\dots$) [44-46]. Other additives have been used to bring the $T_{\text{R-O}}$ of KNN from -123°C to above room temperature, such as AZrO_3 ($A = \text{Ba, Ca, Sr}\dots$) [47,48], Sb^{5+} [49,50], BiScO_3 [51].

Even though most studies claimed that the R phase in KNN ceramics can be stabilized by BaZrO_3 modification, the definition of stabilized phases is still controversial. In fact, it is difficult to clarify the crystal structure using XRD patterns at (200) peak only since either rhombohedral or pseudocubic (PC) shows the single (h00) peaks. However, a rhombohedral symmetry ($\alpha = \beta = \gamma \neq 90^\circ$) indicates the split peaks at (hh0) and (hhh) reflections [1,152], while pseudocubic symmetry are reflected as single peaks based on the perpendicularity. Moreover, some studies have recently suggested stabilization of a relaxor based on the phase transition from noncubic phases to pseudocubic phases [68-73,179]. The relaxor behaviors in KNN-based ceramics can be considered as some features, such as the extremely broad maximum in temperature dependent permittivity, diffuse phase transitions, and Vogel-Fulcher relaxations [74]. By considering the XRD pattern at (110) peaks and investigating the relaxor features in BaZrO_3 -modified KNN, Duong *et. al.* [124] suggested that stabilized phase was pseudocubic. Therefore, several R-T MPBs should be review as new PC-T phase boundary.

Actually, the MPB behaviors for tetragonal and pseudocubic phase have been mentioned in lead-based [83,84] and lead-free piezoceramics [71,85,86], based on the ferroelectric-relaxor phase transition. The enhancement of piezoelectric constant and/or electromechanical strain can be observed; however, the temperature stability of

piezoelectric properties was not mentioned. Otherwise, since the materials in those studies were synthesized by solid solution method, the formation and contribution of each component in the phase coexistence are still ambiguous. One again, the composite method is considered as a promising solution. The calcined powders of two end members for tetragonal and pseudocubic symmetry at room temperature can be mixed with different ratios. In this study, we selected the composition of $0.96(\text{K}_{0.5}\text{Na}_{0.5})_{0.96}\text{Li}_{0.04}\text{NbO}_3 - 0.04\text{SrTiO}_3$ (KNN-4ST-4L) as tetragonal and $0.92\text{Na}_{0.5}\text{K}_{0.5}\text{NbO}_3 - 0.08\text{BaZrO}_3$ (KNN-8BZ) as pseudocubic phase. The composites are indicated by the fraction f of T-phase content. The temperature dependent dielectric properties, high temperature X-ray diffraction patterns and temperature stability of piezoelectric constant d_{33} were investigated to emphasize the existence of new morphotropic phase boundary. Moreover, the microstructure, ferroelectric properties, piezoresponse force microscopy mappings were studied as well.

4.5.2. Results and discussions

Figure 4.27 shows the polished and thermally etched surface images of KNN-based composites, with different T-phase fraction f . The relative densities of all samples were calculated from the measured density and the unit cell volume determined by XRD. Both end components have high relative density around 96%, with very small amounts of holes and abnormal grain distributions. However, the relative density slightly decreases to 95%–95.5% for the composites. 10 mol% of T-phase sample exhibits the strong abnormal grain growth, which may be related to the preferential segregation of T-phase seed with small amount as impurities [180] or different particle size distribution [181]. When the seed fraction further increases, the anisotropic grain-boundary energies [182]

can be reduced and the grain structures become more uniform. The average grain size firstly increases and reaches the largest grains for $f = 0.7$, then decreases.

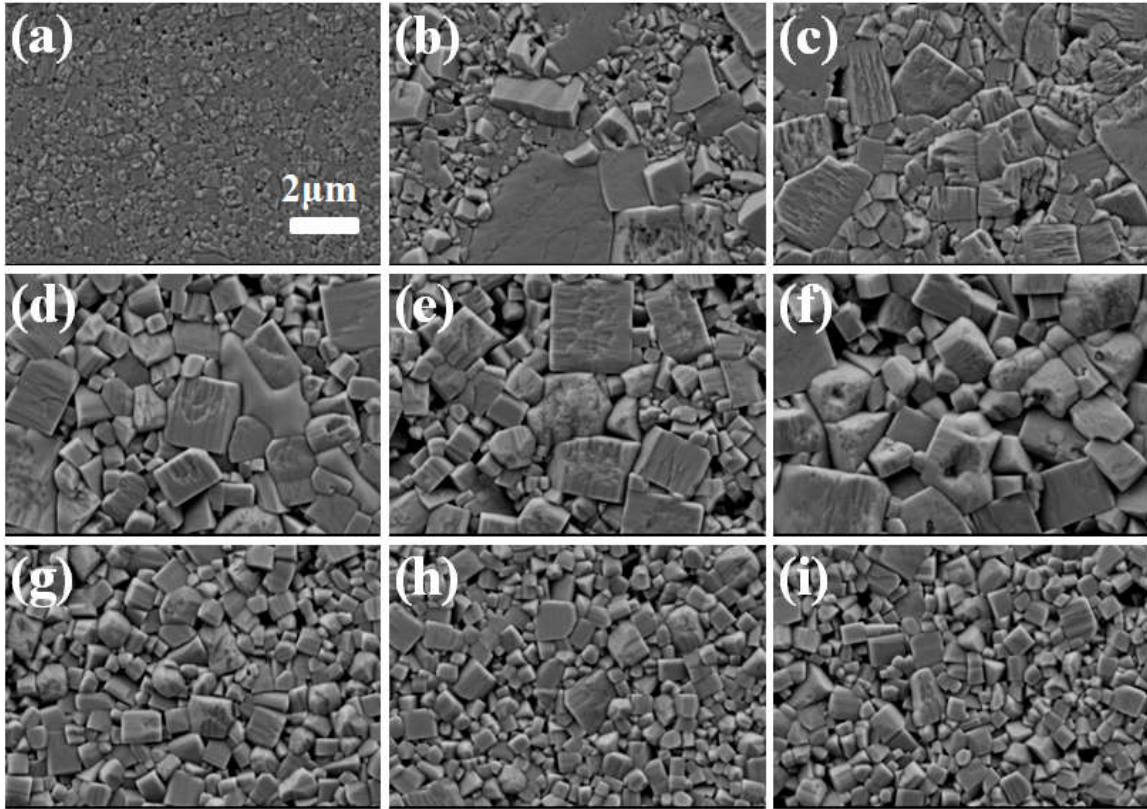


Figure 4.27. The polished and thermally etched surface images of KNN-based composites, with different T-phase fraction: (a) $f = 0$, (b) $f = 0.1$, (c) $f = 0.3$, (d) $f = 0.5$, (e) $f = 0.06$, (f) $f = 0.7$, (g) $f = 0.8$, (h) $f = 0.9$, and (i) $f = 1$.

The X-ray diffraction patterns for KNN-based composites as a function of T-phase fraction are depicted in Figure 4.28. A single perovskite structure without any secondary phases in all samples indicates that all composites were stably synthesized. The peaks in 2θ range of 44.5° – 46.2° are displaced in Figure 28 (b) to clarify the changes in crystal structure for all compositions. It was clearly reported in the Section 4.3 that the

KNN-4ST-4L (or $f = 1$) ceramics performed a single tetragonal structure, corresponding with two distinct peaks as $(002)_T$ and $(200)_T$. Meanwhile, the pseudocubic phase was observed in Section 4.4 for KNN-8BZ (or $f = 1$) ceramics with single (110) and (200) reflections [124]. For the composites with the increase of T-phase fraction, the crystal structure is gradually transformed from PC phase to T phase. As an advantage of composite method, these two phases are believed to be coexisted in the composites at different contribution ratios.

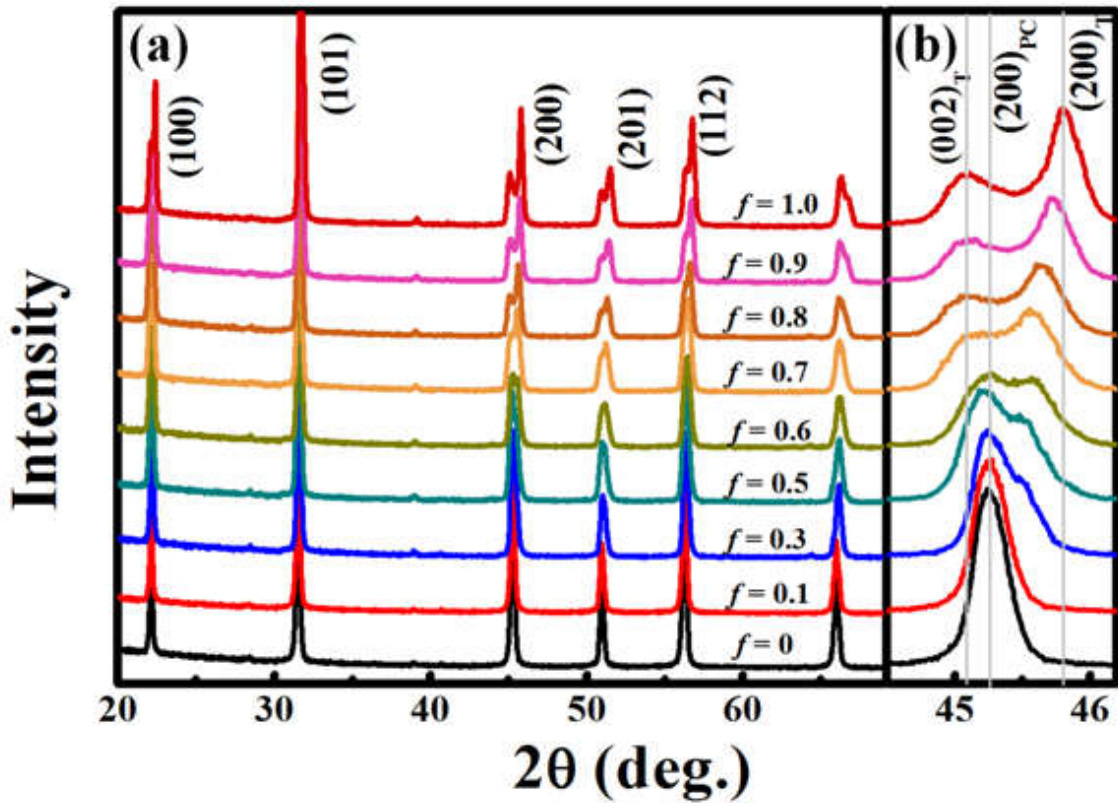


Figure 4.28. X-ray diffraction patterns of KNN-based composites in the 2θ ranges of (a) 20° – 70° , (b) 44.5° .

Figure 4.29 (a) shows dielectric constant (ϵ_r) for all KNN-based composites as a function of temperature. The detected Curie temperature (T_C) and pseudocubic–tetragonal

phase transition temperatures (T_{PC-T}) are provided in Figure 4.29 (b). It is well noted that T_C values for KNN–8BZ and KNN–4ST–4L are around 205°C and 340°C, respectively. When the contribution of KNN–4ST–4L increases, T_C values for composites monotonically increase as well. KNN–8BZ was considered as the composition at ferroelectric–to–relaxor crossover with PC phase. An abnormal peak can be observed for $f = 0.3$ composites around 100°C, then shifted to lower temperature for $f = 0.5$ and 0.6 composites, and finally detected near room temperature (RT) for $f = 0.7$ composites. There are no abnormal peaks on ϵ_r for $f = 0.8, 0.9$ and 1.0 composites between RT and T_C . This implies that those samples were stabilized as a tetragonal phase. Actually, the PC phase can be existed in $f = 0.8, 0.9$ composites, but with small ratios and relatively weak compared with T phase.

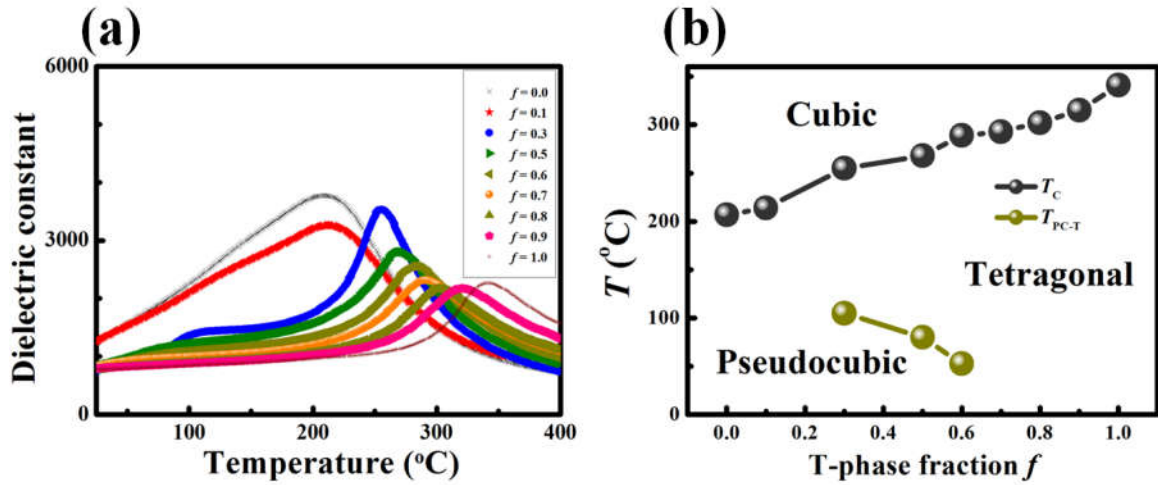


Figure 4.29. (a) Temperature–dependent dielectric constant (ϵ_r) for all KNN–based composites at 100 kHz. (b) Phase transition temperatures.

Figure 4.30 shows the electric–field–induced strain ($S-E$) and polarization ($P-E$) curves for KNN–based composites under an electric field of 4kV/mm and the extracted values. It

is believed that the relaxor features in KNN–8BZ ceramics is revealed, while KNN–4ST–4L performs the relaxor–like ferroelectric behaviors. Interestingly, both S – E and P – E curves of $f = 0.1$ composites show strongest ferroelectricity, which may be related with the abnormal grain growth behaviors of these samples in Figure 4.27. From $f = 0.1$ to $f = 1$ composites, the maximum polarization P_m and remnant polarization P_r monotonically decrease, while the coercive field E_c increases. The negative strain S_{neg} values are small for single phase ceramics, and then gradually increase when the fraction approaches 0.5. The maximum strain S_{max} values are enhanced for $f = 0.5$ – 0.7 composites, with highest value is obtained at $f = 0.7$. These results are strongly related to the coexistence of PC and T phases, as well as the coexistence of relaxor and ferroelectric.

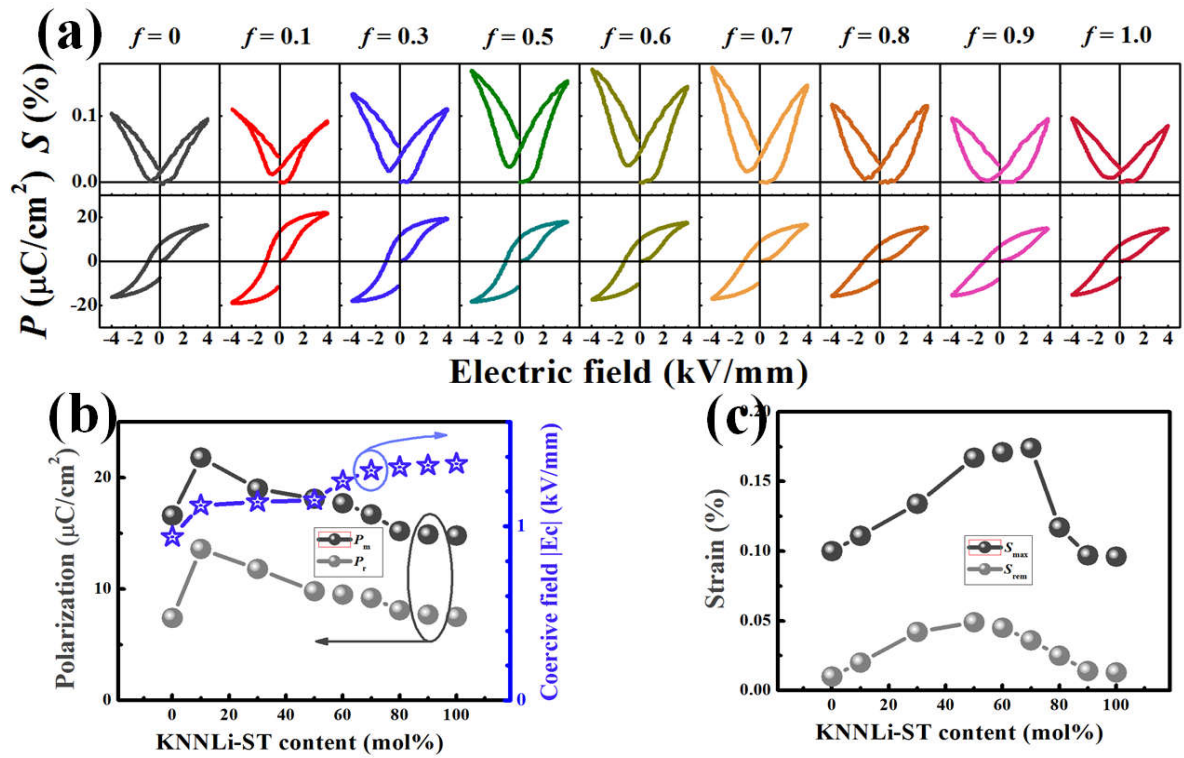


Figure 4.30. (a) Electric–field–induced strain and polarization curves for KNN–based composites and (b, c) extracted values.

Figure 4.31 provides the values of piezoelectric constant (d_{33}), mechanical quality factor (Q_m), and electromechanical coupling factor (k_p) for KNN-based composites as a function of T-phase fraction. With increasing T-phase content, both d_{33} and k_p slightly increase, culminate in the highest values of 210 pC/N and 35% at $f=0.7$ composites, then decrease. It is suggested that the enhancement of piezoelectric properties comes from the coexistence of tetragonal and pseudocubic phases in these KNN-based composites. In addition, the optimum ratio for composites can be considered as 70 mol% of T-phase and 30 mol% of PC-phase. On the other hand, the trend of Q_m is more complicated. It seems to be improved for both PC- and T-rich phase composites, in a comparison with single compositions or near 50/50 composites. This behavior may be related with the microstructure, which was described in Figure 4.27.

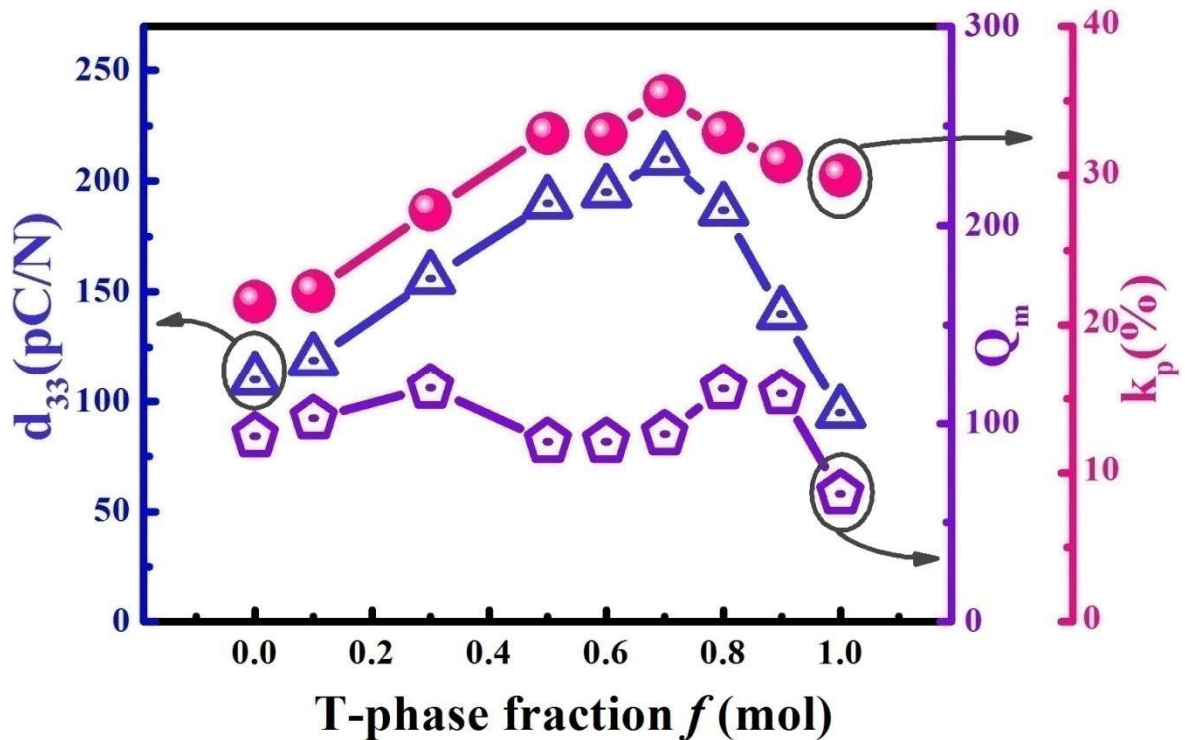


Figure 4.31. Piezoelectric constant (d_{33}), mechanical quality factor (Q_m), and electromechanical coupling factor (k_p) for KNN-based composites.

To clarify the crystal structures and phase transition behaviors, the temperature-dependent XRD patterns in the 2θ range of 44.4° – 46.4° for $f = 0, 0.3, 0.7$ and 1.0 composites are shown in Figure 4.32. In $f = 0$ ceramics, the PC phase with single (200) peaks can be observed from RT to 150°C , and then the cubic (C) phase is detected for temperature above 200°C . The single peak with small shoulder on right side in room temperature XRD pattern for $f = 0.3$ composites indicates that both PC- and T-phase are already coexisted in this material, in which the PC-phase is still dominant. When the temperature increases, T-phase becomes more stable and contribute more into crystal structure. As a result, the XRD patterns in temperature range of 100°C – 200°C shows the coexistence of PC- and T-phase with a relative distribution. When temperature is higher than 250°C , C-phase is observed. In case of $f = 0.7$ composites, it seems that both PC- and T-phase offer the comparable contribution at RT. This can be a reason for the highest d_{33} value in these composites. With increasing temperature, T-phase become more dominant above 100°C , and C-phase is found from 300°C . The peak at 250°C can be considered as the T-C phase transition. For $f = 1$ ceramics, single T-phase is obviously performed from RT up to 300°C , then transforms to C-phase at 350°C .

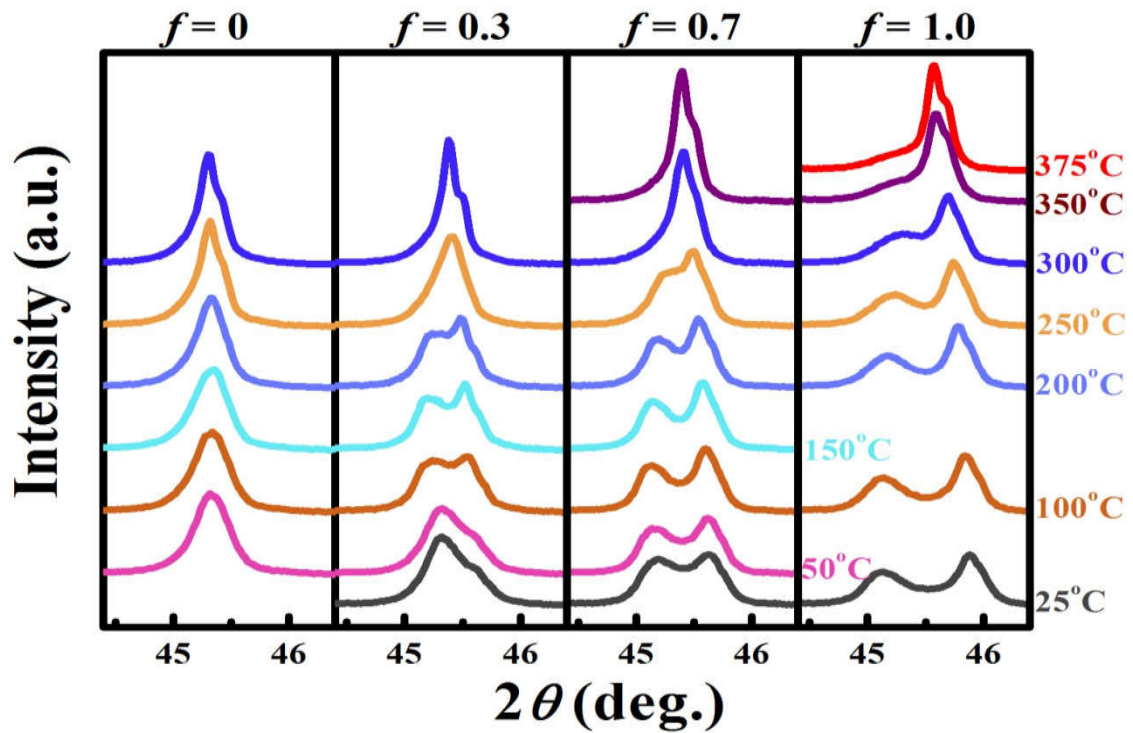


Figure 4.32. High temperature X-ray diffraction patterns of KNN-based composites in the 2θ range of 44.4° – 46.4° .

The temperature-dependent piezoelectric constant d_{33} in the relationship with temperature-dependent dielectric constant ϵ_r for KNN-based composites are shown in Figure 4.33. The samples were annealed for 5 minutes at different temperature steps from room temperature to 350°C , with the increasing step increment of 25°C , to check the temperature stability of the piezoelectric constant d_{33} . Interestingly, the obtained results are well-matched with temperature-dependent XRD patterns in Figure 4.32. Particularly, the gradually decreasing of d_{33} values reveal the relatively sensitive temperature dependence for $f = 0$ ceramics in Figure 4.33 (a), based on PC phase. In Figure 4.33 (b), d_{33} values $f = 0.3$ composites present three regions: (i) stable $\sim 150\text{pC/N}$ (RT– 100°C), corresponds with PC-rich phase coexistence; (ii) stable $\sim 125\text{pC/N}$ (150°C – 225°C), PC–T phase coexistence; and (iii) vanishing ($\geq 250^\circ\text{C}$), C-phase. On the other hand, we could

obtain the highest d_{33} with comparatively good temperature stability (Δd_{33} less than $\pm 10\%$) for $f = 0.7$ composites in Figure 4.33 (c). These behaviors may be related to the coexistence of T and PC phases (RT–100°C) and the stabilization of single T phase [57,96,106] (100°C–200°C). In addition, d_{33} values for $f = 1$ ceramics in Figure 4.33(d) is quite stable from RT up to near T_C , based on the T phase.

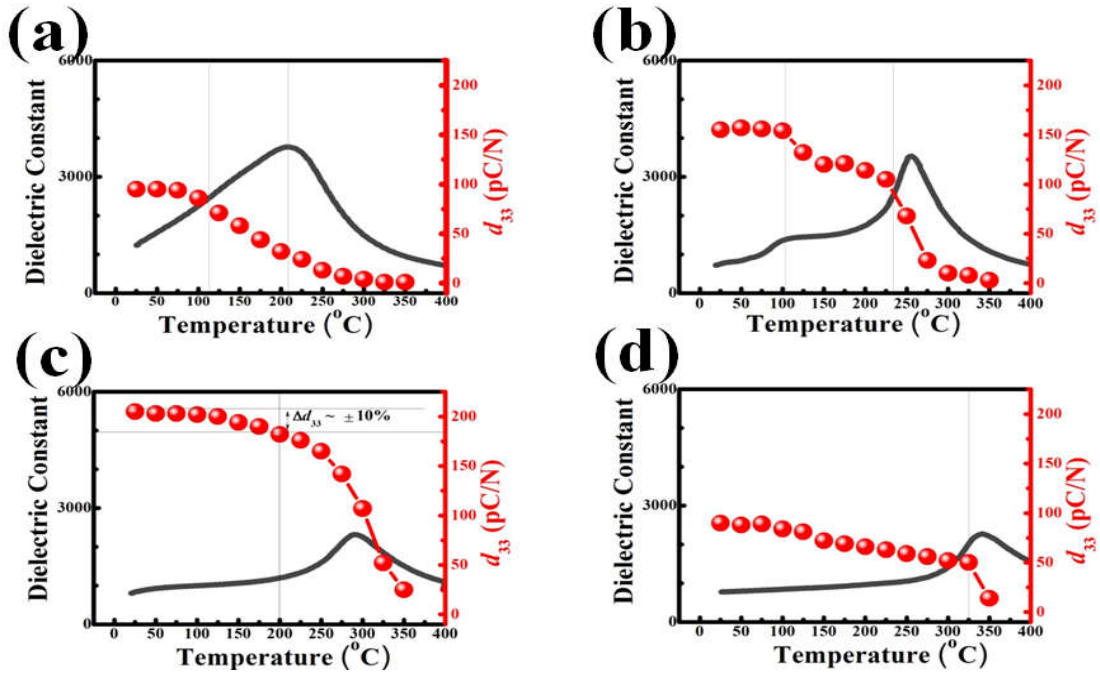


Figure 4.33. Temperature–dependent dielectric constant and d_{33} behavior for KNN–based composites with different T–phase fraction: (a) $f = 0$, (b) $f = 0.3$, (c) $f = 0.7$ and (d) $f = 1$.

The piezoresponse force microscope (PFM) amplitude and phase mappings on $2.0 \mu\text{m} \times 3.0 \mu\text{m}$ area for $f = 0$, $f = 0.7$, and $f = 1$ composites are given in Figure 4.34. The amplitude mappings in upper row describe the respond in displacement of the samples under measuring process, which provides obvious information relating with strain properties. It is clearly observed that $f = 1$ sample in Figure 4.34 (c1) shows the lowest displacement with the dominant parts around 20 pm. For $f = 0$ sample in Figure 4.34 (a1),

the area of 100 pm is quite prevailed. Meanwhile, $f = 0.7$ composites sample in Figure 4.34 (b1) performs the broader range of amplitude, with the highest displacement up to 160pm. This may offer the enhancement in maximum strain behaviors. On the other hand, the phase mappings in lower row give us the visual information about domain structure, and provide the evidence for the behaviors of polarization and piezoelectric constant.

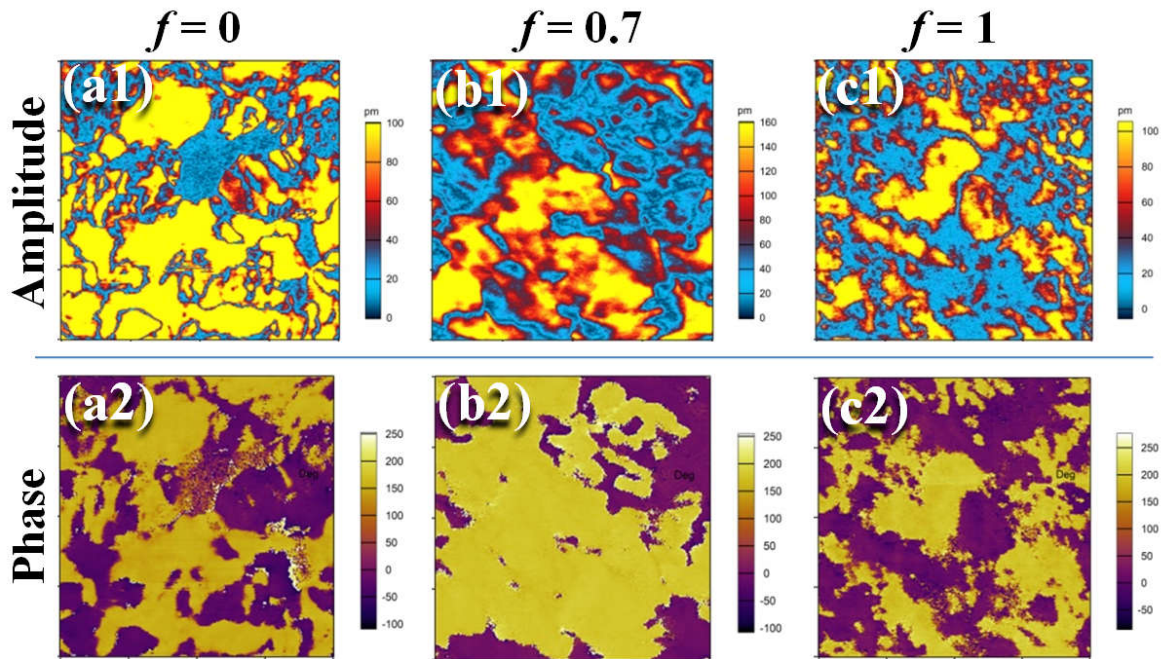


Figure 4.34. PFM mappings of KNN-based composites on $2.0 \mu\text{m} \times 3.0 \mu\text{m}$ area. (a1) and (a2) $f = 0$, (b1) and (b2) $f = 0.7$, (c1) and (c2) $f = 1$ composites.

Figure 4.35 shows the proposed model for three different states of $f = 0$, $f = 0.7$, and $f = 1$ composites to explain the behaviors of electromechanical strain and polarization properties. Three different domain structures are suggested in this schematic diagram: ferroelectric domains (FDs), polar nanoregions (PNRs) [169], and tetragonal micro-domains (TMDs) [183]. In Figure 4.35 (a), $f = 0$ ceramics are determined as ferroelectric-to-relaxor crossover stage with coexistence of the polarized FDs and PNRs.

At the initial state (i), a macroscopically zero polarization can be obtained for all samples since the domains and regions are organized in a random configuration. Under an external electric field, the coexisted FDs and PNRs are sequentially reoriented to the applied electric field direction, in which PNRs is able to support domain switching as an “accelerator” [175]. At state (iii) where $E = 0$, while the aligned FDs can be maintained in the poling direction, PNRs quickly transit back to the initial state and reduce the stable of those FDs remnant polarization. Therefore, the low E_c with relatively small S_{rem} and high S_{pol} ($> 0.1\%$) can be observed in KNN–8BZ ceramics.

Figure 4.35 (c) shows the status for $f = 1$ ceramics with the TMDs, a transition between tetragonal macro–domains and cubic structure in ferroelectric materials [183-185]. In this model, TMDs are described with separated rectangular domains on non–polar matrix, and own a relatively low domain wall energy [186]. When the electric field is applied, the reorientation for TMDs along the field direction is quite similar to the domain switching process [172] for FDs, but easier. However, it is difficult to completely induce these domains across the macroscopic polarization, based on the disruption. Thus, the P_{max} and S_{max} values for this composition are small regardless of the ferroelectricity.

In Figure 4.35 (b), all three structures of FDs, PNRs and TMDs are coexisted in $f = 0.7$ composites. It is suggested that the presence of PNRs will firstly support on TMDs with lower domain wall energy, and then all of these domains are aligned with the electric field, resulting in the high saturated polarization. When the external field is removed, PNRs quickly transition back to the initial state while the polarized FDs and TMDs can be maintained.

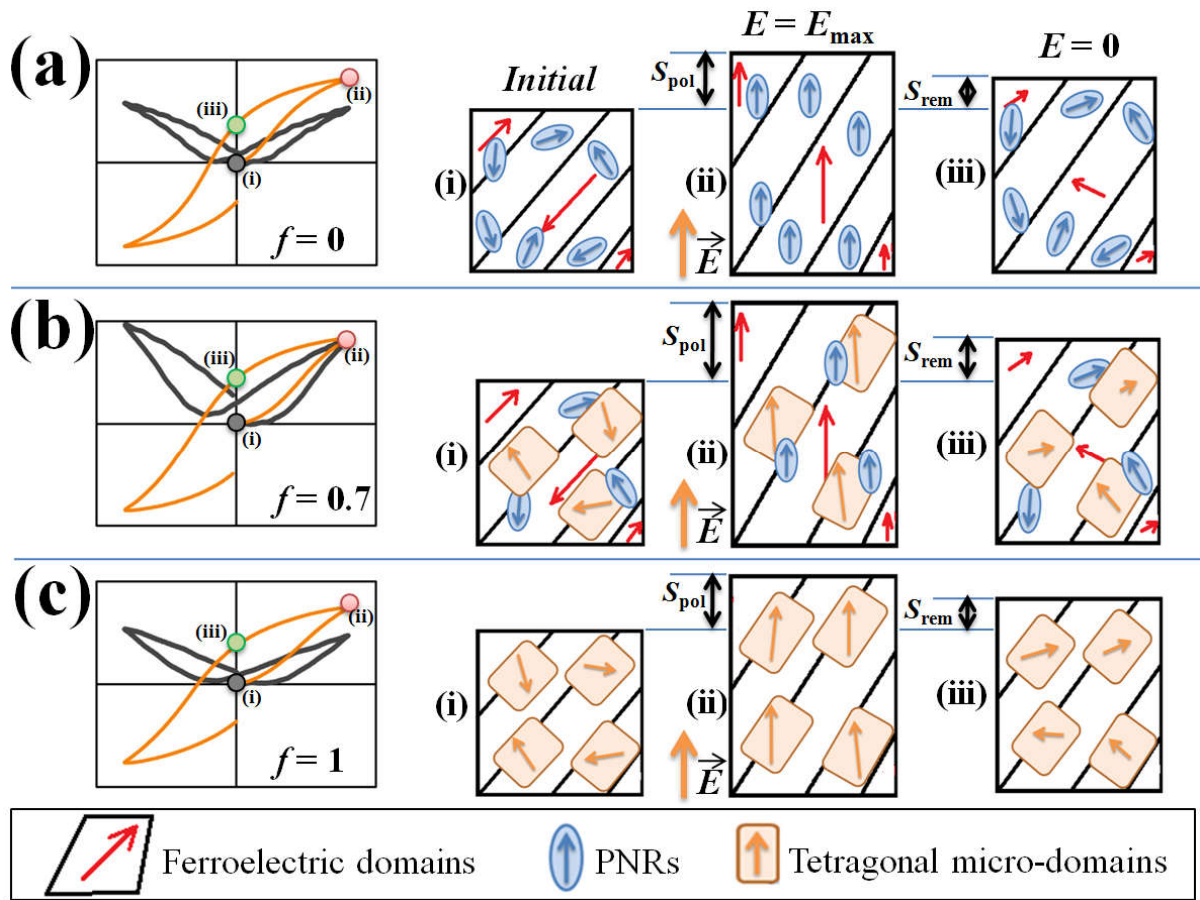


Figure 4.35. Schematic diagram for the three different states of (a) $f = 0$, (b) $f = 0.7$, and (c) $f = 1$ composites.

4.5.3. Conclusion

The calcined powders of two end members for tetragonal and pseudocubic symmetry at room temperature can be mixed with different tetragonal contribution fraction f . The temperature dependent dielectric properties, high temperature X-ray diffraction patterns and temperature stability of piezoelectric constant d_{33} were investigated to emphasize the existence of new morphotropic phase boundary. Moreover, the microstructure, ferroelectric properties, piezoresponse force microscopy mappings were studied as well. As a result, the enhanced strain properties at $f = 0.7$ composites are related with the

coexistence of FDs, TMDs and PNRs, originating from the relatively contribution of the ferroelectric and relaxor components in composites. Moreover, the new T-PC phase boundary can be observed in composites with T-phase fraction $f = 0.7$, with the enhancement of d_{33} and its good temperature stability.

Chapter 5: Summary

The work described in this thesis presented the detailed study on forming the new phase boundary in lead-free KNN-based piezoelectric materials. All of the experiments and research results are systematically described and discussed in Chapter 4 with consistent direction.

An example of rhombohedral-tetragonal morphotropic phase boundary (R-T MPB) in KNN-BLT-100xBZ ceramics was performed in section 4.1. The MPB in $x = 0.06$ composition was identified by the room temperature XRD, high temperature XRD, temperature dependent dielectric properties, with the enhancement and thermal stability of piezoelectric constant d_{33} . The compositions were synthesized by conventional solid solution, using $\text{Bi}_{0.5}\text{Li}_{0.5}\text{TiO}_3$ and BaZrO_3 modification on KNN materials to control the R-O and O-T phase transition temperature. As mentioned in several references, BaZrO_3 was believed to stabilize the rhombohedral phase in KNN ceramics.

In order to separate and clarify the components in phase coexistence, the main idea of this work was forming an MPB on KNN-based ceramics by using the calcined powders of two end members (one with tetragonal and the other with rhombohedral symmetry) to create the composites. For tetragonal stabilization, we had firstly chosen SrTiO_3 modification because of its advantages on sinterability and piezoelectric properties of KNN ceramics. As a result, we found the stable single tetragonal phase in KNN-100xST ceramics with $x \geq 0.06$. However, those compositions required high sintering temperature T_s (above 1200°C) to obtain dense sample, and their Curie temperature T_C also significantly decreases (under 290°C). To overcome these problems, Li_2CO_3 doping was doped on $0.96\text{Na}_{0.5}\text{K}_{0.5}\text{NbO}_3-0.04\text{SrTiO}_3$ ceramics. Finally, we selected $0.96(\text{K}_{0.5}\text{Na}_{0.5})_{0.96}\text{Li}_{0.04}\text{NbO}_3-0.04\text{SrTiO}_3$ (KNN-4ST-4L) as a candidate for tetragonal

phase, with T_s , T_C and d_{33} are 1180°C, 328°C, 165pC/N and 0.33, respectively.

The original purpose of BaZrO₃ modification in KNN ceramics was to stabilize the rhombohedral phase. However, by adding the peaks (110) analysis in XRD and investigating the relaxor features of materials, the stabilized phase in the KNN–100yBZ was confirmed to be a pseudocubic phase. Moreover, a proposed model of ferroelectric domains (FDs) and polar nanoregions (PNRs) was provided to explain the changes of electrical properties in KNN–100yBZ ceramics in the relationship with stabilized relaxor. The ferroelectric-to-relaxor crossover was found at KNN–8BZ ceramics, in which the significantly decreased E_c with relatively small S_{neg} and enhanced S_{max} may originate from the existence of PNRs with FDs. End of this stage, KNN–8BZ was chosen to be the remaining component with pseudocubic phase.

Therefore, the composites in Section 4.5 were formed by mixing the tetragonal KNN–4ST–4L and the pseudocubic KNN–8BZ, with different T-phase fraction f . As an advantage of composite method, these two phases are believed to be coexisted in the composites at different contribution ratios. The optimum ratio can be considered for 70 mol% of T-phase (30 mol% of PC-phase) composites, with the highest d_{33} values of 210 pC/N comparatively good temperature stability (Δd_{33} less than $\pm 10\%$). The high temperature XRD pattern for $f = 0.7$ composites indicated that both PC- and T-phases coexisted in this materials from RT up to near T_C . In this temperature range, the contribution of those phases seems to be equivalent near RT, and the T-phase become more dominant at higher temperature. Interestingly, the enhancement of electromechanical strain behaviors was also observed in $f = 0.7$ composites, which may originate from the complicated existence of ferroelectric polarization with micro domains in tetragonal phase and PNRs in pseudocubic phase. The schematic diagram for these domain structures was introduced as well.

We had successfully fabricated the lead-free KNN-based ferroelectric/relaxor piezoelectric composites with new phase boundary. The currently developed materials showed not only highly temperature-insensitive piezoelectric constant d_{33} but also improved electromechanical strain, which is highly promising for both sensor and actuator applications. However, the values of d_{33} in our materials still need to be enhanced, and the mechanism of ferroelectric behaviors for all composites requires further analysis.

References

1. R. Guo, L.E. Cross, S.E. Park, B. Noheda, D.E. Cox, G. Shirane, *Phys. Rev. Lett.* **84**, 5423-5426 (2000).
2. M.S. Islam, J. Beamish, *J. Appl. Phys.* **126**, 204101 (2019).
3. A. Kuma, A.K. Kalyani, R. Ranjan, K.C.J. Raju, J. Ryu, N. Park, A.R. James, *J. Alloys Compd.* **816**, 152613 (2020).
4. A.J. Bell, O. Deubzer, *MRS Bull.* **43**, 581-587 (2018).
5. J. Wu, D. Xiao, W. Wu, Q. Chen, J. Zhu, Z. Yang, J. Wang, *Scr. Mater.* **65**, 771-774 (2011).
6. M. Arshad, H. Du, M. Javed, A. Maqsood, I. Ashraf, H. Sussain, W. Ma, H. Ran, *Ceram. Int.* **46**, 2238-2246 (2020).
7. T.A. Duong, H.S. Han, Y.H. Hong, Y.S. Park, H.T.K. Nguyen, T.H. Dinh, J.S. Lee, *J. Electroceram.* **41**, 73-79 (2018).
8. G. Wang, Y.H. Hong, H.T.K. Nguyen, B.W. Kim, C.H. Ahn, H.S. Han, J.S. Lee, *Sens. Actuator A Phys.* **293**, 1-6 (2019).
9. J. Wu, D. Xiao, J. Zhu, *Chem. Rev.* **115**, 2559-2595 (2015).
10. H. Shi, J. Chen, R. Wang, S. Dong, *J. Alloys Compd.* **655**, 290-295 (2016).
11. H.-C. Thong, C. Zhao, Z. Zhou, C.-F. Wu, Y.-X. Liu, Z.-Z. Du, J.-F. Li, W. Gong, K. Wang, *Mater. Today* **29**, 37-48 (2019).
12. J.F. Li, K. Wang, F.Y. Zhu, L.Q. Cheng, F.Z. Yao, D.J. Green, *J. Am. Ceram. Soc.* **96**, 3677-3696 (2013).
13. B. Jaffe, R.S. Roth, S. Marzullo, *J. Appl. Phys.* **25**, 809-810 (1954).
14. Q. Liu, J.-F. Li, L. Zhao, Y. Zhang, J. Gao, W. Sun, K. Wang, L. Li, *J. Mater. Chem. C.* **6**, 1116-1125 (2018).
15. N.M. Hagh, B. Jadidian, E. Ashbahian, A. Safari, *IEEE Trans. Ultrason. Ferroelectr. Freq. Control.* **55**, 214-24 (2008).
16. S. Mishra, L. Unnikrishnan, S.K. Nayak, S. Mohanty, *Macromol. Mater. Eng.* **304**, 1800463 (2019).
17. D. Damjanovic, *Rep. Prog. Phys.* **61**, 1267-1324 (1998).
18. R.R. Mehta, B.D. Silverman, J.T. Jacobs, *J. Appl. Phys.* **44**, 3379-3385 (1973).
19. K. Matsuura, Y. Cho, R. Ramesh, *Appl. Phys. Lett.* **83**, 2650-2652 (2003).
20. I.W. Chen, Y.Q. Wang, *Ferroelectrics.* **206**, 245-263 (1998).

21. M. Acosta, N. Novak, V. Rojas, S. Patel, R. Vaish, J. Koruza, G.A. Rossetti, J. Rödel, *Appl. Phys. Rev.* **4**, 041305 (2017).
22. A. Safari, R.K. Panda, V.F. Janas, *Key Eng. Mater.* **122-124**, 35-70 (1996).
23. G. Shirane, K. Suzuki, A. Takeda, *J. Phys. Soc. Jpn.* **7**, 12-18 (1952).
24. J. Caceres, C. Passos, J. Chagas, R. Barbieri, R. Corteletti, *Mater. Res.* **22**, 20190123 (2019).
25. B. Jaffe, W.R. Cook, H. Jaffe, *Piezoelectric ceramics*, **Vol.5**, (1971).
26. T.B. Weston, A.H. Webster, V.M. Mcnamara, *J. Am. Ceram. Soc.* **52**, 253–257
27. H. Banno, T. Tsunooka, 1967 *Jpn. J. Appl. Phys.* **6**, 954-962 (1967).
28. G. Smolenskii, V. Isupov, *Sov. Phys. Solid State.* **2**, 2584-2594 (1961).
29. L. Cross, *Ferroelectrics.* **76**, 241-267 (1987).
30. S. Swartz, T. Shrout, W. Schulze, L. Cross, *J. Am. Ceram. Soc.* **67**, 311-314 (1984).
31. G.H. Haertling, *J. Am. Ceram. Soc.* **82**, 797–818 (1999).
32. X. Dai, Z. Xu, J. Li, D. Viehland, *J. Mater. Res.* **11**, 626-638 (1995).
33. E. Aksel, J.L. Jones, *Sensors.* **10**, 1935-1954 (2010).
34. W. Liu, X. Ren, *Phys Rev Lett.* **103**, 257602 (2009).
35. D.S. Keeble, F. Benabdallah, P.A. Thomas, M. Maglione, J. Kreisel, *Appl. Phys. Lett.* **102**, (2013).
36. K. Reichmann, A. Feteira, M. Li, *Mater.* **8**, 8467-8495 (2015).
37. X. Wang, H.L.W. Chan, C.L. Choy, *J. Am. Ceram. Soc.* **86**, 1809–1811 (2003).
38. B. Malic, J. Koruza, J. Hrescak, J. Bernard, K. Wang, J.G. Fisher, A. Bencan, *Mater.* **8**, 8117-8146 (2015).
39. S.O. Leontsev, R.E. Eitel, *Sci. Technol. Adv. Mater.* **11**, 044302 (2010).
40. K. Tanaka, H. Hayashi, K.-i. Kakimoto, H. Ohsato, T. Iijima, *Jpn. J. Appl. Phys.* **46**, 6964-6970 (2007).
41. H. Du, W. Zhou, F. Luo, D. Zhu, S. Qu, Y. Li, Z. Pei, *J. Appl. Phys.* **104**, (2008).
42. R. Wang, H. Bando, M. Itoh, *Appl. Phys. Lett.* **95**, (2009).
43. D. Lin, K.W. Kwok, H.L.W. Chan, *J. Appl. Phys.* **102**, (2007).
44. N. Klein, E. Hollenstein, D. Damjanovic, H.J. Trodahl, N. Setter, M. Kuball, *J. Appl. Phys.* **102**, (2007).
45. D. Lin, K.W. Kwok, K.H. Lam, H.L.W. Chan, *J. Appl. Phys.* **101**, (2007).
46. Y. Guo, K.-i. Kakimoto, H. Ohsato, *Mater. Lett.* **59**, 241-244 (2005).

47. R. Wang, H. Bando, T. Katsumata, Y. Inaguma, H. Taniguchi, M. Itoh, *physica status solidi (RRL) - Rapid Res. Lett.* **3**, 142-144 (2009).
48. R. Wang, H. Bando, M. Kidate, Y. Nishihara, M. Itoh, *Jpn. J. Appl. Phys.* **50**, (2011).
49. R. Zuo, J. Fu, D. Lv, Y. Liu, *J. Am. Ceram. Soc.* **93**, 2783-2787 (2010).
50. I.H. Chan, C.-T. Sun, M.-P. Houg, S.-Y. Chu, *Ceram. Int.* **37**, 2061-2068 (2011).
51. X. Sun, J. Chen, R. Yu, C. Sun, G. Liu, X. Xing, L. Qiao, *J. Am. Ceram. Soc.* **92**, 130-132 (2009).
52. R. Wang, R.-J. Xie, K. Hanada, K. Matsusaki, H. Bando, M. Itoh, *Phys. Status Solidi (A)*. **202**, R57-R59 (2005).
53. E. Hollenstein, M. Davis, D. Damjanovic, N. Setter, *Appl. Phys. Lett.* **87**, (2005).
54. G.-Z. Zang, J.-F. Wang, H.-C. Chen, W.-B. Su, C.-M. Wang, P. Qi, B.-Q. Ming, J. Du, L.-M. Zheng, S. Zhang, T.R. Shrout, *Appl. Phys. Lett.* **88**, (2006).
55. R. Zuo, X. Fang, C. Ye, *Appl. Phys. Lett.* **90**, (2007).
56. W. Liang, W. Wu, D. Xiao, J. Zhu, S. Zhang, *J. Am. Ceram. Soc.* **94**, 4317-4322 (2011).
57. R. Zuo, C. Ye, X. Fang, *Jpn. J. Appl. Phys.* **46**, 6733-6736 (2007).
58. X. Wang, J. Wu, D. Xiao, J. Zhu, X. Cheng, T. Zheng, B. Zhang, X. Lou, X. Wang, *J. Am. Chem. Soc.* **136**, 2905-10 (2014).
59. K. Xu, J. Li, X. Lv, J. Wu, X. Zhang, D. Xiao, J. Zhu, *Adv Mater.* **28**, 8519-8523 (2016).
60. T. Zheng, H. Wu, Y. Yuan, X. Lv, Q. Li, T. Men, C. Zhao, D. Xiao, J. Wu, K. Wang, J.-F. Li, Y. Gu, J. Zhu, S.J. Pennycook, *Energy Environ. Sci.* **10**, 528-537 (2017).
61. T. Karaki, T. Katayama, K. Yoshida, S. Maruyama, M. Adachi, *Jpn. J. Appl. Phys.* **52**, (2013).
62. T. Takenaka, K.-i. Maruyama, K. Sakata, *Jpn. J. Appl. Phys.* **30**, (1991).
63. X. Lv, J. Zhu, D. Xiao, X.X. Zhang, J. Wu, *Chem. Soc. Rev.* **49**, 671-707 (2020).
64. Y.G. Lv, C.L. Wang, J.L. Zhang, L. Wu, M.L. Zhao, J.P. Xu, *Mater. Res. Bull.* **44**, 284-287 (2009).
65. Y. Yuan, J. Wu, H. Tao, X. Lv, X. Wang, X. Lou, *J. Appl. Phys.* **117**, (2015).
66. H. Du, W. Zhou, D. Zhu, L. Fa, S. Qu, Y. Li, Z. Pei, *J. Am. Ceram. Soc.* **91**, 2903-2909 (2008).
67. F. Li, S. Zhang, D. Damjanovic, L.Q. Chen, T.R. Shrout, *Adv. Func. Mater.* **28**, (2018).
68. S.W. Zhang, H. Zhang, B.P. Zhang, S. Yang, *J. Alloys Compd.* **506**, (2010).
69. J.U. Rahman, A. Hussain, A. Maqbool, T.K. Song, W.J. Kim, S.S. Kim, M.H. Kim, *Curr.*

- Appl. Phys. **14**, 331-336 (2014).
70. F. Si, B. Tang, Z. Fang, H. Li, S. Zhang, *Ceram. Int.* **45**, 17580-17590 (2019).
 71. Y. Wei, N. Zhang, C. Jin, W. Zhu, Y. Zeng, G. Xu, L. Gao, Z. Jian, *J. Am. Ceram. Soc.* **102**, 3598-3608 (2018).
 72. P.D. Gio, T.T. Bau, N.V. Hoai, N.Q. Nam, *J. Mater. Sci. Chem. Eng.* **08**, 1-11 (2020).
 73. X. Zhou, Z. Yan, H. Qi, L. Wang, S. Wang, Y. Wang, C. Jiang, H. Luo, D. Zhang, *J. Eur. Ceram. Soc.* **39**, 2310-2317 (2019).
 74. V.V. Shvartsman, D.C. Lupascu, D.J. Green, *J. Am. Ceram. Soc.* **95**, 1-26 (2012).
 75. Y. Guo, K.-i. Kakimoto, H. Ohsato, *Solid State Commun.* **129**, 279-284 (2004).
 76. M. Kosec, V. Bobnar, M. Hrovat, J. Bernard, B. Malic, J. Holc, *J. Mater. Res.* **19**, 1849-1854 (2004).
 77. V. Bobnar, J. Bernard, M. Kosec, *Appl. Phys. Lett.* **85**, 994-996 (2004).
 78. Y. Guo, K.-i. Kakimoto, H. Ohsato, *Jpn. J. Appl. Phys.* **43**, 6662-6666 (2004).
 79. A.V. Zhirkov, A.S. Sidorkin, E.V. Vorotnikov, A.I. Burkhanov, *Bull. Russian Acad. Sci.: Phys.* **83**, 1122-1124 (2019).
 80. L. Liu, M. Knapp, H. Ehrenberg, L. Fang, H. Fan, L.A. Schmitt, H. Fuess, M. Hoelzel, H. Dammak, M.P. Thi, M. Hinterstein, *J. Eur. Ceram. Soc.* **37**, 1387-1399 (2017).
 81. N.T. U. Nuraini, M. Mashuri, S. Suasmoro, *Mater. Sci. Eng.* **496**, 012043 (2019).
 82. J. Zhou, G. Xiang, J. Shen, H. Zhang, Z. Xu, H. Li, P. Ma, W. Chen, *J. Electroceram.* **44**, 95-103 (2019).
 83. C.H. Wang, *Ceram. Int.* **30**, 605-611 (2004).
 84. T.G. Lee, S.W. Kim, E.J. Kim, S. Jin Lee, H.G. Hwang, Y.W. Hong, J.S. Kim, K.H. Chae, J.W. Choi, C.Y. Kang, S. Nahm, *J. Eur. Ceram. Soc.* **40**, 1947-1956 (2020).
 85. J. Hao, W. Bai, W. Li, B. Shen, J. Zhai, *J. Mater. Res.* **27**, 2943-2955 (2012).
 86. L. Liu, M. Knapp, H. Ehrenberg, L. Fang, L.A. Schmitt, H. Fuess, M. Hoelzel, M. Hinterstein, *J. Appl. Crystallogr.* **49**, 574-584 (2016).
 87. J. Rödel, K.G. Webber, R. Dittmer, W. Jo, M. Kimura, D. Damjanovic, *J. Eur. Ceram. Soc.* **35**, 1659-1681 (2015).
 88. J. Rödel, J.-F. Li, *MRS Bull.* **43**, 576-580 (2018).
 89. A.J. Bell, O. Deubzer, *MRS Bull.* **43**, 581-587 (2018).
 90. A.R. Paterson, H. Nagata, X. Tan, J.E. Daniels, M. Hinterstein, R. Ranjan, P.B. Groszewicz, W. Jo, J.L. Jones, *MRS Bull.* **43**, 600-606 (2018).

91. K. Shibata, R. Wang, T. Tou, J. Koruza, *MRS Bull.* **43**, 612-616 (2018).
92. K. Wang, B. Malič, J. Wu, *MRS Bull.* **43**, 607-611 (2018).
93. T. Zheng, J. Wu, D. Xiao, J. Zhu, *Progr. Mater. Sci.* **98**, 552-624 (2018).
94. C.-H. Hong, H.-P. Kim, B.-Y. Choi, H.-S. Han, J.S. Son, C.W. Ahn, W. Jo, *J. Materiomics* **2**, 1-24 (2016).
95. H.-P. Kim, C.W. Ahn, Y. Hwang, H.-Y. Lee, W. Jo, *J. Kor. Ceram. Soc.* **54**, 86-95 (2017).
96. S. Zhang, R. Xia, T.R. ShROUT, *Appl. Phys. Lett.* **91**, 132913 (2007).
97. B. Wu, H. Wu, J. Wu, D. Xiao, J. Zhu, S.J. Pennycook, *J. Am. Chem. Soc.* **138**, 15459-15464 (2016).
98. Y. Huang, C. Zhao, B. Wu, J. Wu, *J. Am. Ceram. Soc.* **102**, 2648-2657 (2018).
99. M.-H. Zhang, K. Wang, J.-S. Zhou, J.-J. Zhou, X. Chu, X. Lv, J. Wu, J.-F. Li, *Acta Materialia*. **122**, 344-351 (2017).
100. T. Wang, C. Wu, J. Xing, J. Wu, B. Li-Chen, X. Xu, K. Wang, J. Zhu, *J. Am. Ceram. Soc.* **00**, 1-11 (2019).
101. E.D. Politova, N.V. Golubko, G.M. Kaleva, A.V. Mosunov, N.V. Sadovskaya, S. Yu. Stefanovich, D.A. Kiselev, A.M. Kislyuk, M.V. Chichkov, P.K. Panda, *Ferroelectrics*. **538**, 45-51 (2019).
102. Y.-X. Liu, H.-C. Thong, C. Zhao, Q. Liu, X. Xu, K. Wang, J.-F. Li, *J. Mater. Chem. C*, (2019).
103. F.-Z. Yao, K. Wang, W. Jo, K.G. Webber, T.P. Comyn, J.-X. Ding, B. Xu, L.-Q. Cheng, M.-P. Zheng, Y.-D. Hou, J.-F. Li, *Adv. Funct. Mater.* **26**, 1217-1224 (2016).
104. Y. Chang, S. Poterala, Z. Yang, G.L. Messing, *J. Am. Ceram. Soc.* **94**, 2494-2498 (2011).
105. H. Zhang, Y. Zhu, P. Fan, M.A. Marwat, W. Ma, K. Liu, H. Liu, B. Xie, K. Wang, J. Koruza, *Acta Materialia* **156**, 389-398 (2018).
106. L. Jiang, Y. Li, L. Xie, J. Wu, Q. Chen, W. Zhang, D. Xiao, J. Zhu, *J. Mater. Sci. Mater. Electron.* **28**, 8500-8509 (2017).
107. Y.-H. Seo, D.J. Franzbach, J. Koruza, A. Benčan, B. Malič, M. Kosec, J.L. Jones, K.G. Webber, *Phys. Rev. B.* **87**, (2013).
108. J.A.G. B. Noheda, L.E. Cross, R. Guo, S.E. Park, D.E. Cox, G. Shirane, *Phys. Rev. B.* **61**, (2000).
109. J. Frantti, S. Ivanov, S. Eriksson, H. Rundlöf, V. Lantto, J. Lappalainen, M. Kakihana, *Phys. Rev. B.* **66**, (2002).
110. Z. Li, H.C. Thong, Y.F. Zhang, Z. Xu, Z. Zhou, Y.X. Liu, Y.Y.S. Cheng, S.H. Wang, C.

- Zhao, F. Chen, K. Bi, B. Han, K. Wang, *Adv. Funct. Mater.* **31**, (2020).
111. T.R. Shrout, S.J. Zhang, *J. Electroceram.* **19**, 113-126 (2007).
112. J. Zushi, T. Ariizumi, S. Kojima, R. Wang, H. Bando, *Jpn. J. Appl. Phys.* **52**, (2013).
113. R. Wang, K. Wang, F. Yao, J.-F. Li, F.H. Schader, K.G. Webber, W. Jo, J. Rödel, S. Zhang, *J. Am. Ceram. Soc.* **98**, 2177-2182 (2015).
114. J. Acker, H. Kungl, M.J. Hoffmann, *J. Am. Ceram. Soc.* **93**, 1270-1281 (2010).
115. M. Feizpour, T. Ebadzadeh, D. Jenko, *Materiali in tehnologije.* **49**, 975-982 (2015).
116. H.-S. Han, J. Koruza, E.A. Patterson, J. Schultheiß, E. Erdem, W. Jo, J.-S. Lee, J. Rödel, *J. Eur. Ceram. Soc.* **37**, 2083-2089 (2017).
117. T. Huang, D. Xiao, C. Liu, F. Li, B. Wu, J. Wu, J. Zhu, *Ceram. Int.* **40**, 2731-2735 (2014).
118. R. Zuo, J. Fu, *J. Am. Ceram. Soc.* **94**, 1467-1470 (2011).
119. M.I. Morozov, M.-A. Einarsrud, J.R. Tolchard, P.T. Geiger, K.G. Webber, D. Damjanovic, T. Grande, *J. Appl. Phys.* **118**, (2015).
120. A.S. Karapuzha, N.K. James, H. Khanbareh, S. van der Zwaag, W.A. Groen, *Ferroelectrics.* **504**, 160-171 (2016).
121. Y. Zhang, D. Xue, H. Wu, X. Ding, T. Lookman, X. Ren, *Acta Materialia* **71**, 176-184 (2014).
122. M. Hinterstein, M. Hoelzel, J. Rouquette, J. Haines, J. Glaum, H. Kungl, M. Hoffman, *Acta Materialia* **94**, 319-327 (2015).
123. L. Li, M. Zhu, Q. Wei, M. Zheng, Y. Hou, J. Hao, *J. Eur. Ceram. Soc.* **38**, 1381-1388 (2018).
124. T.A. Duong, F. Erkinov, M. Aripova, C.W. Ahn, B.W. Kim, H.S. Han, J.S. Lee, *Ceram. Int.* **47**, 4925-4932 (2020).
125. S. Zhang, R. Xia, T.R. Shrout, *J. Electroceram.* **19**, 251-257 (2007).
126. Z. Liu, H. Fan, C. Long, *J. Mater. Sci.* **49**, 8107-8115 (2014).
127. H.Q. Fan, Z. Li, P.R. Ren, G.C. Jiao, *Mater. Sci. Forum.* **654-656**, 1978-1981 (2010).
128. Z. Liu, H. Fan, Y. Zhao, G. Dong, W. Jo, *J. Am. Ceram. Soc.* **99**, 146-151 (2016).
129. K. Ramam, M. Lopez, *J. Eur. Ceram. Soc.* **27**, 3141-3147 (2007).
130. C. Liu, D. Xiao, T. Huang, J. Wu, F. Li, B. Wu, J. Zhu, *Mater. Lett.* **120**, 275-278 (2014).
131. J. Du, Z. Xu, R. Chu, J. Hao, W. Li, P. Zheng, *J. Mater. Sci. Mater. Electron.* **27**, 6535-6541 (2016).
132. D. Lin, K.W. Kwok, *J. Mater. Sci. Mater. Electron.* **23**, 501-505 (2011).

133. J. Hao, Z. Xu, R. Chu, W. Li, J. Du, *J. Mater. Res.* **30**, 2018-2029 (2015).
134. Y. Guo, K.-i. Kakimoto, H. Ohsato, *Appl. Phys. Lett.* **85**, 4121-4123 (2004).
135. K. Wang, F.-Z. Yao, W. Jo, D. Gobeljic, V.V. Shvartsman, D.C. Lupascu, J.-F. Li, J. Rödel, *Adv. Funct. Mater.* **23**, 4079-4086 (2013).
136. S.N. K. Uchino, L. E. Cross, R. E. Newnham, S. J. Jang, *J. Mater. Sci.* **16**, 569-678 (1981).
137. Y. Zhang, L. Li, B. Shen, J. Zhai, *Dalton Trans.* **44**, 7797-802 (2015).
138. Y. Huan, X. Wang, J. Koruza, K. Wang, K.G. Webber, Y. Hao, L. Li, *Sci. Rep.* **6**, 22053 (2016).
139. J. Fu, R. Zuo, Y. Xu, J.F. Li, M. Shi, *J. Eur. Ceram. Soc.* **37**, 975-983 (2017).
140. M.D. Maeder, D. Damjanovic, N. Setter, *J. Electroceramic.* **13**, 385-392 (2004).
141. Y. Li, K. Moon, C.P. Wong, *Science.* **308**, 1419-1420 (2005).
142. G.F. Fan, M.B. Shi, W.Z. Lu, Y.Q. Wang, F. Liang, *J. Eur. Ceram. Soc.* **34**, 23-28 (2014).
143. S. Guan, H. Yang, Y. Zhao, R. Zhang, *J. Alloys Compd.* **735**, 386-393 (2018).
144. T.H. Chung, K.W. Kwok, *J. Alloys Compd.* **737**, 317-322 (2018).
145. I. Izzuddin, M.H. Hj. Jumal, Z. Zainuddin, N.H. Janil, *Ceram. Int.* **45**, 17204-17209 (2019).
146. E.D. Politova, G.M. Kaleva, A.V. Mosunov, N.V. Sadovskaya, D.A. Kiselev, A.M. Kislyuk, T.S. Ilina, S. Yu. Stefanovich, E.A. Fortalnova, *Ferroelectrics.* **560**, 38-47 (2020).
147. J. Hao, Z. Xu, R. Chu, W. Li, J. Du, *J. Mater. Sci. Mater. Electron.* **26**, 7867-7872 (2015).
148. J.E. Garcia, F. Rubio-Marcos, *J. Appl. Phys.* **127**, (2020).
149. X. Vendrell, J.E. García, X. Bril, D.A. Ochoa, L. Mestres, G. Dezanneau, *J. Eur. Ceram. Soc.* **35**, 125-130 (2015).
150. W. Liang, W. Wu, D. Xiao, J. Zhu, J. Wu, *J. Mater. Sci.* **46**, 6871-6876 (2011).
151. B. Zhang, J. Wu, X. Wang, X. Cheng, J. Zhu, D. Xiao, *Curr. Appl. Phys.* **13**, 1647-1650 (2013).
152. J. Fu, R. Zuo, S.C. Wu, J.Z. Jiang, L. Li, T.Y. Yang, X. Wang, L. Li, *Appl. Phys. Lett.* **100**, (2012).
153. B. Orayech, A. Faik, G.A. López, O. Fabelo, J.M. Igartua, *J. Appl. Crystallography.* **48**, 318-333 (2015).
154. H.-S.H. Tran Vu Diem Ngoca, Kyung-Jong Kima, Rizwan Ahmed Malika, Ali Hussainb and Jae-Shin Lee, *J. Ceram. Proces. Res.* **13**, 177-180 (2012).

155. V.V. Lemanov, N.V. Zaitseva, E.P. Smirnova, P.P. Syrnikov, *Ferroelectr. Lett. Section.* **19**, 7-12 (1995).
156. J. Ravez, A. Simon, *Mater. Lett.* **36**, 81–84 (1998).
157. H. Yu, Z.-G. Ye, *J. Appl. Phys.* **103**, (2008).
158. A.A. Bokov, Z.G. Ye, *J. Mater. Sci* **41**, 31-52 (2006).
159. A.A. Bokov, B.J. Rodriguez, X. Zhao, J.-H. Ko, S. Jesse, X. Long, W. Qu, T.H. Kim, J.D. Budai, A.N. Morozovska, S. Kojima, *Zeitschrift für Kristallographie.* **226**, 99-107 (2011).
160. N. Setter, *Ferroelectrics.* **500**, 164-182 (2016).
161. R.C. C. E. Ciomaga, M. T. Buscaglia, M. Viviani, V. Buscaglia, L. Mitoseriu, A. Stancu, P. Nanni, *J. Optoelectron. Adv. Mater.* **8**, (2006).
162. S. Favre, A. Moreno, D. Garcia, *Mater. Res. Bull.* **47**, 486-490 (2012).
163. T. Maiti, R. Guo, A.S. Bhalla, *Ferroelectrics.* **425**, 4-26 (2011).
164. T. Badapanda, S.K. Rout, L.S. Cavalcante, J.C. Sczancoski, S. Panigrahi, E. Longo, M.S. Li, *J. Phys. D: Appl. Phys.* **42**, (2009).
165. J. Ravez, A. Simon, *J. Solid State Chem.* **162**, 260-265 (2001).
166. C. Lei, A.A. Bokov, Z.G. Ye, *J. Appl. Phys.* **101**, (2007).
167. K. Uchino, S. Nomura, *Ferroelectrics.* **44**, 55-61 (2011).
168. F. Li, S. Zhang, Z. Xu, L.-Q. Chen, *Adv. Funct. Mater.* **27**, (2017).
169. M. Zhou, R. Liang, Z. Zhou, X. Dong, *Ceram. Int.* **45**, 3582-3590 (2019).
170. H. Tao, H. Wu, Y. Liu, Y. Zhang, J. Wu, F. Li, X. Lyu, C. Zhao, D. Xiao, J. Zhu, S.J. Pennycook, *J. Am. Chem. Soc.* **141**, 13987-13994 (2019).
171. D. Berlincourt, H.H.A. Krueger, *J. Appl. Phys.* **30**, 1804-1810 (1959).
172. M. Acosta, N. Novak, V. Rojas, S. Patel, R. Vaish, J. Koruza, G.A. Rossetti, J. Rödel, *Appl. Phys. Rev.* **4**, (2017).
173. Q.M. Zhang, W.Y. Pan, S.J. Jang, L.E. Cross, *J. Appl. Phys.* **64**, 6445-6451 (1988).
174. L. Jin, R. Huo, R. Guo, F. Li, D. Wang, Y. Tian, Q. Hu, X. Wei, Z. He, Y. Yan, G. Liu, *ACS Appl. Mater. Interfaces.* **8**, 31109-31119 (2016).
175. X.-x. Sun, J. Zhang, X. Lv, X.-x. Zhang, Y. Liu, F. Li, J. Wu, *J. Mater. Chem. A.* **7**, 16803-16811 (2019).
176. D. Xue, Y. Zhou, H. Bao, C. Zhou, J. Gao, X. Ren, *J. Appl. Phys.* **109**, (2011).
177. G. Shirane, R. Newnham, R. Pepinsky, *Phys. Rev.* **96**, 581-588 (1954).
178. Y. Dai, X. Zhang, G. Zhou, *Appl. Phys. Lett.* **90**, 262903 (2007).

179. K.T. Lee, D.H. Kim, S.H. Cho, J.S. Kim, J. Ryu, C.W. Ahn, T.H. Lee, G.H. Kim, S. Nahm, *J. Alloys Compd.* **784**, 1334-1343 (2019).
180. D.S. Horn, G.L. Messing, *Mater. Sci. Eng. A.* **195**, 169-178 (1995).
181. C.A. Bateman, S.J. Bennison, M.P. Harmer, *J. Am. Ceram. Soc.* **72**, 1241-1244 (1989).
182. B.-K. Lee, S.-Y. Chung, S.-J. Kang, *Acta mater.* **48**, 1575-1580 (2000).
183. Y. Yu, X.-S. Wang, H. Zou, Y.-X. Li, X. Yao, *Mater. Res. Bull.* **69**, 56-60 (2015).
184. M.S. Yoon, H.M. Jang, *J. Appl. Phys.* **77**, 3991-4001 (1995).
185. R. Zuo, F. Li, J. Fu, D. Zheng, W. Zhao, H. Qi, *J. Eur. Ceram. Soc.* **36**, 515-525 (2016).
186. Y.M. Jin, Y.U. Wang, A.G. Khachatryan, J.F. Li, D. Viehland, *J. Appl. Phys.* **94**, 3629-3640 (2003).

Publications

Patents

- 1) Production method of lead-free piezoelectric ceramics with high strains, Kor. Patent Application No. 10-2016-0082892 (2016).
- 2) Lead-free piezoelectric ceramic ternary compositions with high strains, Kor. Patent Application No. 10-2017-0064310 (2017).
- 3) Lead-free piezoelectric ceramic composition and preparation method thereof, Kor. Patent Application No. 10-2020-0076707 (2020).

Journal papers

- 1) Thi Hinh Dinh, Jin-Kyu Kang, Hoang Thien Khoi Nguyen, **Trang An Duong**, Vu Diem Ngoc Tran, Ky Nam Pham, and Jae-Shin Lee, *Giant strain in lead-free relaxor/ferroelectric piezocomposite ceramics*, J. Korean Phys. Soc. **68**, 1439–1444 (2016).
- 2) Chang-Heon Lee, Hyung-Su Han, **Trang An Duong**, Thi Hinh Dinh, Chang Won Ahn, and Jae-Shin Lee, *Stabilization of the relaxor phase by adding CuO in lead-free $(Bi_{1/2}Na_{1/2})TiO_3$ - $SrTiO_3$ - $BiFeO_3$ ceramics*, Ceram. Int. **43**, 11071–11077 (2017).
- 3) **Trang An Duong**, Hyung-Su Han, Young-Hwan Hong, Hoang Thien Khoi Nguyen, Thi Hinh Dinh, and Jae-Shin Lee, *Dielectric and piezoelectric properties of $Bi_{1/2}Na_{1/2}TiO_3$ - $SrTiO_3$ lead-free ceramics*, J. Electroceram. **41**, 73–79 (2018).
- 4) **Trang An Duong**, Farruhk Erkinov, Hoang Thien Khoi Nguyen, Chang-Won Ahn, Byeong Woo Kim, Hyung-Su Han, and Jae-Shin Lee, *Temperature insensitive piezoelectric properties on the morphotropic phase boundary of $BaZrO_3$ -modified lead-free KNN-BLT ceramics*, J. Electroceram. Accepted (04/2021).
- 5) **Trang An Duong**, Farruhk Erkinov, Mastura Aripova, Chang Won Ahn, Byeong Woo

Kim, Hyoung–Su Han, Jae–Shin Lee, *Ferroelectric–to–relaxor crossover in KNN–based lead–free piezoceramics*, *Ceram. Int.* **47**, 4925–4932 (2021).

6) Sang–Hun Lee, Seong–Hyun Kim, Farrukh Erkinov, Hoang Thien Khoi Nguyen, **Trang An Duong**, Hyoung–Su Han, Jae–Shin Lee, *Dielectric and piezoelectric properties of microwave sintered BNT–ST ceramics*, *J. KIEEME* **33**, 37–44 (2020).

6) Hyoung–Su Han, **Trang An Duong**, Chang Won Ahn, Wook Jo, Jae–Shin Lee, *A brief review of enhancing incipient piezostains: Approach by ceramic/ceramic composites*, *Ceramist* **23**, 89–100 (2020).

8) Hoang Thien Khoi Nguyen, **Trang An Duong**, Farrukh Erkinov, Hyungwon Kang, Byeong Woo Kim, Chang Won Ahn, Hyoung–Su Han, Jae–Shin Lee, *Effect of SrTiO₃ modification on dielectric, phase transition and piezoelectric properties of lead–free Bi_{0.5}Na_{0.5}TiO₃–CaTiO₃–SrTiO₃ piezoelectric ceramics*, *J. Kor. Ceram. Soc.* **57**, 570–577 (2020).

9) Hoang Thien Khoi Nguyen, **Trang An Duong**, Farrukh Erkinov, Chang Won Ahn, Byeong Woo Kim, Hyoung–Su Han, Jae–Shin Lee, *Large Electric Field–Induced Strain Response Under a Low Electric Field in Lead–Free Bi_{1/2}Na_{1/2}TiO₃–SrTiO₃–BiAlO₃ Ternary Piezoelectric Ceramics*, *J. Electro. Mater.* **49**, 6677–6685 (2020).

10) Hoang Thien Khoi Nguyen, **Trang An Duong**, Sang Sub Lee, Chang Won Ahn, Hyoung–Su Han, Jae–Shin Lee, *Comparing the electromechanical properties of CaTiO₃–and BaZrO₃–modified BiO_{0.5}Na_{0.5}TiO₃–SrTiO₃ ceramics*, *J. Mater. Res.* **94**, 1–10 (2020).

11) **Trang An Duong**, ..., Hyoung–Su Han, and Jae–Shin Lee, *Effects of SrTiO₃ modification on tetragonal phase stabilization of lead–free KNN–based piezoceramics*, will be submitted.

12) **Trang An Duong**, ..., Hyoung-Su Han, and Jae-Shin Lee, *Bi_{0.5}Na_{0.5}TiO₃-SrTiO₃ lead-free ceramics composites near nonergodic-ergodic relaxor phase transition*, will be submitted.

13) **Trang An Duong**, ..., Hyoung-Su Han, and Jae-Shin Lee, *New phase boundary originating from coexistence of ferroelectrics and relaxor in lead-free piezoelectric KNN-based composites*, will be submitted.

Oral presentations

1) 웬호앙티엔코이, 딘치힌, **즈엉짱안**, 정광휘, 홍영환, 김일원, 이재신, *Large low field strain properties of Bi_{0.5}Na_{0.5}TiO₃-SrTiO₃ ceramics with heterogeneity compositions*, The 10th Asian Meeting on Electroceramics (AMEC-10), 2016.12.04~12.07, GISTAIPEI TECH Convention Center, Taiwan.

2) 딘치힌, 찬부이엠옥, 강진규, 웬호앙티엔코이, **즈엉짱안**, 김일원, 이창현, 이재신, *Enhanced low-field strain in Bi-based ferroelectric/relaxor ceramic composites*, IWPMA & ECMD, 2016.08.21~08.24, 서귀포 KAL 호텔, 서귀포

3) **즈엉짱안**, 웬호앙티엔코이, 김성덕, 딘치힌, 김일원, 이재신, *Dielectric and piezoelectric properties of Bi_{0.5}Na_{0.5}TiO₃-SrTiO₃ lead-free ceramics*, 한국전기전자재료학회, 2016.11.17~11.18, 목포대학교, 무안군.

4) 이재신, 웬호앙티엔코이, **즈엉짱안**, 딘치힌, 한형수, *Understanding of giant strain in lead-free Bi-based piezoelectric ceramics*, ICMFM, 20170508~ 20170510, Hanoi Army Hotel, 베트남

5) 웬호앙티엔코이, 딘치힌, **즈엉짱안**, 정광휘, 홍영환, 김일원, 이재신, *Effect of micro scale heterogeneity on electromechanical strain properties of lead-free (Bi_{1/2}Na_{1/2})TiO₃-SrTiO₃ ceramic composites*, ICMFM, 20170508~ 20170510, Hanoi Army Hotel, 베트남.

- 6) 이상훈, 김성현, 즈영짱안, 한형수, 이재신, *Dielectric and piezoelectric properties of $Bi_{1/2}Na_{1/2}TiO_3$ - $SrTiO_3$ lead-free ceramics*, IFAAP, 2018.05.27~06.01, Hiroshima International Conference Center, 일본.
- 7) 한형수, 즈영짱안, 딘치힌, 안창원, 이재신, *Stabilization of the relaxor phase by adding CuO in lead-free $(Bi_{1/2}Na_{1/2})TiO_3$ - $SrTiO_3$ - $BiFeO_3$ ceramics*, IFAAP, 2018.05.27~06.01, Hiroshima International Conference Center, 일본.
- 8) 이상훈, 이재신, 한형수, 즈영짱안, 웬호양티엔코이, 에르키노프파루크, *$SrTiO_3$ 변성에 의한 BNT 계 무연 압전 세라믹스의 미세구조, 결정구조, 전기적 특성변화에 관한 연구*, 한국전기전자재료학회, 2018.06.20~06.22, 대명 델피노리조트, 강원도 고성군.
- 9) 웬호양티엔코이, 이재신, 한형수, 김성현, 즈영짱안, 에르키노프파루크, *$(Bi,Na)TiO_3$ - $(Bi,K)TiO_3$ 계 강유전체/완화형 강유전체 복합세라믹스의 저전계 변형특성에 관한 연구*, 한국전기전자재료학회, 2018.06.20~06.22, 대명 델피노리조트, 강원도 고성군.
- 10) 에르키노프파루크, 한형수, 즈영짱안, 웬호양티엔코이, 마스투라아리포봐, 이재신, *Dielectric and piezoelectric properties of BNT-ST composite ceramics*, 한국전기전자재료학회, 2018.11.20~11.22, 부여롯데리조트, 충남 부여.
- 11) 즈영짱안, 웬호양티엔코이, 이상훈, 에르키노프파루크, 이재신, 한형수, *Effects of Li_2CO_3 modification on piezoelectric properties and phase transition behavior of lead-free $Na_{0.5}K_{0.5}NbO_3$ - $SrTiO_3$ piezoceramics*, 한국전기전자재료학회, 2019.06.16~06.21, 웰리힐리파크, 횡성.
- 12) 즈영짱안, 에르키노프파루크, 웬호양티엔코이, 안창원, 이재신, 한형수, *Formation of the rhombohedral-tetragonal morphotropic phase boundary in KNN-based lead-free piezoelectric ceramics*, ICAE, 2019.11.05~11.08, Ramada Plaza Jeju Hotel,

제주.

13) 웬호앙티엔코이, 즈엉짱안, 에르키노프파루크, 이상훈, 한형수, 이재신, *Effects of CaTiO₃-modification on the dielectric and piezoelectric properties of the lead-free (Bi_{1/2}Na_{1/2})TiO₃-SrTiO₃ piezoelectric ceramics*, ICAE, 2019.11.05~11.08, Ramada Plaza Jeju Hotel, 제주.

14) Trang An Duong, Hoang Thien Khoi Nguyen, Sang-Sup Lee, Chang-Won Ahn, Hyoung-Su Han, Jae-Shin Lee, *Effects of BaZrO₃ Modification on Electrical Properties and Relaxor Behavior of Lead-free K_{0.5}Na_{0.5}O₃ Piezoceramics*, ICC8, 2021.04.25~04.30, Virtual, Korea.

Poster presentations

1) 웬호앙티엔코이, 딘치힌, 즈엉짱안, 정광휘, 홍영환, 김일원, 이재신, *정규-완화형 강유전체 상전이 영역에서 Bi_{0.5}Na_{0.5}TiO₃-SrTiO₃ 무연압전 세라믹스의 변형 특성*, 한국세라믹학회, 2016.04.20~ 04.22, BEXCO 제 2 전시장, 부산.

2) 즈엉짱안, 웬호앙티엔코이, 딘치힌, 김일원, 이재신, *Bi_{0.5}Na_{0.5}TiO₃-SrTiO₃ 세라믹스의 소결 거동 및 압전 특성에 대한 CuO 도핑의 영향*, 한국세라믹학회, 2016.04.20~ 04.22, BEXCO 제 2 전시장, 부산.

3) 강진규, 딘치힌, 박영석, 웬호앙티엔코이, 이창현, 즈엉짱안, 이재신, *Bi_{0.5}Na_{0.5}TiO₃-SrTiO₃-BiFeO₃ 삼성분계 강유전성 세라믹스의 저온소성*, 한국재료학회, 2016.05.18 ~ 05.20, 디오션리조트, 여수.

4) 박영석, 이창현, 강진규, 딘치힌, 즈엉짱안, 웬호앙티엔코이, 이재신, *Bi_{0.5}Na_{0.5}TiO₃-SrTiO₃-BiFeO₃ 삼성분계 강유전성 세라믹스의 저온소성 연구*, 한국전기전자재료학회, 2016.06.22~06.24, 현대호텔경주, 경주.

- 5) 이창현, 홍영환, 이동훈, 즈엉짱안, 웨호앙티엔코이, 딘치힌, 이재신 *Electric-field-induced strain properties of $Bi_{1/2}Na_{1/2}TiO_3$ - $SrTiO_3$ - $LiNbO_3$ ternary ceramics*, 한국전기전자재료학회, 2016.06.22~06.24, 현대호텔경주, 경주.
- 6) 박영석, 이창현, 강진규, 웨호앙티엔코이, 즈엉짱안, 딘치힌, 이재신, *Low Temperature sintering of ternary $Bi_{0.5}Na_{0.5}TiO_3$ - $SrTiO_3$ - $BiFeO_3$ piezoelectric ceramics*, 한국전기전자재료학회, 2016.06.22~06.24, 현대호텔경주, 경주.
- 7) 왕국, 딘치힌, 웨호앙티엔코이, 이창현, 즈엉짱안, 한형수, 이재신, *Electric field-induced giant strain in $Bi_{0.47-x}La_xNa_{0.47}Ba_{0.06}TiO_3$ ceramics*, 한국세라믹학회, 2016.11.23~11.25, 코엑스, 서울.
- 8) 이창현, 박영석, 즈엉짱안, 딘치힌, 한형수, 김일원, 이재신, *Low temperature sintering of CuO-added ($Bi_{1/2}Na_{1/2}$) TiO_3 - $SrTiO_3$ - $BiFeO_3$ ternary piezoelectric ceramics*, The 10th Asian Meeting on Electroceramics (AMEC-10), 2016.12.04 ~12.07, GISTAIPEI TECH Convention Center, Taiwan.
- 9) 김성현, 이창현, 홍영환, 즈엉짱안, 왕국, 한형수, 이재신, *BNT-ST- ABO_3 삼성분계 무연 압전 세라믹스의 유전 특성 및 전계 유기 변형 특성 연구*, 한국전기전자재료학회, 2017.06.21~06.23, 알펜시아리조트컨벤션센터, 평창.
- 10) 즈엉짱안, 이창현, 정광휘, 웨호앙티엔코이, 이재신, 한형수, *무연 KNN 계 세라믹의 결정구조, 유전체, 강유전성, 압전 특성에 미치는 $BaZrO_3$ 변성의 영향*, 한국전기전자재료학회, 2017.06.21~06.23, 알펜시아리조트컨벤션센터, 평창.
- 11) 즈엉짱안, 김성현, 이상훈, 웨호앙티엔코이, 이재신, 한형수, *KNN 계 무연 압전 세라믹스의 결정구조와 전기적특성 변화에 관한 연구*, 한국전기전자재료학회, 2018.06.20~06.22, 대명 텔피노리조트, 강원도 고성군.

12) 김민영, 임태현, 즈엉짱안, 웬호앙티엔코이, 김성현, 한형수, 이재신, *BNT-ST 세라믹스의 압전성에 대한 Bi 이온의과잉과 결핍 효과 비교 연구*, 한국전기전자재료학회, 2018.11.20~11.22, 부여롯데리조트, 충남 부여.

13) 임태현, 정경훈, 즈엉짱안, 웬호앙티엔코이, 이상훈, 한형수, 이재신, *BNT-ST 세라믹스의 압전성에 대한 주개와 받개 불순물 도핑 효과 비교 연구*, 한국전기전자재료학회, 2018.11.20~11.22, 부여롯데리조트, 충남 부여.

13) 한형수, 이창현, 에르키노프파루크, 이상훈, 즈엉짱안, 웬호앙티엔코이, 이재신, *CuO 첨가에 의한 무연 압전 BNT-ST-BF 세라믹스의 소결 온도와 전계유기변형특성 변화에 관한 연구*, 한국재료학회, 2019.05.15~05.17, 알펜시아리조트 컨벤션센터, 평창

14) 웬호앙티엔코이, 즈엉짱안, 이상훈, 한형수, 이재신, *Investigation of phase transition behavior and electrical properties in the ternary $(Bi_{1/2}Na_{1/2})TiO_3-SrTiO_3-CaTiO_3$ lead-free piezoelectric ceramics*, 한국전기전자재료학회, 2019.06.16~06.21, 웰리힐리파크, 횡성.

15) 한형수, 홍영환, 즈엉짱안, 웬호앙티엔코이, 안창원, 이재신, *Effects of sintering temperature on microstructures, phase transition behaviors, and electrical properties in $LiNbO_3$ -modified $Bi_{1/2}Na_{1/2}TiO_3-SrTiO_3$ relaxor ceramics*, 한국전기전자재료학회, 2019.06.16~06.21, 웰리힐리파크, 횡성.

16) 즈엉짱안, 에르키노프파루크, 이상훈, 이재신, 한형수, *Effects of $BaZrO_3$ modification on piezoelectric properties and phase transition behavior of lead-free $K_{0.5}Na_{0.5}NbO_3$ piezoceramics*, ICAE, 2019.11.05~11.08, Ramada Plaza Jeju Hotel, 제주.

17) Nguyen Hoang Thien Khoi, Duong Trang An, Kim Byeong-Woo, Ahn Chang-Won, Han Hyung-Su, Lee Jae-Shin, *Effect of $SrTiO_3$ Modification on Dielectric, Phase Transition and Piezoelectric Properties of Lead-Free $Bi_{1/2}Na_{1/2}TiO_3-CaTiO_3-SrTiO_3$*

Piezoelectric Ceramics, 한국세라믹학회 춘계학술대회, 2020.07.06~09, Virtual, Korea.

18) Trang An Duong, Hoang Thien Khoi Nguyen, Sang-Sub Lee, Farrukh Erkinov, Chang-Won Ahn, Hyoun-Su Han, Jae-Shin Lee, *Enhancement of Piezoelectric Properties and Temperature Stability in BaZrO₃-Modified Lead-Free KNN-BLT Ceramics with Morphotropic Phase Boundary*, 한국전기전자재료학회 - 하계학술대회, 2020.07.08~10, 휘닉스 평창 호텔, 평창.

19) Hyoun-Su Han, Hoang Thien Khoi Nguyen, Trang An Duong, Chang-Won Ahn, Jae-Shin Lee, *Large Field-induced Strain Properties of BiAlO₃-Modified Bi_{1/2}Na_{1/2}TiO₃-SrTiO₃ Lead-Free Piezoelectric Ceramics*, 한국전기전자재료학회 - 하계학술대회, 2020.07.08~10, 휘닉스 평창 호텔, 평창.

20) Hyoun-Su Han, Hoang Thien Khoi Nguyen, Trang An Duong, Chang Won Ahn, Jae-Shin Lee, *Nonergodicity-Derived Thermal Stability of Electromechanical Strain Properties in CaTiO₃-Modified Lead-Free BNT-ST Relaxor Materials*, 한국전기전자재료학회 - 하계학술대회, 2020.07.08~10, 휘닉스 평창 호텔, 평창.

21) 남채영, 김수진, 이상섭, 웬 호앙 티엔 코이, 즈영 짱 안, 한형수, 이재신, *(Bi_{1/2}Na_{1/2})TiO₃계 무연 압전 세라믹스의 유전 및 압전특성에 관한 SrTiO₃ 첨가 효과*, 한국전기전자재료학회 - 하계학술대회, 2020.07.08~10, 휘닉스 평창 호텔, 평창.

22) 김수진, 남채영, 이상섭, 즈영 짱 안, 웬 호앙 티엔 코이, 한형수, 이재신, *BNT 무연압전 세라믹스의 압전 특성과 전기유기 변형특성에 관한 주개/받개 원소 도핑효과*, 한국전기전자재료학회 - 하계학술대회, 2020.07.08~10, 휘닉스 평창 호텔, 평창.

23) Trang An Duong, Hoang Thien Khoi Nguyen, Sang-Sub Lee, Chang-Won Ahn, Hyoung-Su Han, Jae-Shin Lee, *Effects of BaZrO₃ Modification on Crystal Structure and Ferroelectricity Disruption in Lead free KNN Piezoceramics*, 한국전기전자재료학회 – 추계학술대회, 2020.11.05~06, The-K 호텔, 경주.

23) Hoang Thien Khoi Nguyen, Trang An Duong, Sang-Sub Lee, Chang-Won Ahn, Hyoung-Su Han, Jae-Shin Lee, *The Difference of Ferroelectric-Relaxor Phase Transition Behavior between CaTiO₃ and BaZrO₃ Modification in Bi_{0.5}Na_{0.5}TiO₃-SrTiO₃ Lead-Free Piezoceramics*, 한국전기전자재료학회 – 추계학술대회, 2020.11.05~06, The-K 호텔, 경주.

25) Sang-Sub Lee, Hoang Thien Khoi Nguyen, Trang An Duong, Chang-Won Ahn, Hyoung-Su Han, Jae-Shin Lee, *Thermal stability of electromechanical strain properties for CaTiO₃-modified (Bi_{1/2}Na_{1/2})TiO₃ -SrTiO₃ lead-free piezoceramics*, 한국전기전자재료학회 – 추계학술대회, 2020.11.05~06, The-K 호텔, 경주.

26) 남채영, 김수진, 김운기, 김승홍, 채주현, 대표님, 즈영 짱 안, 한형수, 이재진, *코어-셸 구조의 구리-은 나노 분말을 이용한 전도성 전극 개발*, 한국전기전자재료학회 – 추계학술대회, 2020.11.05~06, The-K 호텔, 경주.

27) 김수진, 김운기, 남채영, 즈영 짱 안, 웬 호앙 티엔 코이, 안창원, 한형수, 이재진, *(Bi_{1/2}Na_{1/2})TiO₃-SrTiO₃ 무연 압전 세라믹스의 거대변형 특성에 대한 BiAlO₃ 변성 효과*, 한국전기전자재료학회 – 추계학술대회, 2020.11.05~06, The-K 호텔, 경주.

28) Sang-Sub Lee, Hoang Thien Khoi Nguyen, Trang An Duong, Hyoung-Su Han, Jae-Shin Lee, *Effect of SrTiO₃ on dielectric and piezoelectric properties in lead-free Bi_{1/2}Na_{1/2}TiO₃-2BiFeO₃ based piezoceramics*, 한국센서학회 – 추계학술대회, 2020.11.11~13, 라카이샌드파인리조트, 강릉.

29) Woon-Gi Kim, Su-Jin Kim, Hoang Thien Khoi Nguyen, Trang An Duong, Chang Won Ahn, Hyoung-Su Han, Jae-Shin Lee, *Stress-derived large strain properties under low electric field of $(Bi_{1/2}Na_{1/2})TiO_3$ - $SrTiO_3$ - $BiAlO_3$ lead-free piezoelectric ceramics*, 한국센서학회 - 추계학술대회, 2020.11.11~13, 라카이샌드파인리조트, 강능.

30) Chae-Yeong Nam, Su-Jin Kim, Sang-Sub Lee, Hoang Thien Khoi Nguyen, Trang An Duong, Jae-Shin Lee, Hyoung-Su Han, *Dielectric and piezoelectric properties of $SrTiO_3$ -modified $Bi_{1/2}Na_{1/2}TiO_3$ lead-free ceramics*, 한국센서학회 - 추계학술대회, 2020.11.11~13, 라카이샌드파인리조트, 강능.

31) Hoang Thien Khoi Nguyen, Trang An Duong, Sang-Sub Lee, Chang-Won Ahn, Hyoung-Su Han, Jae-Shin Lee, *Effect of $CaTiO_3$ and $BaZrO_3$ modification on phase transition and piezoelectric properties of lead-free $Bi_{0.5}Na_{0.5}TiO_3$ - $SrTiO_3$ piezoelectric ceramics*, 한국센서학회 - 추계학술대회, 2020.11.11~13, 라카이샌드파인리조트, 강능.

32) Trang An Duong, Hoang Thien Khoi Nguyen, Sang-Sub Lee, Chang-Won Ahn, Jae-Shin Lee, Hyoung-Su Han, *Ferroelectric, piezoelectric properties and relaxor behavior of lead-free $(1-x)K_{0.5}Na_{0.5}O_3$ - $xBaZrO_3$ piezoceramics*, 한국센서학회 - 추계학술대회, 2020.11.11~13, 라카이샌드파인리조트, 강능.

33) Hoang Thien Khoi Nguyen, Chang-Heon Lee, Trang An Duong, 이상섭, Hyoung-Su Han, Jae-Shin Lee, *Large electric field-induced strain response under low electric field of lead-free BNT - ST - BA ternary piezoelectric ceramics*, 한국재료학회 - 춘.추계통합학술대회, 2020.11.18~20.

34) Trang An Duong, Farruhk Erkinov, Hoang Thien Khoi Nguyen, Chang-Won Ahn, Hyoung-Su Han, Jae-Shin Lee, *Temperature stability of piezoelectric properties on the morphotropic phase boundary of $BaZrO_3$ -modified lead-free KNN - BLT ceramics*,

한국재료학회 - 춘.추계통합학술대회, 2020.11.18~20, 휘닉스 섭지코지, 제주..

35) 이상섭, Nguyen Hoang Thien Khoi, Duong Trang An, 한형수, 이재신, $SrTiO_3$ 첨가에 따른 $(Bi_{1/2}Na_{1/2})TiO_3-2BiFeO_3$ 무연 압전 세라믹스의 강유전-완화형 강유전체 상전이 거동, 한국세라믹학회 - 추계학술대회, 2020.11.23~25, 컨벤션센터, 대전.

36) Nguyen Hoang Thien Khoi, Duong Trang An, Ahn Chang-Won, Kim Byeong-Woo, Han Hyoung-Su, Lee Jae-Shin, $(Bi_{1/2}Na_{1/2})TiO_3-SrTiO_3$ 계 무연 압전 세라믹스의 자전계 거대 변형 특성에 대한 새로운 개념, 한국세라믹학회 - 추계학술대회, 2020.11.23~25, 컨벤션센터, 대전.

...

Curriculum Vitae

Name: Duong Trang An
Date of birth: 29th of March, 1987
Nationality: Vietnam



Education:

- 09/2015–Present: Study M.S–Ph.D combined course, Materials Science and Engineering, University of Ulsan, Korea
- 2010: B.Sc. in Physics, Hue University’s College of Education, Vietnam

Experience:

- 10/2010–Present: Lecturer in Physics, Hue University’s College of Education, Vietnam

Awards:

- 2020: Best poster award in 2020 KIEEME Annual Autumn Conference, 2020.11.05~06, The K Hotel, , Gyeongju, Republic of Korea
- 2020: Excellent paper award in 2020 The Korean Sensor Society, conference, 2020.11.11~13, Lakai Sanpine Resort, Gangneung, Republic of Korea